Regularized Unfolding of gamma-ray Spectra for Nuclear Physics Applications

E. Lima,[1, 2] L. L. Braseth,[1] A. H. Mjøs,[1, 2] M. Hjorth-Jensen,[1, 3] A. Kvellestad,[1] and A. C. Larsen[1, 2]

[1]*Department of Physics, University of Oslo, N-0316 Oslo, Norway*
[2]*Norwegian Nuclear Research Center, Norway*[*]
[3]*Center for Computing in Science Education, University of Oslo, N-0316 Oslo, Norway*

(Dated: November 24, 2025)

Reconstructing gamma-ray spectra from detector measurements is an ill-posed inverse problem. Standard methods, such as Folding Iteration with Compton Subtraction (FICS), provide point estimates but lack calibrated uncertainties and may bias the spectrum. We introduce an unfolding framework based on regularized maximum-likelihood estimation (RMLE) that enforces non-negativity and detector-response constraints while explicitly modeling background and contaminant contributions. Simulations and analytical results show that RMLE yields smoother reconstructions with well-calibrated confidence intervals and outperforms existing techniques for low-complexity spectra. Although high-complexity data remain challenging, the intervals produced by RMLE maintain correct coverage.

I. INTRODUCTION

The accurate reconstruction of gamma-ray spectra from detector measurements is a fundamental challenge in nuclear physics experiments. The intrinsic physical processes of gamma-ray detection — notably Compton scattering, pair production, and backscattering — transform the true spectrum. Recovering the original spectrum from these transformed measurements constitutes an ill-posed inverse Poisson problem that demands statistical treatment.

Inverse Poisson problems of similar complexity are encountered in various scientific fields, such as medical imaging, astronomy, and particle physics, where advanced methods have been developed. Techniques such as expectation-maximization in PET imaging, Richardson-Lucy deconvolution in astronomy, and singular value decomposition in particle physics have proven effective in their respective domains. However, these approaches fall short when applied to nuclear physics because of three key challenges. First, unlike the predominantly geometric or smooth response functions in other fields, nuclear detector responses are highly complex, combining multiple physical interaction mechanisms that create correlations across the spectrum. Second, the measured spectra in nuclear experiments are highly diverse, ranging from sharp discrete peaks to broad continuous distributions, often in the same spectrum. Finally, the optimization processes often involve millions of parameters, rendering many standard algorithms computationally infeasible.

The gamma-ray spectra of primary interest in this work are those used as input data for the *Oslo Method* [1–3]. The goal of the Oslo Method is to experimentally extract nuclear level densities (NLD) ρ and gamma-ray transmission coefficients $\mathcal{T}$ [4]. This is achieved by simultaneously measuring the gamma-ray energies E_γ and the initial excitation energy $E_{\rm in}$ of gamma cascades of the nucleus under investigation. The first step in the data analysis involves correcting for the detector response, i.e., *unfolding* the spectrum.

To date, this unfolding has been performed using an iterative technique called *Folding Iteration with Compton Subtraction* (FICS) [1]. This approach is a variant of Richardson's method[5] and incorporates two regularization strategies: early stopping and the Compton subtraction method. However, FICS has several limitations. It produces only a point estimate for each bin in the unfolded spectrum without quantifying uncertainties. Furthermore, the method is prone to overfitting statistical noise and can introduce artificial structures into the reconstructed spectrum.

In the original software for decomposing ρ and $\mathcal{T}$, Schiller *et al.* [3] estimated the unfolding uncertainty as the ratio between the detector array's solid-angle coverage and its full-energy peak efficiency at a gamma-ray energy of 1.33 MeV [6]. Schiller *et al.* nevertheless cautioned that this estimate is "quite uncertain".

Midtbø *et al.* [7] developed a software implementation of the Oslo Method to estimate total statistical uncertainties using Monte Carlo simulations. In this approach, the data is resampled under the assumption of a Poisson distribution and processed through the standard Oslo Method. Confidence intervals are then derived from the mean and standard deviation of the resulting ensemble. However, this procedure relies on two critical assumptions: that the FICS unfolding procedure is unbiased and that the resulting ensemble is approximately Gaussian. As we will show, FICS is biased, and the Monte Carlo ensemble exhibits non-negligible higher-order moments, rendering confidence intervals based solely on the mean and standard deviation unreliable.

A fundamental property of the unfolding problem is that it is not identifiable. The detector response folds the underlying spectrum in a way that renders the inverse problem non-unique. Consequently, infinitely many mathematically distinct spectra are consistent with the same measured data. Any unfolding method must there-

[*] erlend.lima@fys.uio.no; a.c.larsen@fys.uio.no

fore select one solution among many, implicitly or explicitly through its regularization. Failure to recognize this can lead to over-interpretation of noise or regularization artifacts as genuine spectral structure.

In this article, we present a novel approach to the unfolding problem. Our method provides well-motivated and transparent uncertainty estimates for individual bins in gamma-ray spectra, offering unbiased results with confidence intervals calibrated to their stated confidence levels.

Our approach leverages regularized maximum likelihood estimation (RMLE) to recover the expectation value of the unfolded spectrum under physical constraints, rather than seeking arbitrary mathematical solutions that merely satisfy the folding relations. By prioritizing physically meaningful solutions, the method yields spectra that are robust against statistical noise. Its flexibility allows for principled statistical treatment of both background spectra and contaminants. Importantly, this robustness comes without computational cost: the method efficiently unfolds spectra with millions of bins in seconds on a standard desktop GPU.

Our analysis demonstrates that the spectral complexity of the input spectrum significantly influences the unfolding process. We establish a mathematical framework to classify spectra as either low- or high-complexity. For low-complexity spectra, our regularization approach yields reliable results with expected coverage levels. Overall, the method produces smoother spectra and achieves more accurate confidence interval coverage than the ensemble method of Midtbø [7]. While high-complexity spectra pose fundamental challenges to regularization that our current methodology cannot fully address, they can still be unfolded in practice, though users should expect greater uncertainty and interpret potential spurious peaks with caution. The treatment of high-complexity spectra remains an open area for future research.

The article is organized as follows. In Sec. II, we present a theoretical framework for the unfolding problem. The detector response functions are discussed in Sec. III, followed by theoretical and numerical implications of the ill-posedness and strategies for addressing it in Sec. IV. Our unfolding methodology is described in Sec. V, and the uncertainty quantification procedure is detailed in Sec. VI. Results on simulated data are presented in Sec. VII. A comparison to FICS is given in Sec. VIII. Finally, Sec. IX provides a summary and outlook.

The extensive theoretical treatment in these sections addresses a critical gap in the field, as many of the relevant mathematical and physical principles have previously been scattered across disparate papers in nuclear physics and other domains. By consolidating them into a unified framework, we aim to provide a solid foundation for future research and make the concepts more accessible to practitioners.

Appendix A provides relevant mathematical background, while Appendix B gives a mathematical description of fluctuations in gamma-ray spectra. Convergence conditions are presented in Appendix C. Appendix D outlines the theory behind marginal and simultaneous confidence intervals, and Appendix E discusses the mathematical basis of coverage probability. In Appendix F, we explain the Oslo Method and introduce typical experimental measurements using various reactions and detector types. Appendix G presents systematic results on regularization selection. Finally, the FICS method is derived and discussed in Appendix H.

This paper presents a complete theoretical framework from fundamentals through implementation. Recognizing that readers may have different needs, we suggest the following reading paths:

1. For practitioners mainly interested in implementing the method: Secs. V to VII provide a nearly self-contained description of the algorithm, implementation, and numerical results.

2. For those interested in method derivation without full theoretical foundations, Secs. III to IV develop the method for Oslo-type data.

3. Readers interested in the complete theoretical background should start with Sec. II.

II. THE UNFOLDING PROBLEM

A. The Poisson distribution and counting experiments

Experiments on atomic nuclei that produce gamma-ray emissions are commonly modeled as counting processes. These are mathematically described by Poisson point processes, which provide a natural framework for capturing the stochastic nature of event detection.

To develop a rigorous foundation for this model, we adopt a measure-theoretical framework where regions of observation are treated as *measurable*[1] subsets of the event space. We begin by examining individual events at a point-level, then extend the analysis to account for detector *smearing*[2] of the signal. When the average rate of occurrence remains constant, the Poisson distribution emerges as the natural model.

---

[1] The term *measure* used here refers to the mathematical concept in measure theory, specifically the Lebesgue measure, which provides a systematic way to assign "sizes" to sets, generalizing concepts like length, area, and volume. It should not be confused with physical measurements of energy or other detector observables.

[2] In this work, *smearing* refers to any process that redistributes or spreads out true values into observed measurements due to detector effects or measurement uncertainties. When specifically referring to smearing by a Gaussian distribution, we will explicitly use the term *Gaussian smearing*.

The Poisson distribution is defined as follows: Let Y be a random variable representing the number of events occurring in a fixed region.

Definition II.1 (Poisson Distribution) *A random variable Y is said to follow a Poisson distribution with parameter $\nu > 0$ if the probability of observing exactly y events is given by:*

$$P(Y = y \mid \nu) = \frac{\nu^y}{y!}e^{-\nu}\,. \tag{1}$$

The Poisson distribution has the following properties:

$$\mathbb{E}[Y] = \nu\,, \tag{2}$$
$$\mathbb{V}[Y] = \nu\,, \tag{3}$$

i.e., the mean and variance are given by the parameter ν, and for such Y we write

$$Y \sim \text{Poisson}(\nu)\,. \tag{4}$$

A natural question arises: Given that $Y \sim \text{Poisson}(\nu)$, what can be said about the parameter ν from the observation y? In this work, we will base our estimation on the maximum likelihood property:

Definition II.2 (Maximum Likelihood) *For a random variable $Y \sim \text{Poisson}(\nu)$, a maximum likelihood estimator (MLE) for ν, based on an observed count y, is the value $\hat{\nu}$ that maximizes the likelihood function*

$$\mathcal{L}(\nu) = \frac{\nu^y}{y!}e^{-\nu}\,, \tag{5}$$

satisfying the condition for any alternative $\tilde{\nu} \geq 0$

$$P(Y = y \,|\, \hat{\nu}) \geq P(Y = y \,|\, \tilde{\nu})\,. \tag{6}$$

In other words, an MLE $\hat{\nu}$ maximizes the probability to observe y, and a straightforward calculation yields that the MLE for ν is given by

$$\hat{\nu} = y\,, \tag{7}$$

which is an unbiased estimator, $\mathbb{E}[\hat{\nu} \,|\, \nu] = \nu$. This is known as *inference for direct observations*.

However, in real experiments, the detector will distort the underlying process. As a result, the observed data is a smeared representation of the truth-level[3] counts. In such cases, we deal with *inference for indirect observations*, where—in statistical terms—an unbiased solution can result in an unacceptable large variance [8]. This complication arises because the smearing transformation induced by the detector blur or mix the truth-level counts, making direct inversion unstable. The inference process then becomes more complex, and a closed

───────

[3] The term *truth-level* refers to the actual physical quantities or events before they are affected by detector resolution, efficiency, or other experimental effects.

form solution of the maximum likelihood estimator typically does not exist.

In the following, we wish to generalize from the discrete Poisson distribution to the Poisson point process in a continuous setting. Practical limitations ultimately force us to consider a discretized framework—for instance, by binning the energy spectrum into finite intervals. Nonetheless, our aim is to abstract away from any specific discretization so that the problem can be framed more generally.

B. Poisson point processes

We aim to model the detection of emitted gamma rays as a counting process, where the primary goal is to analyze how many events occur in specific energy regions. The appropriate mathematical tool for describing these types of processes is a point process. Essentially, a point process is a random mechanism that generates events within a continuous space.

Consider a state space $E \subseteq \mathbb{R}$, which represents the possible values for a physical observable of interest, e.g., energy. A point measure is a mathematical object that counts the number of events within a given set. For example, if we detect gamma rays at specific energies, the point measure tells us how many gamma rays are detected in a given energy range. To make this precise we need the following input:

- On a set E, a σ-algebra is a nonempty collection of subsets of E closed under complement, countable unions and countable intersections.

- A Borel σ-algebra on E, denoted $\mathcal{B}(E)$, is the smallest σ-algebra containing all open subsets of E.

- For a Borel set $B \in \mathcal{B}(E)$ and $x \in E$, a Dirac measure δ_x is defined by

$$\delta_x(B) = \begin{cases} 1, & x \in B, \\ 0, & x \notin B. \end{cases} \tag{8}$$

Then, we can define:

Definition II.3 (Point Measure) *A point measure χ on E is defined as*

$$\chi(B) = \sum_{i \in I} \delta_{x_i}(B)\,, \quad B \in \mathcal{B}(E)\,, \tag{9}$$

where I is a finite (or countable) index set and δ_{x_i} is the Dirac measure centered at the point $x_i \in E$, which counts whether the point x_i is in the set B.

A *point process* G is simply a random point measure, meaning that for each $B \in \mathcal{B}(E)$, the value $G(B)$ is a random integer that counts the number of points in B. For our purposes, the point process describes the random locations of gamma-ray detection events, and the

distribution of these events can vary depending on the underlying physical process.

The Poisson point process is a special type of point process that arises naturally in many experimental settings. It has two key properties:

1. For any Borel set B, the number of events $G(B)$ is a Poisson-distributed random variable with mean measure $\nu(B)$

$$G(B) \sim \text{Poisson}(\nu(B)) . \qquad (10)$$

2. The number of events in disjoint regions are independent.

The mean measure $\nu(B)$ represents the expected number of points $\nu(B) = \mathbb{E}[G(B)]$ in the region B, and is referred to as the mean measure of the process. This makes the Poisson process a good model for gamma-ray detection, where events occur independently, and the number of events in each region can be modeled using the Poisson distribution.

A key feature of the Poisson point process is the *intensity function* $f(x)$, which describes the expected rate of events at each point $x \in E$. In a small region around x, the expected number of events is approximately $f(x)\,dx$. Thus, the intensity function plays a role analogous to the parameter ν in the standard Poisson distribution, but with the added flexibility of varying across space, allowing for the modeling of non-uniform event distributions. The total expected number of events in a bounded Borel (measurable) subset B is given by

$$\nu(B) = \mathbb{E}[G(B)] = \int_B f(x)\,dx , \qquad (11)$$

where $G(B)$ denotes the number of events occurring in B.

To illustrate this, consider a one-dimensional interval $[a, b] \subset \mathbb{R}$. If the intensity function is constant, $f(x) = \nu$, the expected number of events becomes $\mathbb{E}[G([a, b])] = \nu(b - a)$. In this case, ν represents the constant event rate per unit length, and the total expected number of events is simply the product of the rate and the length of the region. This is known as a *homogeneous Poisson process*. When the intensity function varies with x, the process is referred to as an *inhomogeneous Poisson process*.

C. Poisson inverse problem

In real experiments we do not observe the true intensity function directly. Instead, we observe a smeared version of the process due to detector imperfections, where the observed intensity g is a blurred version of the truth-level intensity f. Performing inference in this scenario is referred to as a *Poisson inverse problem*, and generally falls into the class of *statistical ill-posed problems* [9].

To model this, let us consider two Poisson processes F and G. Let F denote the truth-level spectrum of events with $D \subseteq \mathbb{R}$ as state space, and let G denote the smeared spectrum of events with $E \subseteq \mathbb{R}$ as state space. We assume that both E and D are compact[4] intervals and we denote by $\mathcal{X}$ and $\mathcal{Y}$ spaces of regular[5] functions on D and E, respectively. Consider $f \in \mathcal{X}$ and $g \in \mathcal{Y}$ intensity functions of F and G. The intensity functions can then be related by a bounded[6] linear operator $\mathcal{R} : \mathcal{X} \to \mathcal{Y}$, giving the operator equation

$$\mathcal{R}(f) = g . \qquad (12)$$

Here, $\mathcal{R}$ is a linear operator whose *integration kernel* represents the response of a measuring device, e.g., the detector response. The detector response will act as a smoothing operation on the truth-level spectrum, resulting in an observed smeared spectrum. This may be modeled by assuming that the intensity functions are related by a Fredholm equation of the first kind,

$$g(y) = (\mathcal{R}f)(y) = \int_D R(y, x) f(x)dx , \qquad (13)$$

where R is a integration kernel[7] such that the integral is meaningful and the forward model is well-defined.

An inverse problem seeks to infer an unknown quantity from an indirect observation. This reconstruction task is often ill-posed; the stable solvability of a problem is given by:

Definition II.4 (Hadamard Criteria) *Let* $f \in \mathcal{X}$ *and* $g \in \mathcal{Y}$. *A problem is well-posed if the following conditions hold:*

(i) *Existence:* g *is in the* range *of the operator* $\mathcal{R}$, *i.e., there exists a solution* f *to* $\mathcal{R}(f) = g$.

(ii) *Uniqueness: The solution* f *is unique, implying that if* $\mathcal{R}(f) = \mathcal{R}(f')$ *then* $f' = f$.

———

[4] Compact means bounded and closed, e.g., for $a, b \in \mathbb{R}$ the interval $[a, b]$ is compact. All closed sets in $\mathbb{R}$ are Borel sets because the Borel σ-algebra includes all closed (and open) sets. Thus, every compact interval is a Borel set.

[5] Here, regular means sufficiently smooth functions, i.e., a function that has derivatives of sufficient order at each point in its domain.

[6] The distinction between bounded and unbounded operators is theoretical. In practice, especially in numerical computations, whether or not an operator is theoretically bounded is less critical than ensuring that the numerical methods are stable and the model is well-posed.

[7] An integration kernel $R(y, x)$ that makes Eq. (13) meaningful for all $f \in \mathcal{X}$ should be measurable in (y, x) with integrability conditions ensuring $(\mathcal{R}f)(y) = \int_D R(y, x)\,f(x)\,dx$ is well-defined and measurable for each $y \in E$ (for instance, this holds if $R \in L^2(E \times D)$ with $\mathcal{X} = \mathcal{Y} = L^2$). These assumptions (together with boundedness and linearity of $\mathcal{R}$) specify a valid forward model $g = \mathcal{R}f$; they do not, by themselves, imply that the inverse problem stated below is well-posed.

(iii) Stability: The solution f is a continuous function of g. Essentially, this means that a small change in $\mathcal{Y}$ leads to small changes in $\mathcal{X}$.

If any of these conditions are not met, the problem is deemed ill-posed. Most practical applications are in fact ill-posed problems.

Let us formulate this specifically for the problem at hand: The unfolding problem is to make inferences about the truth-level intensity f given a single observation[8] of the Poisson process G. In other words, the noise is modeled by regarding g as a parameter of an underlying statistical Poisson model. Given the stochastic nature of Poisson processes, we do not have access to an exact g, but can only construct an estimate $\hat{g}$ based on the observed data and try to solve Eq. (12) in an approximate sense. If we denote this approximate solution by $\hat{f}$, then it is possible that; *(i)* $\hat{g}$ is not in the range of $\mathcal{R}$ and $\hat{f}$ is not an exact solution, *(ii)* candidate solutions $\hat{f}$ map to the same $\hat{g}$, and *(iii)* $\hat{f}$ is not a continuous function of $\hat{g}$. In addition, even though the theoretical detector response is well-behaved, its practical implementation (e.g., discretization) does not necessarily carry this property. These practical limitations will most surely transform any well-behaved theoretical response to an ill-conditioned one, and with noise in the model, small perturbations in data-space may yield drastically different solutions in solution-space, and should therefore be regarded as unreliable.

In order to satisfy Hadamard's well-posedness conditions, one has to turn to regularization methods. Regularization methods—in the linear deterministic case—approach the ill-posedness in two different ways:

(1) **Implicit Regularization:** This approach is based on so-called iterative methods, which start with an initial estimate of the solution and refine this estimate through a series of iterations. Each iteration aims to reduce the discrepancy between the observed data and the model's predictions, incorporating regularization implicitly through the iteration process itself and the application of a stopping criterion.

(2) **Explicit Regularization:** This method proceeds in two conceptual steps:

   (i) **Generalized Inverses:** For a non-injective detector response, the naive inverse is not well-defined. To address multiple solutions, one replace inversion by a selection rule among data-consistent solutions (fixed by geometry and possible constraints). A standard approach introduce a generalized inverse, $\mathcal{R}^{\dagger}$,

and uses spectral/SVD projection to pick a canonical representative. For least squares, the Moore-Penrose pseudoinverse is one such selection (minimum norm in a Hilbert geometry) but is not stable in ill-posed settings.

   (ii) **Parametric Regularization:** To address the problem of instability, a family of continuous operators $\{\mathcal{R}_{\alpha}\}$ is introduced, such that for a regularization parameter $\alpha > 0$ the operators $\mathcal{R}_{\alpha}$ converge (in an appropriate topology) to the generalized inverse in the limit $\alpha \to 0$.

Ill-posed inverse problems are further compounded if the underlying model is probabilistic. This forces one to adapt the regularization methodology to a statistical setting, which may be classified as:

(1) **Frequentist Unfolding:** Treats unfolding as a point-estimation problem: choose a solution that best fits the data (e.g., via maximum likelihood or loss minimization) under physical constraints, while stabilizing the inversion through regularization. Regularization may be *explicit*—augmenting the objective with penalties that encode smoothness or shape—or *implicit*—through early stopping of iterative schemes. The regularization strength or stopping rule should be selected by data-driven rules (e.g. discrepancy principle, L-curve), and uncertainties can be quantified with frequentist tools such as bootstrap.

(2) **Bayesian Unfolding:**

This approach frames the unfolding problem in a purely probabilistic manner. Bayesian unfolding incorporates prior information about the solution and combines it with the observed data in a principled way:

   (1) **Prior Knowledge:** To regularize the ill-posed problem, one introduces a prior probability distribution over the space of possible solutions. This prior encodes any a priori knowledge about the expected smoothness, shape, or other properties of the solution. Priors that favor smooth or constrained solutions regularize the problem by penalizing unlikely solutions, thus addressing both non-uniqueness and instability.

   (2) **Posterior Distribution:** The observed data is modeled using a likelihood function, which accounts for the measurement process and the uncertainty in the observations. The posterior distribution is then obtained by applying Bayes' theorem, where the posterior reflects the updated belief about the solutions after observing the data.

---

[8] By single observation we mean that the experiment yields one spectrum.

In this work, the unfolding problem is approached using a frequentist methodology, with an emphasis on explicit regularization to obtain acceptable estimators. The most commonly used method for unfolding Oslo gamma-ray spectra, FICS, relies on implicit regularization.[9] The case of Bayesian unfolding will be addressed in a future work [10].

As we will see in Sec. III, trying to model the detector response as a pure smoothing operation will fail. That is, there are underlying nuclear processes that prevent the response from being a pure convolution operator, and standard deconvolution techniques are unsuitable.

Although the functional version of the unfolding problem is the most general, practical application necessitates a form that is amenable to computation. Therefore, we will next discretize the problem using histograms and discuss its ill-posedness in more detail.

D. Discretization and ill-posedness

The data in gamma-ray counting experiments are usually analyzed in binned form.[10] Thus, Poisson problems are predominantly examined in a format where both the observable process and the unobservable process are made discrete using histograms.

Recall, we consider two distinct Poisson processes, F and G, with intensity functions f and g, respectively. To discretize the smeared process G, we let $\{E_i\}_{i=1}^n$ be a partition of the smeared space E into n ordered intervals (energy bins). Similarly, for the truth-level process F, we let $\{D_i\}_{i=1}^n$ be a partition of the truth-level space D. Furthermore, we let y_i denote the number of points falling within interval E_i, denoted $y_i = G(E_i)$, resulting in a random vector

$$\mathbf{y} = [G(E_1), \dots, G(E_n)] = [y_1, \dots, y_n], \qquad (14)$$

i.e., the y_i's represent independent and Poisson distributed event counts. Then, we consider mean measures $\mu(D_i)$ and $\nu(E_i)$, such that we may construct mean vectors

$$\boldsymbol{\nu} = [\nu(E_1), \dots, \nu(E_n)] = \left[\int_{E_1} g(y)dy, \dots, \int_{E_n} g(y)dy \right] \qquad (15)$$

$$\boldsymbol{\mu} = [\mu(D_1), \dots, \mu(D_n)] = \left[\int_{D_1} f(x)dx, \dots, \int_{D_n} f(x)dx \right], \qquad (16)$$

where $\boldsymbol{\nu} \in \mathbb{R}_+^n$ represents the mean of the smeared histogram $\mathbf{y}$, and $\boldsymbol{\mu} \in \mathbb{R}_+^n$ represents the mean of some unobservable truth-level spectrum

$$\mathbf{x} = [F(D_1), \dots, F(D_n)]. \qquad (17)$$

We demand these vectors to belong to the non-negative orthant $\mathbb{R}_+ = \{x \in \mathbb{R} \,|\, x \geq 0\}$ because negative counts are not physically possible.

The discretized unfolding problem then takes the following form: Given an observed smeared spectrum $\mathbf{y}$ and the model

$$\mathbf{y} \sim \text{Poisson}\left(\mathbf{R}\boldsymbol{\mu} = \boldsymbol{\nu}\right), \qquad (18)$$

what can be said about the means $\boldsymbol{\mu}$ of the truth-level spectrum $\mathbf{x}$? As indicated, the mean vectors are related by the matrix equation

$$\mathbf{R}\boldsymbol{\mu} = \boldsymbol{\nu}, \qquad (19)$$

where the matrix $\mathbf{R}$ is the discretized version of the integral kernel in Eq. (13), representing *migration probabilities*.[11] For an *ill-conditioned*[12] smearing matrix $\mathbf{R}$, whose specific construction will be discussed in Sec. III, an estimator $\hat{\boldsymbol{\mu}}$ is difficult to obtain. Inferences for this model will be addressed in the next section.

It is important to note that for finite-dimensional systems a bijective $\mathbf{R}$ yields necessarily well-posedness essentially as an application of the Fredholm alternative.[13] In other words, such finite-dimensional linear problems are not ill-posed in the sense that they violate the third condition of Hadamard's definition. The main issue in such cases is that, due to an ill-conditioned $\mathbf{R}$, the solution will overfit to noise.

To evaluate the scope of the issue, let us model the noise as the discrepancy between the data and the model prediction

$$\mathbf{y} = \mathbf{R}\boldsymbol{\mu} + \boldsymbol{\epsilon}. \qquad (20)$$

Here, $\boldsymbol{\epsilon}$ represents the statistical noise in the observed data $\mathbf{y}$, accounting for discrepancies between the actual measurements and the model prediction $\mathbf{R}\boldsymbol{\mu}$. Each component ϵ_i of the noise vector corresponds to the deviation

---

[9] A detailed exposition of this method is provided in Appendix H.

[10] This is the most practical way to store the experimental data, but note that there is nothing fundamental about this choice. Also, the truth-level spectrum does not need to be restricted to histograms, e.g., another popular choice is splines. Nevertheless, for practical purposes, this is the choice we make.

[11] Migration probabilities represent the probabilities that events originating in specific bins of the truth-level spectrum are observed in particular bins of the smeared spectrum due to detector effects such as resolution limitations and inefficiencies. Each element R_{ij} of the matrix $\mathbf{R}$ corresponds to the probability that an event in the j-th truth-level bin is reconstructed in the i-th observed bin. Thus, the matrix $\mathbf{R}$ encodes the expected *migration* of events between bins because of the detector response.

[12] This means that the matrix has a high condition number, as defined in Definition II.5.

[13] In finite dimensions, the Fredholm alternative simplifies to statements about the rank and nullity of $\mathbf{R}$ and is closely related to the Rank-Nullity Theorem.

in the i-th bin, arising from inherent statistical fluctuations. Under the assumption of large number of counts, the Poisson distribution approaches a Gaussian distribution due to the Central Limit Theorem. In this regime, ϵ can be modeled as a vector of independent Gaussian random variables with zero mean and variances equal to the expected counts, that is,

$$\epsilon_i \sim \mathcal{N}(0, \nu_i), \quad \text{where} \quad \nu_i = (\mathbf{R}\boldsymbol{\mu})_i. \tag{21}$$

It is important to note that while this additive noise model is an approximation—since Poisson noise is signal-dependent and not strictly additive—it captures the essential features of the ill-posedness we expect to encounter.

Since we cannot satisfy $\mathbf{y} = \mathbf{R}\boldsymbol{\mu}$ exactly, and there are possibly multiple $\boldsymbol{\mu}$, we seek a solution that approximates this equation. Let us handle this using the explicit regularization methodology: The first step is to ensure the existence of a solution, and if multiple solutions exist, we need to establish a notion of uniqueness. Once uniqueness is addressed, we then tackle potential instability by further refining the solution with supplementary information, thereby enhancing the robustness of the reconstruction.

A solution that always exists is the *least squares* solution[14]:

$$\hat{\boldsymbol{\mu}}_{\text{LS}} = \underset{\boldsymbol{\mu} \in \mathbb{R}^n}{\arg\min} ||\mathbf{R}\boldsymbol{\mu} - \mathbf{y}||^2, \tag{22}$$

but for rank deficient and ill-conditioned $\mathbf{R}$, this solution is not unique and extremely unstable. The existence and non-uniqueness of the least squares solution, and a possible bound on the reconstruction may be quantified from the following theorem utilizing the Moore-Penrose pseudoinverse (see Appendix A 2).

Theorem II.1 *Let* $\mathbf{R} \in \mathbb{R}^{n \times n}$ *be a matrix with non-trivial null space* $\text{Ker}(\mathbf{R})$. *Then, all the least squares solutions are of the form*

$$\boldsymbol{\mu}_{\text{LS}} = \boldsymbol{\mu}_0 + \boldsymbol{\lambda}, \tag{23}$$

which is a sum of a particular and a homogeneous solution

$$\boldsymbol{\mu}_0 = \mathbf{R}^\dagger \mathbf{y} \in \mathbb{R}^n \tag{24}$$

$$\boldsymbol{\lambda} = (\mathbf{I} - \mathbf{R}^\dagger \mathbf{R})\mathbf{v} \in \text{Ker}(\mathbf{R}), \quad \mathbf{v} \in \mathbb{R}^n, \tag{25}$$

where $\mathbf{R}^\dagger$ *is the Moore-Penrose pseudoinverse and* $\mathbf{I} - \mathbf{R}^\dagger \mathbf{R}$ *is the orthogonal projection onto* $\text{Ker}(\mathbf{R})$.

Proof: The proof can be found in Appendix A 3.

$\square$

For $\mathbf{R}$ of full column rank and square, the Moore-Penrose pseudoinverse reduces to the standard inverse, and the least squares estimator reduces to $\hat{\boldsymbol{\mu}}_{\text{LS}} = \mathbf{R}^\dagger \mathbf{y} = \mathbf{R}^{-1}\mathbf{y}$, which is unique:

Corollary II.2 *The least squares solution* $\hat{\boldsymbol{\mu}}_{LS}$ *is unique if and only if the null space is empty, i.e.,* $\text{Ker}(\mathbf{R}) = \{\mathbf{0}\}$.

Proof: See Appendix A 4.

$\square$

Even if we obtain a unique solution, and *if* the noise $\epsilon \in \text{Ran}(\mathbf{R})$,[15] the naive inversion will—depending on how ill-conditioned $\mathbf{R}$ is—fit to noise and the reconstructed estimator $\hat{\boldsymbol{\mu}}_{\text{LS}}$ may be far from the truth-level value $\boldsymbol{\mu}$. In most cases, however, the noise $\epsilon \notin \text{Ran}(\mathbf{R})$, which further compounds the problem.

Let us show this explicitly: the measure for the stable solvability of the problem is the *condition number*, $\text{Cond}(\mathbf{R})$:

Definition II.5 *(Condition Number)*

- *For a square matrix* $\mathbf{R} \in \mathbb{R}^{n \times n}$ *of full column rank, the condition number with respect to the matrix norm* $|| \cdot ||$ *is defined as:*

$$\text{Cond}(\mathbf{R}) = ||\mathbf{R}|| \cdot ||\mathbf{R}^{-1}||. \tag{26}$$

- *For a square matrix* $\mathbf{R} \in \mathbb{R}^{n \times n}$ *with rank deficiency, the Moore-Penrose pseudoinverse may be used to define:*

$$\text{Cond}(\mathbf{R}) = ||\mathbf{R}|| \cdot ||\mathbf{R}^\dagger||. \tag{27}$$

Then, if we use the *Singular Value Decomposition* (SVD), the condition number can be written as

$$\text{Cond}(\mathbf{R}) = \frac{\sigma_{\max}}{\sigma_{\min}}, \tag{28}$$

where $\sigma_{\max}$ is the largest singular value and $\sigma_{\min}$ is the smallest non-zero singular value of $\mathbf{R}$.[16] If we (for simplicity) assume a normalization such that $||\mathbf{R}|| = \sigma_{\max} = 1$, and that the noise in Eq. (20) satisfy $||\epsilon|| \leq \epsilon$,[17] we can for full column rank $\mathbf{R}$ estimate the difference in the reconstruction

$$||\hat{\boldsymbol{\mu}}_{\text{LS}} - \boldsymbol{\mu}|| = ||\mathbf{R}^{-1}\epsilon|| \leq ||\mathbf{R}^{-1}|| \cdot ||\epsilon||, \tag{29}$$

---

[14] Throughout, $|| \cdot ||$ denotes the Euclidean vector norm $|| \cdot ||_2$; for matrices, $||A||$ denotes the induced operator (spectral) norm $||A||_{2 \to 2}$.

[15] A non-invertible $\mathbf{R}$ implies that its range is a proper subspace of $\mathbb{R}^n$, making it highly probable for a randomly oriented noise vector ϵ to lie outside this range. That is, proper subspaces of $\mathbb{R}^n$ have Lebesgue measure zero in $\mathbb{R}^n$, so the probability of ϵ being exactly within the range is zero if ϵ is drawn from a distribution with full support in $\mathbb{R}^n$.

[16] For $\mathbf{R}$ of full column rank all singular values are non-zero, but not for rank-deficient matrices and therefore the definition only makes sense if we choose the smallest non-zero singular value.

[17] Note that for a background vector $\mathbf{b}$ this would be $||\mathbf{b}|| \leq b$.

giving that

$$||\hat{\boldsymbol{\mu}}_{\text{LS}} - \boldsymbol{\mu}|| \leq \text{Cond}(\mathbf{R})\epsilon \,. \qquad (30)$$

Geometrically, this inequality defines a *ball* around the true solution $\boldsymbol{\mu}$ within which $\hat{\boldsymbol{\mu}}$ must lie, and the radius of the ball is scaled by $\text{Cond}(\mathbf{R})$. The implication is that a large condition number renders the reconstructed estimator far from the true value, *even if the noise is small.*

Furthermore, if $\mathbf{R}$ is not of full column rank (non-invertible) and simultaneously ill-conditioned, the instability of the solution is exacerbated. In this case, a similar calculation using the Moore-Penrose pseudoinverse yields that the difference in the reconstruction takes the form

$$||\hat{\boldsymbol{\mu}}_{\text{LS}} - \boldsymbol{\mu}|| \leq \text{Cond}(\mathbf{R})\epsilon + ||\boldsymbol{\lambda}|| \,, \qquad (31)$$

for some null-space vector $\boldsymbol{\lambda} \in \text{Ker}(\mathbf{R})$. Geometrically, the solution is therefore part of a tube-like region extending in directions defined by $\text{Ker}(\mathbf{R})$, allowing unbounded deviations.

In other words, for $\mathbf{R}$ of full column rank, we can always establish a bound on the difference that is proportional to $\text{Cond}(\mathbf{R})$, ensuring that the estimated solution $\hat{\boldsymbol{\mu}}$ remains within a controlled vicinity of the true solution $\boldsymbol{\mu}$. However, when $\mathbf{R}$ is not of full column rank, no such bound can guarantee the proximity of $\hat{\boldsymbol{\mu}}$ to $\boldsymbol{\mu}$. In this scenario, the presence of a non-trivial null space allows solutions to deviate arbitrarily from the true value, thereby increasing the instability of the reconstruction.

Another challenge is the occurrence of negative components in the solution, which are physically impossible. That is, null space vectors can often contain components that are both positive and negative, and their amplification results in unphysical solutions:

Proposition II.3 *Let* $\mathbf{R} \in \mathbb{R}^{n \times n}$ *be a non-negative matrix,* $R_{ij} \geq 0$ *for all* i, j, *with no zero rows or columns, and suppose that* $\mathbf{R}$ *has a non-trivial null space. Then any non-zero vector* $\boldsymbol{\lambda} \in \text{Ker}(\mathbf{R})$ *must have both positive and negative components.*

Proof: See Appendix A 5

□

This result implies that any reconstruction method involving matrices $\mathbf{R}$ with the stated properties, and that fails to mitigate the influence of null space vectors, will inevitably produce solutions with unphysical features.

Another challenge is the proper treatment of the background spectrum. Simply subtracting the background can amplify the background error, in direct analogy with the additive noise model Eq. (20). In the presence of a background $\mathbf{b} = \boldsymbol{\beta} + \boldsymbol{\epsilon}_\beta$ with additive noise $\boldsymbol{\epsilon}_\beta$, Eq. (20) becomes

$$\mathbf{y} = \mathbf{R}\boldsymbol{\mu} + \boldsymbol{\epsilon} + \boldsymbol{\beta} + \boldsymbol{\epsilon}_\beta \,. \qquad (32)$$

Since $\mathbf{b}$ is not directly observable, the naive approach is to subtract an estimate $\hat{\mathbf{b}}$ from $\mathbf{y}$, yielding

$$\tilde{\mathbf{y}} = \mathbf{R}\boldsymbol{\mu} + \boldsymbol{\epsilon} + \boldsymbol{\beta} + \boldsymbol{\epsilon}_\beta - \hat{\mathbf{b}} \,. \qquad (33)$$

The resulting background error,

$$||\mathbf{b} - \hat{\mathbf{b}}|| = ||\boldsymbol{\beta} + \boldsymbol{\epsilon}_\beta - \hat{\mathbf{b}}|| \,, \qquad (34)$$

acts as an additional source of additive noise. As in Eq. (30) and Eq. (31), this error is amplified by the condition number. In general, any attempt to subtract away unwanted structure without accounting for its uncertainty will destabilize the reconstruction, by analogous argument.

In conclusion, a large condition number indicates an ill-conditioned problem with a high potential for noise amplification. In finite-dimensional settings, noise may be present in the data, but it is the ill-conditioning that makes the reconstruction highly sensitive to such noise, potentially causing the solution to fit noise rather than signal. Importantly, a large condition number reflects fundamental sensitivity to *any* perturbation—whether from measurement error, modeling inaccuracies, or numerical instability. Ill-conditioned problems therefore require careful handling, typically through regularization. Moreover, if the response matrix is rank-deficient, the problem also lacks uniqueness. In such cases, additional constraints or regularization are essential to avoid inaccurate or unphysical solutions.

E. Tikhonov regularization

Having established the challenges posed by ill-conditioning and potential rank deficiency in the discretized unfolding problem, we now turn to regularization techniques designed to yield stable and physically meaningful solutions. One prominent strategy involves incorporating prior knowledge or desired properties of the solution (e.g., non-negativity) are incorporated directly into the problem formulation, typically by adding a penalty term to an objective function like the least squares criterion.

To get around the non-uniqueness of the least squares solution, we observe that the set of all solutions in Theorem II.1

$$\mathcal{N} = \{\boldsymbol{\mu}_{\text{LS}} = \mathbf{R}^\dagger \mathbf{y} + \boldsymbol{\lambda} \,|\, \boldsymbol{\lambda} \in \text{Ker}(\mathbf{R})\} \,, \qquad (35)$$

is a closed convex set.[18] Hence, we may use the *closest-point theorem*, which states that there exists a unique point in $\mathcal{N}$ corresponding to the minimum norm solution, i.e.,

$$\hat{\boldsymbol{\mu}}_{\text{MNLS}} = \underset{\boldsymbol{\mu}_{\text{LS}} \in \mathcal{N}}{\arg\min} ||\boldsymbol{\mu}_{\text{LS}}|| = \mathbf{R}^\dagger \mathbf{y} \,, \qquad (36)$$

---

[18] The solution set is convex because any convex combination of solutions remains a solution. The solution set is an affine subspace, and in finite-dimensional settings, affine subspaces are closed. This means they contain all their limit points, ensuring that the solution set is topologically closed.

is called the *minimum norm least squares estimator* and is unique, but again, even though a unique solution exists, noise amplification might still be a problem. To remedy this, we seek a smooth cut-off of the singular values such that the estimates $||\hat{\boldsymbol{\mu}} - \boldsymbol{\mu}||$ are dampened. As we have already obtained a notion of a unique solution, we can achieve such a smooth cut-off by considering a solution that continuously converge to the minimum norm least squares solution.

Theorem II.4 *Let $\alpha > 0$ be a constant. For the least squares problem $\mathbf{y} = \mathbf{R}\boldsymbol{\mu}$, where $\mathbf{R} \in \mathbb{R}^{n \times n}$, consider the regularized solution defined by:*

$$\hat{\boldsymbol{\mu}}_\alpha = \arg\min_{\boldsymbol{\mu}} \left(||\mathbf{y} - \mathbf{R}\boldsymbol{\mu}||^2 + \alpha||\boldsymbol{\mu}||^2 \right). \qquad (37)$$

Then:

1. Uniqueness: *The solution*

$$\hat{\boldsymbol{\mu}}_\alpha = (\mathbf{R}^{\mathrm{T}}\mathbf{R} + \alpha\mathbf{I})^{-1}\mathbf{R}^{\mathrm{T}}\mathbf{y}, \qquad (38)$$

   exists and is unique for all $\alpha > 0$.

2. Limiting Case: *As $\alpha \to 0$, the regularized solution $\hat{\boldsymbol{\mu}}_\alpha$ continuously converges to the minimum norm least squares estimator*

$$\lim_{\alpha \to 0} ||\hat{\boldsymbol{\mu}}_\alpha - \hat{\boldsymbol{\mu}}_{\mathrm{MNLS}}|| = 0. \qquad (39)$$

3. Noise Dampening: *The regularization introduces a smooth cut-off of the singular values of $\mathbf{R}$, dampening the amplification of noise in the estimates. Specifically, using the Singular Value Decomposition*

$$\mathbf{R} = \sum_{i=1}^{\mathrm{rank}(\mathbf{R})} \sigma_i \mathbf{u}_i \mathbf{v}_i^{\mathrm{T}}, \qquad (40)$$

   the regularized expression can be expressed as:

$$\hat{\boldsymbol{\mu}}_\alpha = \sum_{i=1}^{\mathrm{rank}(\mathbf{R})} \frac{\sigma_i}{\sigma_i^2 + \alpha} \left(\mathbf{u}_i^{\mathrm{T}} \mathbf{y} \right) \mathbf{v}_i, \qquad (41)$$

   showing that each component of the solution is weighted by a factor that for $\alpha > 0$ dampens the impact of small singular values, mitigating noise amplification.

Proof: See Appendix A 6

□

The main insight from this result is that $\hat{\boldsymbol{\mu}}_\alpha$ is obtained by reconciling fitting to the data, and finding a solution with small norm. This type of regularized solution is most often called *Tikhonov regularization*, and it can be further generalized by adding any convex term $||\mathbf{L}\boldsymbol{\mu}||^2$, where $\mathbf{L}$ is referred to as a regularization matrix. Typically, generalized Tikhonov regularization employs $\mathbf{L}$ as a

discretized version of the first or second order derivative operator, such as ∇ or ∇^2. This form of regularization is particularly well-suited for smooth spectra, where the underlying signal is expected to vary gradually without abrupt changes.

In contrast, for spectra characterized by sparsity, Tikhonov regularization may fail to capture these sharp features adequately. In such cases, a regularization term that promotes sparsity is preferred. For example, incorporating an ℓ_1 norm penalty encourages many coefficients to be exactly zero, making it ideal for sparse solutions where only a few significant components are present. However, if the underlying signal is not only sparse but also contains sharp peaks, pure ℓ_1 regularization may inadvertently penalize these important features, leading to a loss of critical information. To address this, more sophisticated regularization techniques that balance sparsity with the preservation of sharp transitions must be employed.

With this demonstration, we have shown that an explicit regularization method can ensure stable and unique solutions. However, we anticipate several challenges if this method is naively applied to the relevant spectra in this study. One significant issue is that achieving a unique and stable solution required modifying the original problem through *normal equations*, which substantially increases the condition number. As a consequence it is extremely difficult to find an appropriate regularization and the reconstruction does not retain important physical structure. Additionally, the Tikhonov regularization applied to the least squares problem does not enforce the non-negativity constraint. The consequence of this is that while standard Tikhonov allows for a closed-form solution via normal equations, the addition of non-negativity constraints necessitates optimization techniques;[19] closed-form solutions are generally unattainable. While this is not a major problem in itself, as there exists customized optimization methods to handle this, the correct handling of the appropriate noise and background of the physical system is in general infeasible with this simple setup.

To obtain stable and accurate solutions, alternative strategies are necessary—specifically, incorporating explicit regularization techniques within an appropriate statistical framework that effectively handles relevant noise and background. That is, noise and background are stochastic and need to be treated as such. Therefore, we turn our attention towards *regularized maximum likelihood estimation* where these problems have an innate implementation.

———

[19] This is often called *regularized non-negative least squares* in the context of least squares estimation.

F. Regularized maximum likelihood estimation

Since we deal with Poisson distributed data, we are interested in performing maximum likelihood estimation for the mean $\boldsymbol{\mu}$. In the case of direct observation, the MLE had a closed form solution, but this is no longer the case for indirect observations.

Given the unfolding problem and data model

$$\mathbf{y} \sim \mathrm{Poisson}\left(\mathbf{R}\boldsymbol{\mu} = \boldsymbol{\nu}\right), \tag{42}$$

we construct the likelihood of the true mean histogram $\boldsymbol{\mu}$ as:

$$\mathcal{L}(\boldsymbol{\mu}|\mathbf{y}) = \prod_i \frac{\left(\sum_j R_{ij}\mu_j\right)^{y_i}}{y_i!} \exp\left(-\sum_j R_{ij}\mu_j\right), \tag{43}$$

which can equivalently be expressed in terms of the smeared histogram $\boldsymbol{\nu}$, through the relation $\mathbf{R}\boldsymbol{\mu} = \boldsymbol{\nu}$.

However, a challenge in applying maximum likelihood estimation here lies in the nonlinearity of the likelihood function in the constrained $\boldsymbol{\mu} \in \mathbb{R}_+^n$. This leads to a nonlinear constrained optimization problem that lacks a closed-form solution. This means that the MLE must be solved using numerical optimization methods, and due to $\mathbf{R}$ being rank-deficient and ill-conditioned, the existence and stability of the MLE must be carefully examined.

Instead of directly maximizing the likelihood function, we minimize the negative log-likelihood. The negative log-likelihood retains the same information as the likelihood through a monotonic transformation, which preserves the location of the optimal solution. Additionally, the transformation simplifies the optimization process by converting products into sums, making the problem more tractable, while also ensuring that the resulting problem is framed as a minimization.

For the model Eq. (43), the negative log-likelihood takes the form:

$$\ell(\boldsymbol{\mu}|\mathbf{y}) = \sum_i \left[\sum_j R_{ij}\mu_j - y_i \log\left(\sum_j R_{ij}\mu_j\right) \right] + \sum_i \log(y_i!), \tag{44}$$

where the last term is independent of $\boldsymbol{\mu}$ and does not affect the optimization process. The model requires $\boldsymbol{\nu} = \mathbf{R}\boldsymbol{\mu} \geq 0$, and for physical interpretation we must have that $\mathbf{R} \geq 0$, $\boldsymbol{\mu} \geq 0$. Given this, the task is to find the estimator

$$\hat{\boldsymbol{\mu}}_{\mathrm{MLE}} = \underset{\boldsymbol{\mu} \in \mathbb{R}_+^n}{\arg\min}\, \ell(\boldsymbol{\mu}|\mathbf{y}). \tag{45}$$

The negative log-likelihood has—under certain conditions—some very useful properties. First, however, it is useful to differentiate between two notions of indeterminacy in this model:

- *Identifiability (model-level)*: Different parameter values induce different distributions. This is a property of the statistical model, and independent of the data.

- *Uniqueness (estimator-level)*: Given data and a fitting rule, there exists only one solution to the optimization problem.

In the Poisson model Eq. (42), the smeared means $\boldsymbol{\nu}$ are identifiable, but the truth-level means become identifiable only when the matrix $\mathbf{R}$ has full column rank; by the identifiability of $\boldsymbol{\nu}$, it holds that $\mathbf{R}(\boldsymbol{\mu} - \boldsymbol{\mu}') = 0$, implying that the following set maps to the same $\boldsymbol{\nu}$

$$\{\boldsymbol{\mu} = \boldsymbol{\mu}_0 + \boldsymbol{\lambda} \,|\, \boldsymbol{\lambda} \in \mathrm{Ker}(\mathbf{R})\}, \tag{46}$$

which in general is a unphysical and unbounded set. The truth-level means $\boldsymbol{\mu}$ are therefore identifiable if and only if $\mathrm{Ker}(\mathbf{R}) = \{0\}$. However, it is not necessarily true that identifiability and uniqueness coincide.

To address uniqueness, we note that the non-negativity requirement changes the feasible set to a bounded one

$$\{\boldsymbol{\mu} = \boldsymbol{\mu}_0 + \boldsymbol{\lambda} \,|\, \boldsymbol{\lambda} \in \mathrm{Ker}(\mathbf{R})\} \cap \mathbb{R}_+^n, \tag{47}$$

preserving physicality (see Appendix A 7 for a demonstration), but it is difficult to further determine the impact of the non-negativity constraint beyond boundedness. However, if we assume that $\mathbf{R} \geq 0$ and that there are no zero rows in $\mathbf{R}$ for indices with $y_i > 0$[20], the following properties hold:

- The function $\ell(\boldsymbol{\mu}|\mathbf{y})$ attains a minimum over the feasible set of $\boldsymbol{\mu}$.

- The function $\ell(\boldsymbol{\mu}|\mathbf{y})$ is convex with respect to $\boldsymbol{\mu}$; thus, all local minima are global minima.

- If $\mathbf{R}$ has full column rank, $\ell(\boldsymbol{\mu}|\mathbf{y})$ is strictly convex and the solution is unique.

The existence of a minimum follows from the continuity and coercivity of $\ell(\boldsymbol{\mu}|\mathbf{y})$ over the closed domain $\mathbb{R}_+^n$. The convexity of the $\ell(\boldsymbol{\mu}|\mathbf{y})$ follows from the positive semi-definiteness of its Hessian matrix, and if $\mathbf{R}$ is of full column rank, the Hessian is positive definite and $\ell(\boldsymbol{\mu}|\mathbf{y})$ is strictly convex. In essence, the practical problem of indeterminacy has been reduced to possible rank-deficiency of the detector repsonse.

In summary: From the given properties of ℓ, we know that a solution exists, but it is not necessarily unique if $\mathbf{R}$ lacks full column rank. In optimization terms; the negative log-likelihood is convex but not strictly convex when $\mathbf{R}$ is rank-deficient. Additionally, if $\mathbf{R}$ is ill-conditioned,

---

[20] If some row i of $\mathbf{R}$ were identically zero while $y_i > 0$, the Poisson likelihood would be infinite for all $\boldsymbol{\mu} \geq 0$, and the problem would be infeasible.

the solution is highly sensitive to noise. As we have established, this will cause a multitude of problems in the optimization. In contrast to the least squares method, the non-negative constraint is inherent when using likelihoods, since the likelihood is only defined for $\boldsymbol{\nu} \geq 0$. From this, physical requirements sets non-negativity constraint on $\mathbf{R}$ and $\boldsymbol{\mu}$. While these constraints reduces the feasible set of solutions and narrows the search space, it does not eliminate the occurrence of multiple solutions.

By adding a regularization term, the number of possible solutions and noise amplification in the feasible set is expected to be further reduced and dampened. In general, the objective is therefore to find the regularized estimator

$$\hat{\boldsymbol{\mu}}_{\mathrm{RMLE}} = \underset{\boldsymbol{\mu} \in \mathbb{R}_+^n}{\arg \min} \left(\ell(\boldsymbol{\mu}|\mathbf{y}) + \Omega(\boldsymbol{\mu}; \boldsymbol{\alpha}) \right), \qquad (48)$$

where $\Omega(\boldsymbol{\mu}; \boldsymbol{\alpha})$ is the appropriate regularization term(s) for a given spectrum with regularization parameter(s) $\boldsymbol{\alpha}$.

Having established the ill-posed nature of the unfolding problem and the role of the detector response $\mathbf{R}$ in smearing the truth-level spectrum, the next step is to examine this matrix in detail. Section 3 describes the physical basis of the detector response and explains how particle interactions and detector effects give rise to the response matrix $\mathbf{R}$.

III. THE DETECTOR RESPONSE

The experimental data analyzed in this work is structured as two-dimensional histograms, giving rise to a matrix structure $\mathbf{Y} \in \mathbb{R}^{m \times n}$ for the data (see Appendix F for the experimental setup). To model this, we recall from Section II C that F and G are two distinct Poisson processes with corresponding intensity functions f and g. F models the truth-level process and G models the smeared process. The rows E are partitioned into m ordered intervals $\{E_i\}_{i=1}^m$ and the columns E' into n ordered intervals $\{E'_j\}_{j=1}^n$, where each pair (E_i, E'_j) defines a grid cell $E_i \times E'_j$. For each grid cell $E_i \times E'_j$, we let Y_{ij} denote the number of events falling into that cell, $Y_{ij} = G(E_i \times E'_j)$, resulting in a stochastic matrix

$$\mathbf{Y} = \begin{bmatrix} Y_{11} & Y_{12} & \ldots & Y_{1n} \\ Y_{21} & Y_{22} & \ldots & Y_{2n} \\ \vdots & \vdots & \ddots & \vdots \\ Y_{m1} & Y_{m2} & \ldots & Y_{mn} \end{bmatrix} \in \mathbb{R}_+^{m \times n}. \qquad (49)$$

From the mean measures

$$\mu_{ij} = \mu(D_i \times D'_j) = \int_{D_i \times D'_j} f(x, z) \, dx dz \qquad (50)$$

$$\nu_{ij} = \nu(E_i \times E'_j) = \int_{E_i \times E'_j} g(y, w) \, dy dw, \qquad (51)$$

we construct the mean matrices

$$\boldsymbol{\mu} = \begin{bmatrix} \mu_{11} & \mu_{12} & \ldots & \mu_{1n} \\ \mu_{21} & \mu_{22} & \ldots & \mu_{2n} \\ \vdots & \vdots & \ddots & \vdots \\ \mu_{m1} & \mu_{m2} & \ldots & \mu_{mn} \end{bmatrix} \in \mathbb{R}_+^{m \times n}. \qquad (52)$$

$$\boldsymbol{\nu} = \begin{bmatrix} \nu_{11} & \nu_{12} & \ldots & \nu_{1n} \\ \nu_{21} & \nu_{22} & \ldots & \nu_{2n} \\ \vdots & \vdots & \ddots & \vdots \\ \nu_{m1} & \nu_{m2} & \ldots & \nu_{mn} \end{bmatrix} \in \mathbb{R}_+^{m \times n}. \qquad (53)$$

To describe the smearing process, we must separate the smearing across the rows and the smearing across the columns. This can be represented by a double-sided matrix equation

$$\mathbf{R}_1 \boldsymbol{\mu} \mathbf{R}_2 = \boldsymbol{\nu}, \qquad (54)$$

where $\mathbf{R}_1 \in \mathbb{R}^{m \times m}$ describes the smearing along the row dimension and $\mathbf{R}_2 \in \mathbb{R}^{n \times n}$ describes the smearing along the column dimension, giving rise to the matrix model

$$\mathbf{Y} \sim \mathrm{Poisson}(\mathbf{R}_1 \boldsymbol{\mu} \mathbf{R}_2 = \boldsymbol{\nu}). \qquad (55)$$

The detector response consists of two distinct transformations: row-wise smearing $\mathbf{R}_1$ modeling gamma-ray detection, and column-wise smearing $\mathbf{R}_2$ modeling particle detection. A property of the OCL detector setup is that these transformations are independent — the gamma-ray detection (OSCAR) and particle detection (SiRi) are uncorrelated measurements. This independence can be seen in the experimental data as symmetric Gaussian peaks rather than rotated ellipses that would indicate correlation.

The particle detector response $\mathbf{R}_2 = \mathbf{G}_{\mathrm{in}}$ is modeled as a Gaussian smoothing matrix with constant resolution σ_{in}. The specific resolution depends on the experimental setup and particle type — for instance, the instrumental energy resolution when detecting protons (at forward angles) in SiRi [11] is approximately $150 \, \mathrm{keV}$ (full width at half maximum, FWHM).

The gamma-ray detector response $\mathbf{R}_1$ can be factored as $\mathbf{R}_1 = \mathbf{G}_\gamma \mathbf{D}$, where $\mathbf{D}$ is a discrete response matrix capturing the fundamental detector physics, and $\mathbf{G}_\gamma$ is a smoothing matrix accounting for finite detector resolution. This factorization separates the distinct physical processes affecting gamma-ray detection into components that can be handled separately in the unfolding process.

The discrete response matrix $\mathbf{D}$ can be determined either through GEANT4 simulations [12] or experimental measurements. For the OSCAR array, we use GEANT4-simulated responses [13] as they provide better resolution than direct experimental measurements. Since the simulated response energies typically don't align with experimental spectrum binning, interpolation is required (see [1]).
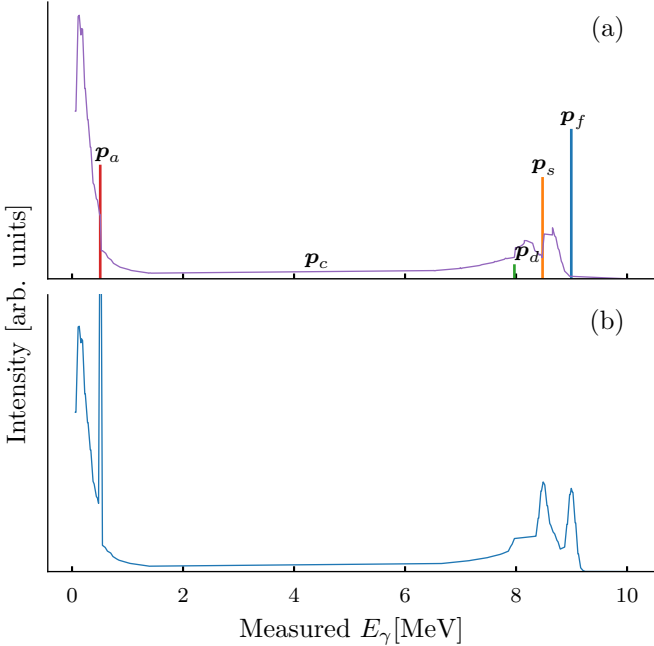
FIG. 1: (a) Each component of the discrete response for true $E_\gamma = 9\,\text{MeV}$. The peaks have been scaled down to make them visually comparable. (b) A single sharp peak at $9\,\text{MeV}$ folded with $\mathbf{G}_\gamma\mathbf{D}$.

The gamma-detector physics is modeled by four discrete structures: the full energy peak ($\mathbf{p}_\text{f}$), which corresponds to the true energy of the incoming gamma-ray; the single escape peak ($\mathbf{p}_\text{s}$); the double escape peak ($\mathbf{p}_\text{d}$); and the annihilation peak ($\mathbf{p}_\text{a}$). In addition, there is a continuum composed of Compton scattering, backscatter, and low-energy processes. This continuum is traditionally referred to as the *Compton background* ($\mathbf{P}_c$). The top panel of Fig. 1 illustrates the components for a single true gamma energy, as a function of measured gamma energy.

The discrete response $\mathbf{D}$ is the matrix sum of these components. By construction, $\mathbf{D}$ is row-stochastic, with each row normalized to unity:

$$\sum_{j=1}^{m} D_{ij} = 1 \quad \forall i = 1, 2, \ldots, m. \qquad (56)$$

The last element of the ith row of $\mathbf{D}$ is the element $(p_\text{f})_i$ of $\mathbf{p}_\text{f}$, located at the diagonal entry D_{ii}, which makes $\mathbf{D}$ a lower triangular matrix. The other vector components are thus placed below the main diagonal: $\mathbf{p}_\text{s}$ is placed along the subdiagonal corresponding to 511 keV below the full energy peak, $\mathbf{p}_\text{d}$ placed along the subdiagonal corresponding to $2 \cdot 511$ keV below the full energy peak and $\mathbf{p}_\text{a}$ is placed along the column corresponding to 511 keV. Given such a structure, the vector components may be embedded into a matrix as:
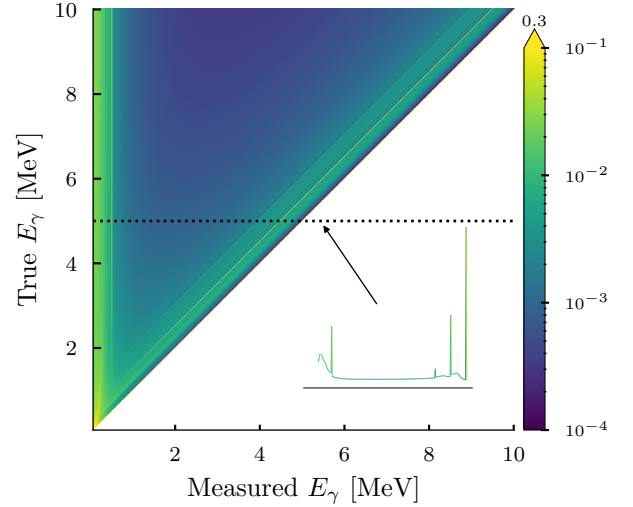

FIG. 2: The discrete OSCAR response $\mathbf{D}$ for a 1000×1000 matrix. The discrete peaks $\mathbf{p}_\text{f}, \mathbf{p}_\text{s}$ and $\mathbf{p}_\text{d}$ are along the diagonal and at offsets $511\,\text{keV}$ and $1024\,\text{keV}$, respectively. The $\mathbf{p}_\text{a}$ is a sharp vertical structure at measured $E_\gamma = 511\,\text{keV}$. The remaining bulk is the $\mathbf{P}_\text{c}$ component. The inset axes shows an example of a single row at true $E_\gamma = 5\,\text{MeV}$. The color scale is logarithmic, scaled to prevent outlying bins from affecting the color. The numbers on the colorbar indicate 0.3% of the bins lie above the range.

$$\mathbf{P} = \sum_{k=0}^{m-1} \text{diag}_k(\mathbf{p}_k) + \sum_{j=1}^{m} \text{col}_j(\mathbf{q}_j), \qquad (57)$$

where the first sum places vectors along the k-th diagonal and the second sum places vectors into the j-th column. To preserve the lower triangular structure: for each column j, the entries $q_{j,i}$, corresponding to rows $i < j$ must be zero.

These diagonal and column components together with the Compton component yields the discrete matrix

$$\mathbf{D} = \mathbf{P}_\text{f} + \mathbf{P}_\text{s} + \mathbf{P}_\text{d} + \mathbf{P}_\text{a} + \mathbf{P}_\text{c}. \qquad (58)$$

The response matrix $\mathbf{D}$ for OSCAR is shown in Fig. 2.[21]

As $\mathbf{D}$ is a lower triangular matrix with all non-zero diagonal elements, it is theoretically full rank and invertible. In practice, however, $\mathbf{D}$ is not effectively full rank. Its condition number (Definition II.5) as function of matrix order is shown in Fig. 3. The value is near constant,

---

[21] While the matrix is mathematically lower triangular, it is displayed with reversed rows to show increasing energy on the y-axis, making it appear upper triangular in the figure.
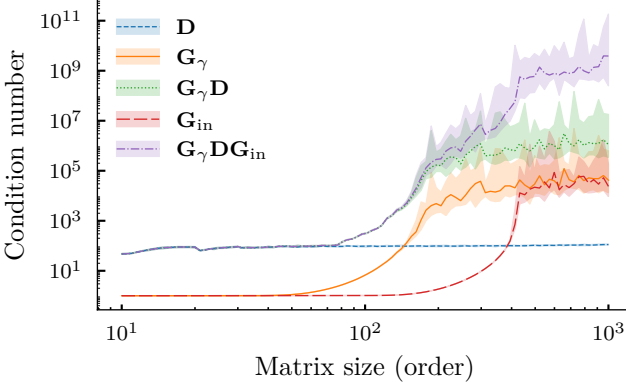
FIG. 3: Condition numbers versus matrix order for matrices $\mathbf{D}$, $\mathbf{G}_\gamma$, $\mathbf{G}_\gamma\mathbf{D}$, $\mathbf{G}_{\text{in}}$ and $\mathbf{G}_\gamma\mathbf{D}\mathbf{G}_{\text{in}}$. The smoothing operators $\mathbf{G}_\gamma$ and $\mathbf{G}_{\text{in}}$ exhibit substantially higher condition number growth with increasing order than $\mathbf{D}$. Shaded bands represent the range of condition numbers across 100 instances with small perturbations, simulating numerical fluctuations in matrix construction. The resolution is held constant at $\sigma_{\text{in}} = 40\,\text{keV}$ and $\sigma_\gamma(1330\,\text{keV}) = 40\,\text{keV}$. The energy range is from 0 to 10 MeV, with ΔE determined by the order.

but too large to be considered well-conditioned. Therefore, we must effectively treat the discrete response $\mathbf{D}$ as being rank-deficient and ill-conditioned.

To model the smearing, we use a Gaussian smoothing matrix $\mathbf{G} \in \mathbb{R}^{n \times n}$, defined element-wise as

$$G_{ij} = \frac{1}{Z_i} \exp\left[-\frac{(E_j - E_i)^2}{2\sigma(E_i)^2} \right], \tag{59}$$

with the normalization[22]

$$Z_i = \sum_{k=1}^{n} \exp\left[-\frac{(E_j - E_i)^2}{2\sigma(E_i)^2} \right]. \tag{60}$$

Here $\mathbf{E} = \{E_1, E_2, \ldots, E_n\}$ represents the energy bins, and $\sigma(E_i)$ denotes the resolution. Each row $\mathbf{G}_i$ of $\mathbf{G}$ corresponds to a Gaussian centered at E_i. The normalization constant Z_i ensures that the sum of elements in each row, $\sum_{j=1}^{n} G_{ij} = 1$, thereby making $\mathbf{G}$ row-stochastic. The $\mathbf{G}$ matrices for OSCAR and SiRi are given in Fig. 4.

As the bin width ΔE of $\mathbf{E}$ narrows, the rows become increasingly similar, compromising their linear independence:

---

[22] This normalization is valid only when unfolding the full spectrum. If only a subregion is unfolded, the normalization must account for smearing into unobserved lower-energy regions. In practice, the most straightforward approach is to construct the full matrix G_{ij} as described and then extract the relevant submatrix.
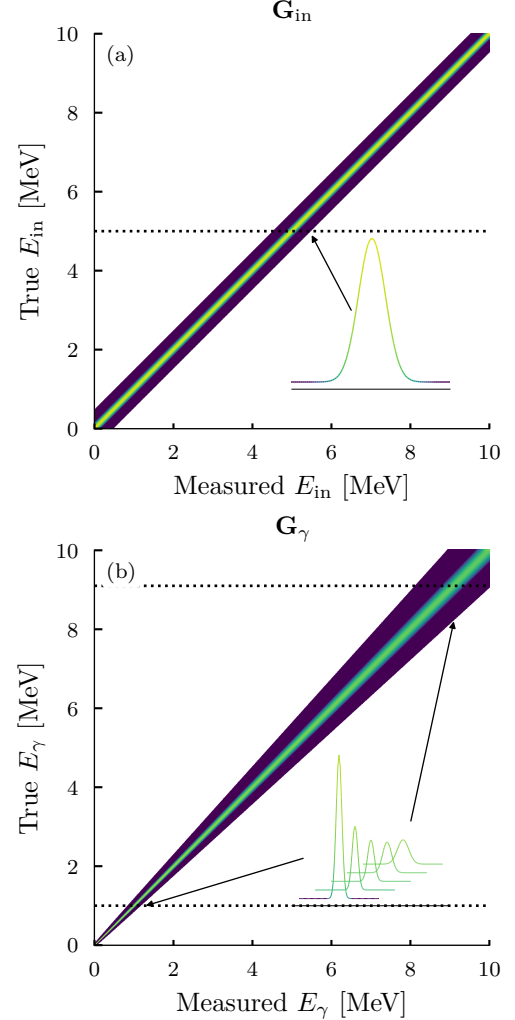

FIG. 4: Examples of smoothing matrices for the initial-excitation-energy axis, $\mathbf{G}_{\text{in}}$ (a), and gamma-ray-energy axis, $\mathbf{G}_\gamma$ (b). The inset axes show examples of the Gaussians at specific true energies marked with dotted lines. The color scale (not shown) is logarithmic with 0 mapped to white.

1. As ΔE becomes much smaller than σ, the Gaussian functions centered at adjacent energy bins overlap significantly. Consequently, the rows of $\mathbf{G}$ becomes nearly identical, leading to effective linear dependence. $\mathbf{G}$ loses its full rank and becomes non-invertible.

2. When ΔE is much larger than σ, the Gaussian functions centered at each energy bin have minimal overlap. The rows of $\mathbf{G}$ remain distinct and linearly independent. As a result, $\mathbf{G}$ maintains full rank and remains invertible.

In the regime where $\Delta E \gg \sigma$, the Gaussian distributions centered at E_i and E_{i+1} have negligible overlap. Each row $\mathbf{G}_i$ and $\mathbf{G}_{i+1}$ is sharply peaked around E_i and

E_{i+1}, respectively. The difference between adjacent rows resembles the difference between two orthogonal unit vectors, and the distance saturates to

$$\|\mathbf{G}_{i+1} - \mathbf{G}_i\| \approx \sqrt{2}, \tag{61}$$

while for $\Delta E \ll \sigma$, adjacent rows significantly overlap, and by converting discrete sums to integrals, the distance obey the scaling behavior

$$\|\mathbf{G}_{i+1} - \mathbf{G}_i\| \approx \left(\frac{1}{4\sqrt{\pi}} \frac{\Delta E^3}{\sigma^3} \right)^{1/2}. \tag{62}$$

When the row distance becomes sufficiently small, floating point errors accumulate, leading to a rapid increase in the condition number of $\mathbf{G}$ and effective rank deficiency. Figure 5 demonstrates the ill-conditioning of $\mathbf{G}_\gamma$ and $\mathbf{G}_{\text{in}}$: at low σ, the row distance remains constant at $\sqrt{2}$. Once σ becomes comparable to ΔE, the distance decays linearly on a log-log scale, accompanied by a sharp increase in the condition number.

A direct consequence is that the inverse $\mathbf{G}^{-1}$ is not well defined. Figure 6 demonstrates the effective rank deficiency of $\mathbf{G}_\gamma$ in the form of $\mathbf{G}_\gamma \mathbf{G}_\gamma^{-1} \neq \mathbf{1}$. Instead of an identity matrix, the product fluctuates twelve orders of magnitude. The Moore-Penrose pseudoinverse $\mathbf{G}_\gamma \mathbf{G}_\gamma^\dagger = \mathbf{P_G} \approx \mathbf{1}$ is expected to be more well-behaved, which the lower panel confirms.

For the matrix $\mathbf{G}_{\text{in}}$, we set a constant width σ_{in}, which results in symmetric elements $(\mathbf{G}_{\text{in}})_{ij} = (\mathbf{G}_{\text{in}})_{ji}$. This symmetry of $\mathbf{G}_{\text{in}}$ is visible in the top panel of Fig. 4. If the values of $\boldsymbol{E}_{\text{in}}$ are equally spaced, $\mathbf{G}_{\text{in}}$ forms a symmetric Toeplitz matrix. Furthermore, when σ_{in} is sufficiently small, the elements rapidly decay to zero, resulting in an approximately banded symmetric Toeplitz matrix. These conditions are usually met in practice. Notably, all banded symmetric Toeplitz matrices commute, a desirable property when solving inverse problems.

In contrast, the resolution of the gamma-ray energy axis is modeled by a square root quadratic function [13]:

$$\sigma_\gamma := \sigma \left(E_\gamma \right) = \sqrt{a_0 + a_1 E_\gamma + a_2 E_\gamma^2}. \tag{63}$$

This energy dependency disrupts both the symmetry and the Toeplitz structure[23] of the resulting matrix $\mathbf{G}_\gamma$, and $\mathbf{G}_\gamma$-like matrices no longer commute. An example of a $\mathbf{G}_\gamma$ matrix is given in the bottom panel of Fig. 4.

These properties—non-commutativity of the response matrices and the degeneracies they introduce—can undermine the reliability of standard methods. In the next section, we demonstrate how these factors can lead to significant inaccuracies when conventional techniques are applied and present a framework to address these challenges effectively.

—————

[23] Convolutions are represented by (circular) Toeplitz matrices. Since our matrices do not have this structure, unfolding gamma-spectra should not be called *deconvolution*.
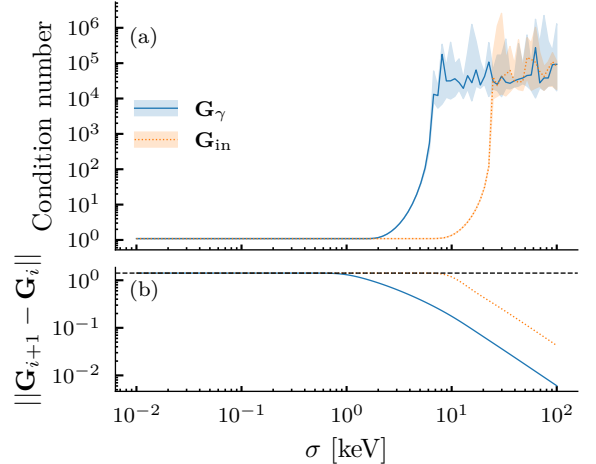

FIG. 5: (a) Condition number and (b) mean row distance of Gaussian smoothing matrix $\mathbf{G}$ versus resolution parameter σ, with fixed bin width $\Delta E = 10\,\text{keV}$. The dashed line in the bottom panel marks $\sqrt{2}$. The shaded bands represent the range of condition numbers across 100 instances with small perturbations, simulating numerical fluctuations in matrix construction. The transition from constant to linear distance scaling occurs when $\sigma \approx \Delta E$, coinciding with rapid growth in condition number. For $\mathbf{G}_\gamma$, the $\sigma_\gamma(E_\gamma)$ is calibrated so that the mean σ_γ over E_γ equals σ.

IV. MITIGATING ILL-POSEDNESS

Here we derive algebraic limitations of gamma-spectrum unfolding and outline how to construct workable solutions. We begin by showing why the system's ill-posedness cannot be resolved by using sharper Gaussian matrices. Accepting the experimental resolution, we map the unfolding problem to a smoothed space, which lifts much of the solution degeneracy. We then introduce a reparameterization that enforces nonnegativity and removes part of the degeneracy caused by the null space. Finally, we identify the remaining sources of variation and explain how regularization and uncertainty quantification fit into the overall workflow.

A. Algebraic limitations of generalized transformations

Having established that the structure of the double-sided matrix equation Eq. (54),

$$\boldsymbol{\nu} = \mathbf{G}_\gamma \mathbf{D} \boldsymbol{\mu} \mathbf{G}_{\text{in}}, \tag{64}$$

leads to a highly ill-posed problem due to the numerical properties of the involved matrices, we now turn to strategies for mitigating this ill-posedness. In particular,
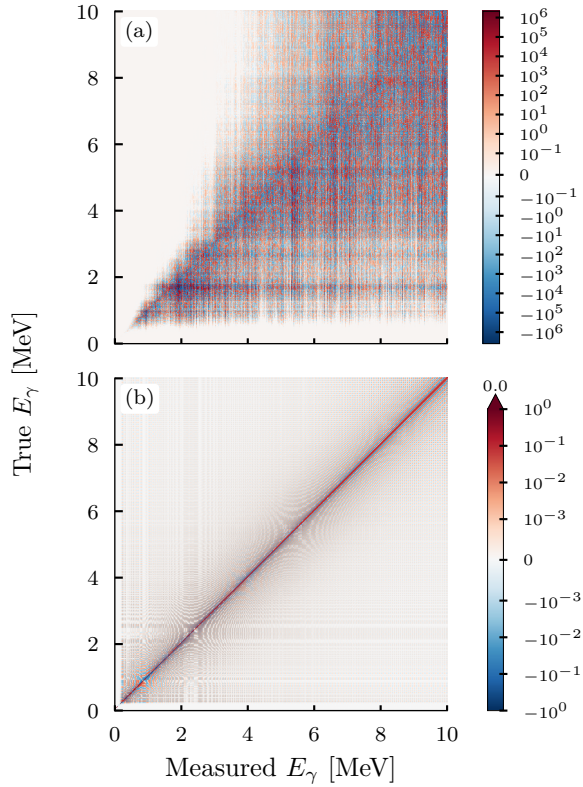
FIG. 6: (a) The product $\mathbf{G}_\gamma \mathbf{G}_\gamma^{-1}$. (b) The product $\mathbf{G}_\gamma \mathbf{G}_\gamma^\dagger$, where $\mathbf{G}_\gamma^\dagger$ is the Moore-Penrose pseudoinverse of $\mathbf{G}_\gamma$. The latter product is six orders of magnitude closer the identity than the former. The colors are linear between $\pm 10^{-1}$ and $\pm 10^{-3}$ for the top and bottom plot, respectively.

we consider a transformation that later will prove instrumental in addressing the limitations of more explicit constraint- and regularization-based approaches.

As shown in Fig. 3, the matrices $\mathbf{G}_\gamma$ and $\mathbf{G}_{\mathrm{in}}$ are the primary contributors to the high condition number of the system and thus the main drivers of degeneracy in the solution space. In contrast, the smearing introduced by the discrete matrix $\mathbf{D}$ is far more pronounced than that of $\mathbf{G}_\gamma$ and $\mathbf{G}_{\mathrm{in}}$. This observation suggests a tradeoff: if one is willing to accept the Gaussian smearing imposed by $\mathbf{G}_\gamma$ and $\mathbf{G}_{\mathrm{in}}$, it is possible to reduce the ill-posedness of the inversion. Accordingly, rather than unfolding directly to the sharply peaked spectrum $\boldsymbol{\mu} \in \mathcal{M}$, we instead unfold to a smoothed representation $\boldsymbol{\eta} \in \mathcal{H}$, where

$$\boldsymbol{\eta} = \mathbf{G}_\gamma \boldsymbol{\mu} \mathbf{G}_{\mathrm{in}} . \qquad (65)$$

The relations are illustrated in the diagram in Fig. 7. We denote by $\mathbf{R}_\sigma$ the map from $\mathcal{H}$ to $\mathcal{N}$, if such a map exists.

Before proceeding, one might question whether the specific choice of $\mathbf{G}_\gamma$ and $\mathbf{G}_{\mathrm{in}}$, corresponding to the experimental resolution, is overly restrictive. In practice, some approaches advocate using sharper Gaussian ker-
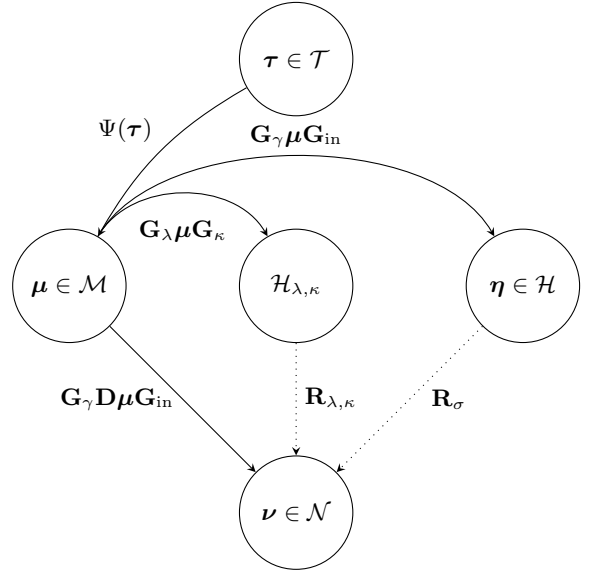

FIG. 7: The relation between the optimization space $\mathcal{T}$, the peaked space $\mathcal{M}$, the smoothed space $\mathcal{H}$, the folded space $\mathcal{N}$, and the intermediate "sharper" space $\mathcal{H}_{\lambda,\kappa}$. Each arrow represents a map from one space to another in the direction of the arrow. The dashed arrows for $\mathbf{R}_{\lambda,\kappa}$ and $\mathbf{R}_\sigma$ indicate that these maps are only well defined in special cases.

nels to recover more detailed spectral features.[24]

To examine the validity of this idea, we temporarily generalize the transformation $\mathcal{M} \to \mathcal{H}$ in Fig. 7 by introducing Gaussian smearing matrices $\mathbf{G}_\lambda$ and $\mathbf{G}_\kappa$. These matrices have Gaussian width parameters λ and κ, respectively, and play the roles of $\mathbf{G}_\gamma$ and $\mathbf{G}_{\mathrm{in}}$ *only* in the mapping from $\mathcal{M}$ to a new image space $\mathcal{H}_{\lambda,\kappa}$. This construction allows us to test whether alternative smoothing scales is possible. The analysis that follows shows that the structure of the problem ultimately forces a return to the original choice $\mathbf{G}_\lambda = \mathbf{G}_\gamma$ and $\mathbf{G}_\kappa = \mathbf{G}_{\mathrm{in}}$.

The mapping from $\mathcal{H}_{\lambda,\kappa}$ to the observable space $\mathcal{N}$ is denoted by $\mathbf{R}_{\lambda,\kappa}$. One might imagine unfolding to $\mathcal{H}_{\lambda,\kappa}$ via $\mathbf{R}_{\lambda,\kappa}$ instead of using the full operators $\mathbf{G}_\gamma \mathbf{D}$ and $\mathbf{G}_{\mathrm{in}}$. Yet the diagram imposes strict algebraic constraints, which turn out to preclude the existence of a well-defined $\mathbf{R}_{\lambda,\kappa}$.

To obtain an expression for $\mathbf{R}_{\lambda,\kappa}$, we require the diagram Fig. 7 to commute, i.e. the path $\mathcal{M} \to \mathcal{H}_{\lambda,\kappa} \to \mathcal{N}$

---

[24] See, e.g., Ref. [14] which appears to be the earliest work proposing this approach in the context of gamma-spectrum unfolding. Although the method is not presented in formal terms, it effectively corresponds to using Gaussian kernels narrower than the experimental resolution. Specifically, the authors advocate unfolding with artificially increased resolution and propose a heuristic rule for doing so, albeit without a theoretical justification. As demonstrated here, no universal rule of this kind can exist in general, though the underlying intuition is noteworthy.

must equal the direct path $\mathcal{M} \rightarrow \mathcal{N}$:

$$\overbrace{\mathbf{R}_{\lambda,\kappa}\,\mathbf{G}_\lambda \boldsymbol{\mu}\mathbf{G}_\kappa}^{\mathcal{M} \rightarrow \mathcal{H}_{\lambda,\kappa} \rightarrow \mathcal{N}} = \overbrace{\mathbf{G}_\gamma\,\mathbf{D}\boldsymbol{\mu}\mathbf{G}_{\mathrm{in}}}^{\mathcal{M} \rightarrow \mathcal{N}} \tag{66a}$$

$$\mathbf{R}_{\lambda,\kappa}\,\mathbf{G}_\lambda \boldsymbol{\mu}\mathbf{G}_\kappa\mathbf{G}_\kappa^{-1} = \mathbf{G}_\gamma\,\mathbf{D}\boldsymbol{\mu}\mathbf{G}_{\mathrm{in}}\mathbf{G}_\kappa^{-1} \tag{66b}$$

$$\mathbf{R}_{\lambda,\kappa}\,\mathbf{G}_\lambda \boldsymbol{\mu} = \mathbf{G}_\gamma\,\mathbf{D}\boldsymbol{\mu}\mathbf{G}_{\mathrm{in}}\mathbf{G}_\kappa^{-1}. \tag{66c}$$

To obtain a bounded operator $\mathbf{R}_{\lambda,\kappa}$ that is independent of $\boldsymbol{\mu}$, the right-hand factor must cancel, requiring $\mathbf{G}_{\mathrm{in}}\mathbf{G}_\kappa^{-1} = \mathbf{1}$ and thus forcing $\mathbf{G}_\kappa = \mathbf{G}_{\mathrm{in}}$. Although we write $\mathbf{G}_\kappa^{-1}$ and use $\mathbf{G}_\kappa\mathbf{G}_\kappa^{-1} = \mathbf{1}$ formally, this identity holds only in exact arithmetic; in practice, the Gaussian matrices are too ill-conditioned to be inverted.

Because Eq. (66) holds for all $\boldsymbol{\mu} \in \mathcal{M}$, we focus solely on the operators. Multiplying by $\mathbf{G}_\lambda^{-1}$ on the right yields

$$\mathbf{R}_{\lambda,\kappa} = \mathbf{G}_\gamma\mathbf{D}\mathbf{G}_\lambda^{-1} = \mathbf{D}\mathbf{G}_\gamma\mathbf{G}_\lambda^{-1} - \left[\mathbf{D}, \mathbf{G}_\gamma\right]\mathbf{G}_\lambda^{-1}. \tag{67}$$

Here the commutator $[\mathbf{D}, \mathbf{G}_\gamma]$ is taken in the matrix algebra acting on the gamma-energy bins. Since both operators are $n \times n$ matrices in the same space, the bracket is well-defined and quantifies their failure to commute.

There are essentially two limiting regimes to consider. Although an intermediate range exists in which λ is non-negligible yet still too small to drive the condition number of $\mathbf{G}_\lambda$ to extreme values, this window is practically irrelevant because the condition number of $\mathbf{G}_\lambda$ already exceeds 10^5 before the resolution reaches $\sigma = 10\,\mathrm{keV}$ (well below the typical OSCAR resolution), so its behavior is indistinguishable from the near-identity case.

In the limit $\lambda \to 0$, $\mathbf{G}_\lambda$ approaches the identity, and $\mathcal{H}_{\lambda,\kappa}$ collapses to the trivial space $\mathcal{M}$. As λ increases, the condition number of $\mathbf{G}_\lambda$ grows rapidly (see Fig. 5), making $\mathbf{R}_{\lambda,\kappa}$ increasingly ill-defined. For $\mathbf{R}_{\lambda,\kappa}$ to remain well defined, every term must stay bounded. A necessary, though not sufficient, requirement is that the product $\mathbf{G}_\gamma\mathbf{G}_\lambda^{-1}$ in the first term equals the identity, which forces $\mathbf{G}_\lambda = \mathbf{G}_\gamma$.

With both $\mathbf{G}_\kappa = \mathbf{G}_{\mathrm{in}}$ and $\mathbf{G}_\lambda = \mathbf{G}_\gamma$, the space $\mathcal{H}_{\lambda,\kappa}$ coincides with $\mathcal{H}$, and the map $\mathbf{R}_{\lambda,\kappa}$ reduces to

$$\mathbf{R}_\sigma = \mathbf{D} - \left[\mathbf{D}, \mathbf{G}_\gamma\right]\mathbf{G}_\gamma^{-1}. \tag{68}$$

Whether $\mathbf{R}_\sigma$ is well defined depends on the second term. The previous section showed that neither $\mathbf{D}$ nor $\mathbf{G}_\gamma$ has a structure that allows them to commute, and numerical tests confirm this result, see Fig. 8. The dominant feature of the commutator is a vertical peak at $511\,\mathrm{keV}$, which arises from the annihilation peak's energy-independent position. All other features are oscillations that are several orders of magnitude smaller.

The nonzero commutator $[\mathbf{D}, \mathbf{G}_\gamma]$ shows that smearing and Gaussian smearing are order dependent, so this residue cannot be removed by any redefinition of $\mathbf{R}_\sigma$. Moreover, the inverse $\mathbf{G}_\gamma^{-1}$ rarely exists in practice because its condition number is extremely large. Consequently, $\mathbf{R}_\sigma$ cannot be well defined in practical computations.
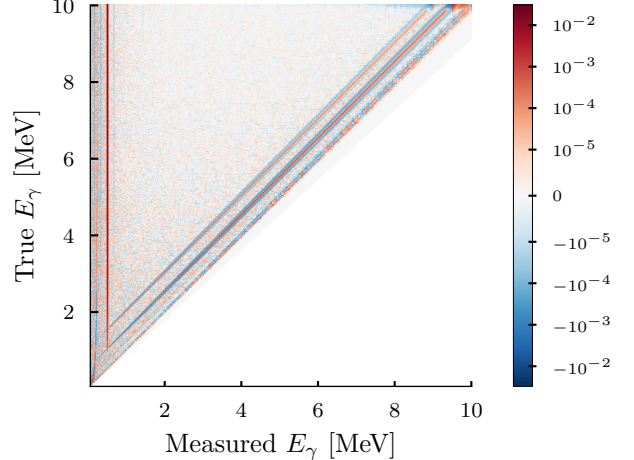

FIG. 8: The commutator $[\mathbf{D}, \mathbf{G}_\gamma]$. The largest feature is the vertical peak at $511\,\mathrm{keV}$ caused by the annihilation peak. Other discrete structures also fail to commute but are several orders of magnitude weaker. The Compton background's contribution is indistinguishable from numerical noise, except for its low-energy peak.

The identifications $\mathbf{G}_\lambda = \mathbf{G}_\gamma$ and $\mathbf{G}_\kappa = \mathbf{G}_{\mathrm{in}}$ are also motivated by practical considerations. Using a resolution sharper than the experimental resolution leaves residual degeneracy in the solution space that must otherwise be removed, a near impossible task in practice.

While methods such as those in Refs. [1, 14] do not explicitly define a mapping of the form $\mathbf{R}_{\lambda,\kappa}$, the operational structure of their algorithms suggests that such a transformation is assumed. Our derivation shows that this assumption leads to unavoidable structural error. Fortunately, a direct unfolding via $\mathbf{R}_{\lambda,\kappa}$ is unnecessary due to a transformation trick, which we now describe.

B. Constructing physically constrained solutions

The previous analysis established that unfolding directly to the smoothed space $\mathcal{H}$ is only rarely well defined. Rather than unfolding to $\mathcal{H}$ explicitly via the ill-defined map $\mathbf{R}_\sigma$, we instead formulate the optimization in the degenerate space $\mathcal{M}$ and recover physically meaningful quantities through the mapping to $\mathcal{H}$, lifting the degeneracy.

To enforce non-negativity, the optimizer operates in an unrestricted space $\mathcal{T} \subseteq \mathbb{R}^{N \times M}$, producing a candidate solution $\hat{\boldsymbol{\tau}} \in \mathcal{T}$. This candidate is mapped to $\mathcal{M} \subseteq \mathbb{R}_+^{N \times M}$ by a reparameterization Ψ (discussed in the next subsection), and then to $\mathcal{H}$ and $\mathcal{N}$ through the known operators. Specifically, we construct $\hat{\boldsymbol{\eta}} = \mathbf{G}_\gamma\Psi(\hat{\boldsymbol{\tau}})\mathbf{G}_{\mathrm{in}}$ and $\hat{\boldsymbol{\nu}} = \mathbf{G}_\gamma\mathbf{D}\Psi(\hat{\boldsymbol{\tau}})\mathbf{G}_{\mathrm{in}}$. The comparison to data is performed in $\mathcal{N}$, while regularization terms can be applied in either $\mathcal{M}$ or $\mathcal{H}$, depending on the nature of the constraint.

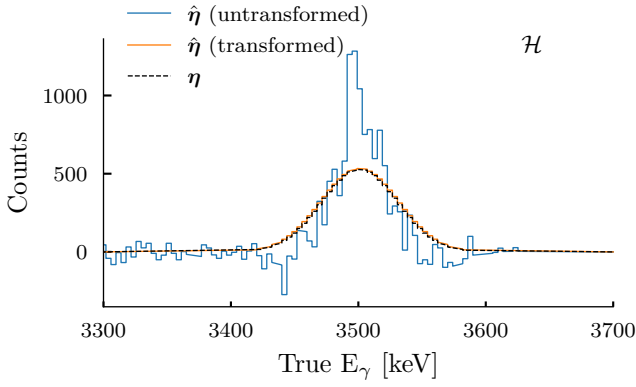This setup allows us to construct spectra in $\mathcal{H}$ through

FIG. 9: Unfolding without using the transformation nor reparameterization yields an $\hat{\boldsymbol{\eta}}$ that lacks the correct bin-to-bin correlations and non-negativity constraints. By contrast, unfolding with the transformations produces a solution that correctly preserves the expected correlations. The label $\mathcal{H}$ is included to clarify that the vectors shown reside in the space $\mathcal{H}$. The $\hat{\boldsymbol{\eta}}$s were found by RMLE as described in Sec. V.

a mathematically justified transformation, rather than attempting to solve the inverse problem directly in that space. Importantly, the expected correlations between bins in $\hat{\boldsymbol{\eta}}$—which are difficult to enforce through regularization alone—are inherently preserved by the transformation. An example is shown in Fig. 9.

Obtaining $\hat{\boldsymbol{\nu}}$ from $\hat{\boldsymbol{\eta}}$ is not possible, as the operator $\mathbf{R}_\sigma$ does not exist. In practice, however, this is rarely a limitation. Instead, the solution can be stored as either $\hat{\boldsymbol{\tau}}$ or $\hat{\boldsymbol{\mu}}$, from which $\hat{\boldsymbol{\eta}}$ and $\hat{\boldsymbol{\nu}}$ can be recovered through the known operators. It is important to note that neither $\hat{\boldsymbol{\tau}}$ nor $\hat{\boldsymbol{\mu}}$ has a direct physical interpretation due to the degeneracy of the inverse problem that we have accepted in the tradeoff.

A substantial benefit of this transformation is that it introduces global correlations across the spectrum, governed by the expected experimental resolution. The implications of this are examined in Sec. V B.

C. Null space degeneracy

Null vectors present a fundamental challenge by creating degeneracy in the solution space. The effective null space of $\mathbf{G}_\gamma$ is substantial: for a 2000×2000 matrix with a relative condition number[25] of 10^{-5}, the null space dimension exceeds 1500. Three examples of elements of the

---

[25] While the matrices are theoretically full rank, the null space issues of $\mathbf{G}$-like matrices are *numerical* in nature. The relative condition number ε determines which vectors are effectively treated as zero. Specifically, for the largest singular value $\sigma_{\max}$, any singular value less than $\varepsilon \cdot \sigma_{\max}$ is considered zero.
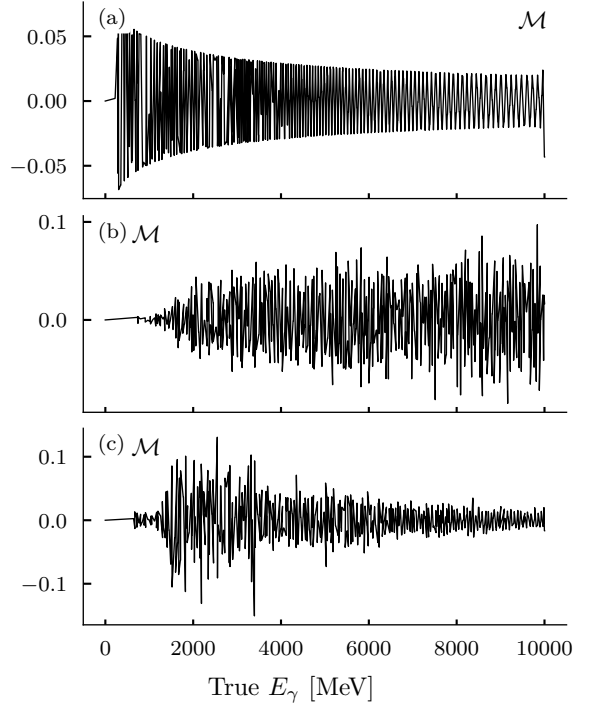

FIG. 10: Three null vectors of $\mathbf{G}_\gamma \mathbf{D}$, computed with a relative condition number $\varepsilon = 10^{-5}$. These vectors oscillate between negative and positive values, but fold to $\mathbf{0}$ in observable space $\mathcal{N}$.

null space are shown in Fig. 10. They are all oscillatory about zero, as expected by Theorem II.3.

A non-empty null space renders the unfolding problem *non-identifiable* (see Sec. II F). Given any data vector $\mathbf{Y}$, recovering the true $\boldsymbol{\mu}$ becomes impossible without additional constraints or information. This non-identifiability is illustrated in Figs. 11 to 13, which compare $\boldsymbol{\mu}$ solutions with and without null vector components. Despite substantial differences in the $\boldsymbol{\mu}$ vectors when null vectors are added, their folded counterparts in observable space remain identical. This demonstrates a critical limitation: optimizing or evaluating solutions solely in $\mathcal{N}$ will almost inevitably lead to unphysical solutions distorted by null vector components.

The degeneracy of the solution space can be partially addressed by exploiting the oscillatory nature of the null vectors. While enforcing non-negativity constraints does not completely exclude null vectors from the solution space (as long as solution components remain sufficiently close to zero), it can help regularize the problem. This is implemented by using a reparameterization to transform the solution space to be non-negative.

As the data follows a Poisson distribution, an exponential reparameterization $\Psi(\boldsymbol{\tau}) = \exp(\boldsymbol{\tau})$ is a natural choice, but it leads to optimization instability. Instead, we employ a quadratic reparameterization $\Psi(\boldsymbol{\tau}) = \boldsymbol{\tau}^2$, which provides better numerical stability. See Appendix A

FIG. 11: Comparison between a sharp peak $\boldsymbol{\mu}$ and $\boldsymbol{\mu} + \boldsymbol{v}_{\text{null}}$ for a $\boldsymbol{v}_{\text{null}}$(a), alongside their folded counterparts $\mathbf{G}_\gamma \mathbf{D} \boldsymbol{\mu}$ and $\mathbf{G}_\gamma \mathbf{D}(\boldsymbol{\mu} + \boldsymbol{v}_{\text{null}})$ (b). While the addition of $\boldsymbol{v}_{\text{null}}$ gives large oscillations in $\mathcal{M}$, the folded vectors are identical (up to a bin-difference $\propto 10^{-3}$), showing the issue caused by null-space vectors. The y-axis of the upper plot as been truncated.

FIG. 12: Similar comparison as Fig. 11 but for simulated ^{120}Sn, showing the impact of null-space vectors on a realistic spectrum. The identical folded spectra (b) demonstrate that the null-space degeneracy persists even in complex, physically-motivated cases. The y-axis in (a) has been truncated.

for more discussion on reparameterizations.

Optimizing over $\boldsymbol{\tau}$ allows the optimizer (see the next section for details on the optimizer) to traverse the parameter space without encountering hard boundaries that could cause convergence issues, or soft constraints that might permit small negative values. This transformation restricts the search space by eliminating unphysical negative components associated with null-space vectors. Although the exact reduction in search space dimensionality is difficult to quantify, this approach improves convergence in cases where unconstrained optimizations fail. However, as shown in Fig. 13, the presence of null vectors is not completely eliminated—a solution can remain strictly positive while still containing null vector components.

D. Sources of variation

In previous works on gamma-ray unfolding (e.g., [1, 14]) the term "fluctuations" has been used ambiguously to describe several distinct phenomena. This ambiguity has led to confusion in interpreting results and comparing methodologies. We propose a more precise terminology
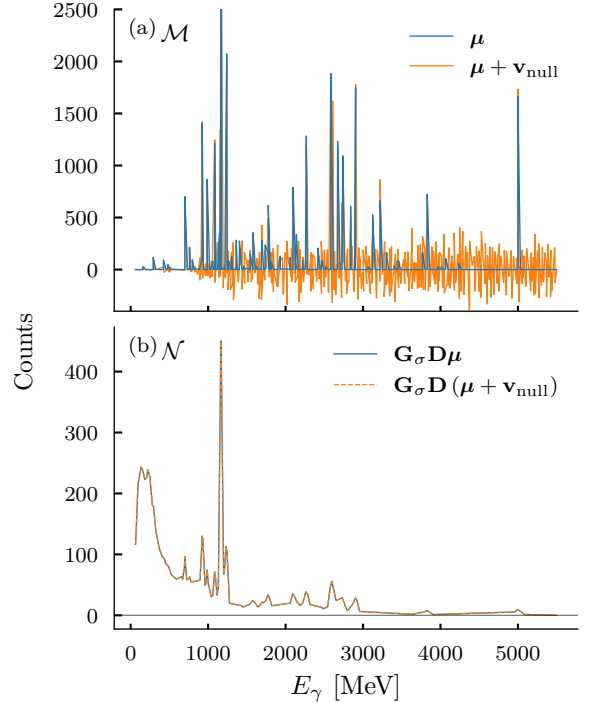
to distinguish between six sources of variation:

1. *Spectral complexity*, which is the intrinsic shape of $\boldsymbol{\mu}$.

2. *Stochastic variation*, arising from the Poisson nature of the prompt data $\mathbf{P} \sim \text{Poisson}(\boldsymbol{\nu} + \boldsymbol{\beta})$, where $\boldsymbol{\beta}$ is the background spectrum.

3. *Background error*, which captures the systematic bias introduced when using an observed background $\mathbf{B}_i$ in place of the true (unobservable) background $\mathbf{B}$. We discuss the background in Sec. V C.

4. *Model degeneracy*, which describes the fundamental non-uniqueness in solutions $\hat{\boldsymbol{\mu}}$ due to the non-empty null space of $\mathbf{R}$.

5. *Monte Carlo variance*, which appears when using Monte Carlo (MC) simulations to construct confidence intervals. The MC method is presented in Sec. VI.

6. *Variance in* $\mathbf{R}$. Model uncertainty in $\mathbf{R}$ will affect the solution space. This lies outside the scope of this work, but should be modeled.
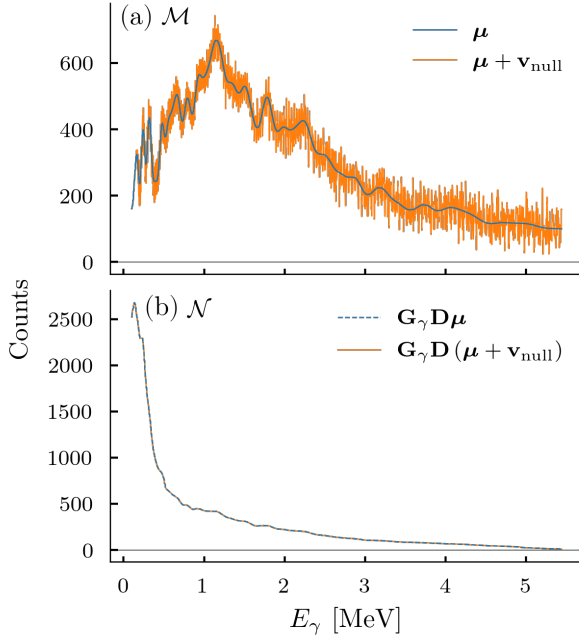
FIG. 13: Demonstration that null-space vectors can affect even strictly positive solutions. Despite both solutions being non-negative in (a), their difference is a null vector, resulting in identical folded spectra (b).
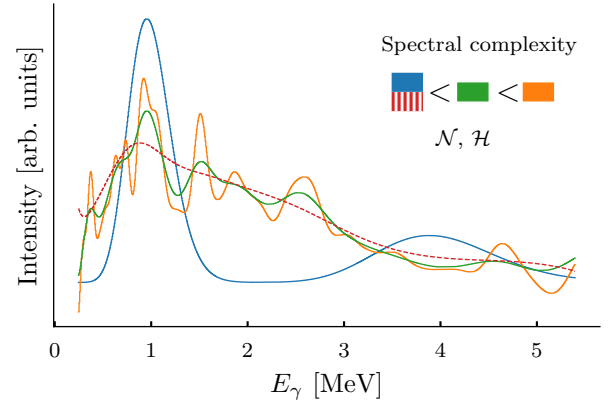

FIG. 14: Illustration of spectral complexity categories. The orange curve exemplifies a non-smooth spectrum characterized by non-isolated peaks with varying amplitudes. The blue curve represents a pseudo-smooth spectrum where sharper, isolated peaks are present within a generally smooth profile. The red curve demonstrates a smooth spectrum with low first and second derivatives, indicating a lack of sharp features. The green curve exhibits an intermediate level of complexity between the orange and red examples. Notably, all curves lack high-frequency bin-to-bin fluctuations, as their shape is determined by the underlying function space of $\boldsymbol{\eta}$.

Spectral complexity refers to variations intrinsic to the underlying signal structure – $\boldsymbol{\mu}$, $\boldsymbol{\eta}$, or $\boldsymbol{\nu}$ – distinct from stochastic noise introduced during measurement or data processing. This complexity can be quantified by analyzing the properties of $\boldsymbol{\eta} \in \mathcal{H}$, see Appendix B.

The spectral complexity is the most important feature when selecting a regularization procedure. We study this extensively in Sec. VII A–G. The fluctuations in the observed experimental data $\mathbf{Y}$ can be decomposed into two distinct components: spectral complexity, represented by variations in the true expected spectrum ($\boldsymbol{\nu} + \boldsymbol{\beta}$), and stochastic variation, arising from Poisson sampling noise:

$$\mathbf{Y} = \underbrace{(\boldsymbol{\nu} + \boldsymbol{\beta})}_{\text{Spectral complexity}} + \underbrace{(\mathbf{Y} - (\boldsymbol{\nu} + \boldsymbol{\beta}))}_{\text{Stochastic variation}} . \qquad (69)$$

Figures 14 and 15 illustrate the difference.

Without any prior model on $\boldsymbol{\nu} + \boldsymbol{\beta}$, these two components cannot be separated.[26] As a direct consequence, the bin-to-bin fluctuations give almost no information on how to regularize $\hat{\boldsymbol{\eta}}$. On the contrary, it is instead the *prior* assumptions of Poisson distribution and modeling of the background that allow for the separation of the spectral complexity and stochastic variation.

———

[26] In fact, *denoising* $\mathbf{Y}$ is an equally hard problem as unfolding to $\mathcal{H}$.

The estimated unfolded solution does not admit a simple additive variance decomposition. However, for illustrative purposes, we can approximate its variance as follows:

$$\text{Var}(\hat{\boldsymbol{\mu}}) \approx \underbrace{\text{Var}(\hat{\boldsymbol{\mu}}|\boldsymbol{\nu}, \boldsymbol{\beta})}_{\text{Stochastic variation}} + \underbrace{\text{Var}(\hat{\boldsymbol{\mu}}|\mathbf{B}_i \neq \mathbf{B})}_{\text{Background error}}$$
$$+ \underbrace{\text{Var}[\hat{\boldsymbol{\mu}}|\text{Ker}(\mathbf{G}_\gamma \mathbf{D} \mathbf{G}_{\text{in}})]}_{\text{Model degeneracy}} + \underbrace{\text{VarMC}}_{\text{MC variation}}. \qquad (70)$$

While these contributions are not statistically independent and may exhibit substantial covariance, we do not attempt to quantify those cross-terms here. This decomposition is meant to provide a rough indication of the dominant sources of variance. Similar decompositions apply to $\hat{\boldsymbol{\nu}}$ and $\hat{\boldsymbol{\eta}}$.

Notably, the spectral complexity does not appear explicitly in the decomposition of $\text{Var}(\hat{\boldsymbol{\mu}})$. This is because the spectral shape is intrinsic and unchanging for a given $\boldsymbol{\mu}$. When these sources of variation are properly accounted for, they influence the geometry of the solution space rather than any individual point within it. A specific point—such as $\hat{\boldsymbol{\eta}}$—will always reflect the spectral complexity corresponding to its location in the space. However, the collection of possible solutions inherits this complexity structure, which is implicitly shaped by the nature of the variations listed above.
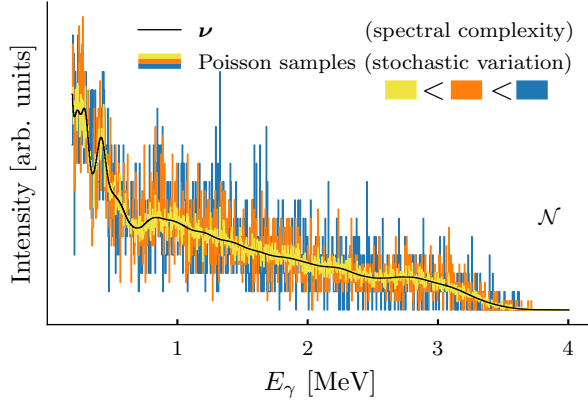
FIG. 15: The spectral complexity compared to three different stochastic variations. Stochastic variation is a property of the experiment, while the spectral complexity is independent of the experiment. The stochastic variations are Poisson samples of the same spectrum at different number of counts, normalized to be visually comparable.
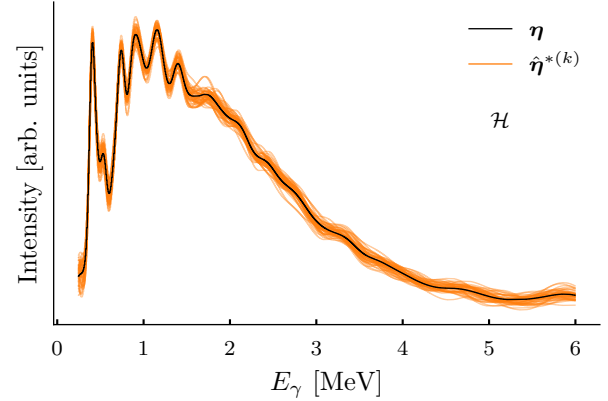

FIG. 16: Spectral complexity compared to $\mathrm{Var}(\hat{\boldsymbol{\eta}})$. Each Monte Carlo sample $\hat{\boldsymbol{\eta}}^{*(k)}$ represents a draw from the allowed solution space, with each sample exhibiting the same spectral complexity. The ensemble variance $\mathrm{Var}(\hat{\boldsymbol{\eta}})$ reflects the spread of these solutions. A properly constrained solution space should only permit spectral complexities consistent with that of the true solution.

In Fig. 16 the true $\boldsymbol{\eta}$ is shown together with an ensemble of MC $\hat{\boldsymbol{\eta}}^*$. While each ensemble member exhibits similar spectral complexity, the ensemble as a whole expresses the variance of the solution space. It is this ensemble-level spread—not the fluctuations of individual solutions—that reflects the full extent of uncertainty.

Unfolding methods that fail to account for these variations produce solutions that are explicitly affected by them. For instance, Richardson's iteration (see A 8) tends to overfit to statistical noise, causing stochastic variation to appear directly in the solution. Backgrounds subtracted naively allow the background error to propagate (see Eq. (34) and Sec. V C). Finally, the model degeneracy would not be accounted for, causing oscillatory features of the null space to appear, as illustrated in Figs. 11 to 13.

Among the variance components, the MC variation is the most straightforward to control, as it decreases with the number of samples. Both stochastic variation and background error scale with the Poisson uncertainty in each bin, roughly $\sqrt{Y_{ij}}$, which decreases as data counts increase. Regularization suppresses variance contributions from stochastic fluctuations, background mismodeling, and degeneracy, but at the cost of introducing bias. In the absence of regularization, stochastic variation and background error are greatly amplified by the condition number. Model degeneracy, in contrast, is unbounded, as demonstrated in Sec. II D, particularly by Eq. (34).

V. UNFOLDING METHOD

Notation Summary:

$\mathbf{G}_\gamma$	Smearing matrix along gamma-energy axis.
$\mathbf{G}_{\mathrm{in}}$	Smearing matrix along the initial-excitation-energy axis.
$\mathbf{D}$	Discrete response.
$\boldsymbol{\tau}$	Optimization variable
$\boldsymbol{\mu}$	The expectation value of the unfolded spectrum.
$\boldsymbol{\eta}$	The expectation value of the unfolded spectrum refolded by $\mathbf{G}_\gamma$ and $\mathbf{G}_{\mathrm{in}}$.
$\boldsymbol{\nu}$	The expectation value of the folded spectrum.
$\mathbf{Y}$	The observed data $\mathbf{Y} \sim \mathrm{Poisson}\left(\boldsymbol{\nu} = \mathbf{G}_\gamma \mathbf{D} \boldsymbol{\mu} \mathbf{G}_{\mathrm{in}}\right)$.
$\mathcal{M}, \mathcal{H}$ $\mathcal{N}, \mathcal{T}$	The spaces which $\boldsymbol{\mu}, \boldsymbol{\eta}, \boldsymbol{\nu}$ and $\boldsymbol{\tau}$ belong, respectively.
Ψ	Non-negativity constraint $\boldsymbol{\mu} = \Psi(\boldsymbol{\tau})$.

A. Regularized maximum likelihood estimation

Algorithm 1 Maximum Likelihood Unfolding with Regularization

Require:
    Observed data matrix $\mathbf{Y}$
    Discrete response matrix $\mathbf{D}$
    E_γ smoothing matrix $\mathbf{G}_\gamma$
    E_{in} smoothing matrix $\mathbf{G}_{\text{in}}$
    Regularization parameters $\boldsymbol{\theta}$
    Detector efficiency $\varepsilon(E_\gamma)$
Ensure:
    Optimized unfolded spectrum $\hat{\boldsymbol{\eta}}$
1: **Initialize**
    Find $\sigma_{\max}$ from $\text{SVD}(\mathbf{G}_\gamma \mathbf{D})$
    Set step size $d\tau < \frac{1}{2\sigma_{\max}^2}$
    Compute bound $\mu_{\max} = \frac{||Y||_1}{||\mathbf{G}_\gamma||_1 ||\mathbf{D}||_1 ||\mathbf{G}_{\text{in}}||_1}$
    Set initial guess $\tau_i \leftarrow \text{Uniform}(10^{-1}, \mu_{\max})$
    Compute initial $\hat{\boldsymbol{\mu}} \leftarrow \Psi(\boldsymbol{\tau})$
2: **while** not converged **do**
3:     **Fold**
        $\hat{\boldsymbol{\nu}} \leftarrow \mathbf{G}_\gamma \mathbf{D} \hat{\boldsymbol{\mu}} \mathbf{G}_{\text{in}}$
4:     **Compute Loss Function** $L(\hat{\boldsymbol{\mu}}, \mathbf{y}; \boldsymbol{\theta})$
        $L \leftarrow \sum_{ij} \nu_{ij} - Y_{ij} \log(\nu_{ij}) + \Omega(\hat{\boldsymbol{\mu}}; \boldsymbol{\theta})$
5:     **Calculate Gradients (JAX)**
        $\nabla_{\boldsymbol{\tau}} L$
6:     **Update Parameters (NAdam)**
        $\boldsymbol{\tau} \leftarrow \text{Optimizer}(\boldsymbol{\tau}, d\tau, \nabla_{\boldsymbol{\tau}} L)$
        $\hat{\boldsymbol{\mu}} \leftarrow \Psi(\boldsymbol{\tau})$
7:     **Check Convergence**
8:     **if** Change in L below threshold
9:      **or** maximum iterations reached **then**
10:       Break
11:     **end if**
12: **end while**
13: **Correct for detector efficiency**
    $\hat{\boldsymbol{\mu}} \leftarrow \hat{\boldsymbol{\mu}}/\boldsymbol{\varepsilon}$
14: **Return**
    $\hat{\boldsymbol{\mu}}$
    $\hat{\boldsymbol{\eta}} \leftarrow \mathbf{G}_\gamma \hat{\boldsymbol{\mu}} \mathbf{G}_{\text{in}}$

Having established the theoretical and practical challenges of the inverse problem, we now present the regularized maximum likelihood method for unfolding gamma-ray spectra. A summary of the unfolding method is given in Algorithm 1.

The unfolded spectrum is obtained by minimizing a loss function, $L(\hat{\boldsymbol{\mu}}, \mathbf{Y})$, which balances the fit to the data and expected physical characteristics of the solution using gradient descent. The loss consists of the Poisson log-likelihood, $\ell(\boldsymbol{\mu})$ (see Eq. (44)), along with an added penalty term, $\Omega(\hat{\boldsymbol{\mu}}; \boldsymbol{\theta})$, to enforce the physicality:

$$L(\hat{\boldsymbol{\mu}}, \mathbf{Y}; \boldsymbol{\theta}) = \ell(\hat{\boldsymbol{\mu}}|\mathbf{Y}) + \Omega(\hat{\boldsymbol{\mu}}; \boldsymbol{\theta}), \quad (71)$$

where

$$\ell(\hat{\boldsymbol{\mu}}|\mathbf{Y}) = \mathbf{G}_\gamma \mathbf{D} \hat{\boldsymbol{\mu}} \mathbf{G}_{\text{in}} - \mathbf{Y} \log(\mathbf{G}_\gamma \mathbf{D} \hat{\boldsymbol{\mu}} \mathbf{G}_{\text{in}}), \quad (72)$$

and $\boldsymbol{\theta}$ are the penalization parameters.[27] Some convergence requirements on the optimization step size are derived in Appendix C.

The choice of regularization strength should be guided by empirical expectations regarding the spectrum's structure. Discrete regions are expected to exhibit sharp peaks, continuous regions should show smooth transitions, and the quasi-continuum combines both smoothness and structure. At low initial excitation energies, the level density—and consequently the number of possible gamma transitions—is low, leading to high sparsity. In contrast, the continuum is characterized by a lack of sparsity, while the intermediate quasi-continuum presents a challenge, as its sparsity decreases with increasing initial excitation energy. To account for these variations in the spectrum, the strength of the regularization parameter can be adjusted based on initial excitation energy using simulated representative spectra.

The penalty term used for regularization should be chosen according to the characteristics of the spectrum. For a discrete spectrum, where sparsity is expected, a sparsity-promoting cost encourages fewer non-zero elements in the $\hat{\boldsymbol{\mu}}$-spectrum. Although an ℓ_1 penalty promotes sparsity, it can also attenuate important peaks. A smoother alternative that retains salient peaks while still favoring sparsity is a sigmoid-shaped penalty, for example, based on the arctangent,

$$\Omega(\hat{\boldsymbol{\mu}}; \boldsymbol{\theta}) = \theta_0 \sum_{ij} \frac{1}{2} \left(1 + \frac{2}{\pi} \arctan\left(\frac{\mu_{ij} - \theta_1}{\theta_1/\theta_2} \right) \right), \quad (73)$$

where θ_0 controls the overall regularization strength, θ_1 sets the lower threshold, and θ_2 determines the width of the sigmoid.

To promote smoothness in the estimated spectrum $\hat{\boldsymbol{\eta}}$, a generalized Sobolev penalty can be applied to penalize high-frequency variations. The regularization term is given by

$$\Omega(\hat{\mu}; \boldsymbol{\theta}) = \sum_{k=1}^{K} \theta_k \sum_{i,j} \left| \left(\nabla^k G_\gamma \hat{\mu} G_{\text{in}} \right)_{ij} \right|^2,$$

where ∇^k denotes the kth discrete derivative operator. This formulation allows for control over which frequency components are penalized, with higher k targeting increasingly rapid oscillations in $\hat{\boldsymbol{\eta}}$.

A complementary strategy is to minimize or maximize the *entropy*,

$$\Omega(\hat{\boldsymbol{\mu}}; \theta) = -\theta \sum_{ij} \left(G_\gamma \hat{\mu} G_{\text{in}} \log \left[G_\gamma \hat{\mu} G_{\text{in}} \right] \right)_{ij}, \quad (74)$$

---

[27] Both the likelihood and different forms of regularizations contain log and divisions by matrices. Both are susceptible to numerical instability, and must be stabilized by the addition of small numerical constants. These are not shown in the equations to avoid visual clutter.

where the sign of θ selects the desired behavior: minimizing the entropy $(\theta > 0)$ sharpens the distribution, effectively mimicking the sigmoid sparsity penalty, whereas maximizing it $(\theta < 0)$ encourages a broader, smoother spectrum similar to Sobolev regularization.

While it is in principle possible to combine penalty terms to accommodate spectra with both discrete and continuous features, selecting regularization strengths that yield consistently good results remains challenging in practice. For data of the type measured in Oslo experiments, this remains an open problem, as discussed in Sec. VII. A comment on how to select regularization method and regularization strength is given in Appendix G.

B. Effect of $\mathbf{G_{in}}$

Standard analyses of Oslo gamma-spectra have addressed $\mathbf{G_{in}}$ smearing separately from the main unfolding framework. This approach typically manages count sparsity through E_{in}-axis rebinning, increasing statistics per row at the cost of introducing discretization artifacts. While the effects of $\mathbf{G_{in}}$ may appear less pronounced than those of $\mathbf{G_\gamma D}$, excluding them from the unfolding process overlooks important aspects of the measurement structure.

The forward model $\boldsymbol{\nu} = \mathbf{G_\gamma D \boldsymbol{\mu} G_{in}}$ shows that $\mathbf{G_{in}}$ is an integral part of the spectrum formation. While $\mathbf{G_\gamma}$ induces smearing and correlations along the E_γ axis, $\mathbf{G_{in}}$ plays an equivalent role along the E_{in} axis. A complete inversion of this process must therefore account for both transformations.

Numerical tests show the advantages of this unified approach. In Fig. 17, we compare reconstructions with progressively more complete model specifications. Unfolding with $\mathbf{D}$ alone completely fails to recover the underlying structure due to the count sparsity. Including $\mathbf{G_\gamma D}$ begins to resolve the peaks but produces noisy results with poorly defined boundaries. The complete $\mathbf{G_\gamma D G_{in}}$ model achieves a more faithful reconstruction of $\boldsymbol{\eta}$, though still containing noise artifacts. Since the unfolding problem remains ill-posed, even this complete model cannot uniquely determine the true $\boldsymbol{\eta}$ without additional constraints. However, the addition of sparsity regularization proves sufficient for the recovery of $\boldsymbol{\eta}$. This unified treatment achieves full resolution without rebinning to increase statistics, and incurs negligible additional computational cost. Importantly, the incorporation of $\mathbf{G_\gamma}$ and $\mathbf{G_{in}}$ with the remapping to $\mathcal{H}$ (as described in Sec. IV B) allows the optimizer to exploit the correlations of neighboring bins while not being affected by their induced degeneracy.
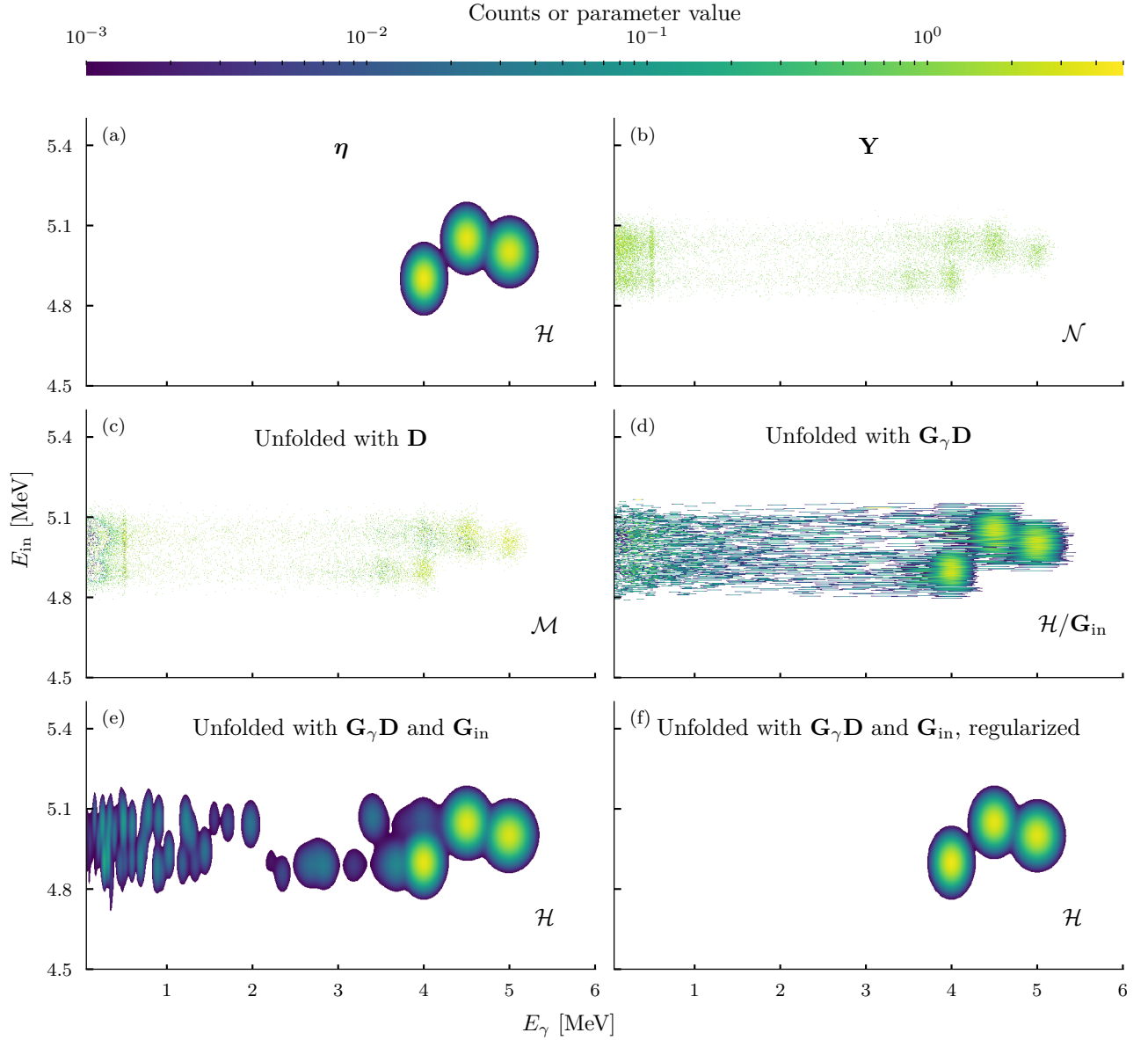
FIG. 17: Comparison of unfolding methods applied to a high-resolution 1000×1000 spectrum containing three sharp peaks, each with 10^4 counts. Panel (a) shows the true $\boldsymbol{\eta}$ spectrum, while panel (b) displays its Poisson-sampled observation $\mathbf{Y}$, illustrating the challenge posed by sparse data, particularly in the $4.8\,\mathrm{MeV}$ to $5.2\,\mathrm{MeV}$ region, which contains only 73 counts on average per E_{in} vector. The subsequent panels present unfolding results with progressively more prior information: (c) $\mathbf{D}$ alone (negligible improvement), (d) $\mathbf{G}_\gamma \mathbf{D}$ (partial improvement but dominated by noise), (e) $\mathbf{G}_\gamma \mathbf{D} \mathbf{G}_{\mathrm{in}}$ (sharper reconstruction but with spurious peaks), and (f) $\mathbf{G}_\gamma \mathbf{D} \mathbf{G}_{\mathrm{in}}$ with sparsity regularization (accurate recovery of the original $\boldsymbol{\eta}$). The incorporation of correlations from both $\mathbf{G}_\gamma$ and $\mathbf{G}_{\mathrm{in}}$, along with regularization, yields the most effective reconstruction under sparse conditions.

C. Background modeling

Experimental spectra always contain background signals that must be accounted for in the analysis. We model both the background and prompt spectra as independent Poisson processes with means $\boldsymbol{\beta}$ and $\boldsymbol{\pi}$, respectively:

$$\mathbf{B} \sim \text{Poisson}(\boldsymbol{\beta}) \tag{75}$$

$$\mathbf{P} \sim \text{Poisson}(\boldsymbol{\pi}). \tag{76}$$

A naive approach to extract the data spectrum would be to subtract the background spectrum $\mathbf{B}$ from the prompt spectrum $\mathbf{P}$, yielding $\tilde{\mathbf{Y}} = \mathbf{P} - \mathbf{B}$. However, in addition to the problems shown in Sec. II D, this difference $\tilde{\mathbf{Y}}$ does not follow a Poisson distribution. While the sum of two Poisson-distributed variables yields another Poisson distribution with mean $\boldsymbol{\beta} + \boldsymbol{\pi}$, their difference follows a *Skellam* distribution:

$$\mathbf{P} - \mathbf{B} \sim \text{Skellam}(\boldsymbol{\pi}, \boldsymbol{\beta}). \tag{77}$$

The Skellam distribution poses computational challenges. Its likelihood evaluation is computationally demanding, and relaxing the non-negativity constraints on $\mathbf{Y}$, $\boldsymbol{\eta}$, and related variables introduces additional degeneracy that destabilizes the optimization. To avoid these challenges, we model $\mathbf{Y}$ as a latent, unobserved variable:

$$\mathbf{Y} \sim \text{Poisson}(\boldsymbol{\nu}) \tag{78}$$

$$\mathbf{P} = \mathbf{Y} + \mathbf{B}, \quad \mathbf{P} \sim \text{Poisson}(\boldsymbol{\nu} + \boldsymbol{\beta}). \tag{79}$$

The likelihoods of all parameters are now Poisson and easy to handle.

An additional complexity arises because, while $\mathbf{P}$ is directly observable, the actual background $\mathbf{B}$ of $\mathbf{P}$ is not. However, we can observe N non-prompt peaks, which can be modeled as independent samples from the same background distribution parameterized by $\boldsymbol{\beta}$:

$$\mathbf{B}_i \sim \text{Poisson}(\boldsymbol{\beta}) \quad \text{for } i = 1, \ldots, N. \tag{80}$$

To unfold with this model, we jointly optimize the log-likelihood of $\boldsymbol{\nu}$ and $\boldsymbol{\beta}$, combining their contributions along with appropriate regularization terms:

$$L(\hat{\boldsymbol{\mu}}, \hat{\boldsymbol{\beta}}, \mathbf{P}, \mathbf{B}_i; \boldsymbol{\theta}_\mu, \boldsymbol{\theta}_\beta) = \ell\left(\hat{\boldsymbol{\mu}} \mid \mathbf{P}\right) + \sum_i^N \ell\left(\hat{\boldsymbol{\beta}} \mid \mathbf{B}_i\right)$$
$$+ \Omega_\mu\left(\hat{\boldsymbol{\mu}}; \boldsymbol{\theta}_\mu\right) + \Omega_\beta\left(\hat{\boldsymbol{\beta}}; \boldsymbol{\theta}_\beta\right), \tag{81}$$

where

$$\ell\left(\hat{\boldsymbol{\mu}} \mid \mathbf{P}\right) = \mathbf{G}_\gamma \mathbf{D} \hat{\boldsymbol{\mu}} \mathbf{G}_{\text{in}} + \hat{\boldsymbol{\beta}}$$
$$- \mathbf{P} \log\left(\mathbf{G}_\gamma \mathbf{D} \hat{\boldsymbol{\mu}} \mathbf{G}_{\text{in}} + \hat{\boldsymbol{\beta}}\right), \tag{82}$$

and

$$\ell\left(\hat{\boldsymbol{\beta}} \mid \mathbf{B}_i\right) = \hat{\boldsymbol{\beta}} - \mathbf{B}_i \log\left(\hat{\boldsymbol{\beta}}\right), \tag{83}$$

represent the log-likelihood terms for the prompt and background spectra, respectively.

While the background parameter $\hat{\boldsymbol{\beta}}$ can be regularized through a penalty term $\Omega_\beta\left(\hat{\boldsymbol{\beta}}; \boldsymbol{\theta}_\beta\right)$, analogous to the signal, this approach faces similar challenges, particularly in selecting an appropriate regularization model. The background consists of several distinct physical processes, which makes it difficult to construct a meaningful prior. In practice, a Sobolev regularization with order $k \geq 5$ is recommended to suppress spurious bin-to-bin fluctuations in the absence of more specific structural assumptions.

We demonstrate the combined unfolding approach with background in Figs. 18 and 19 using synthetic ^{120}Sn-like spectrum at $E_{\text{in}} = 8\,\text{MeV}$, with uncertainty quantification as explained later in Sec. VI. The 95% confidence intervals largely encompass the true expectations $\boldsymbol{\eta}$ and $\boldsymbol{\beta}$ for both the signal and the background. Notably, the method successfully recovers and separates signal and background components even in regions where the signal-to-noise ratio is low. This capability stems from the signal's smeared distribution across the entire spectrum, allowing information from regions with better signal-to-noise ratios to inform the recovery in the noisier regions. The increased uncertainty in these regions is reflected in wider confidence intervals consistent with 0.

D. Contaminant modeling

Gamma spectra from Oslo-type experiments often contain contaminant peaks from unwanted background sources. Typical contaminants are transitions from ^{16}O and ^{12}C. Contaminants may have different response functions from the main spectrum due to Doppler broadening. While standard unfolding methods have difficulties in handling contaminants, the flexibility of RMLE handles them effectively.

Unlike a background spectrum, which can be measured separately, contaminants overlap with the prompt signal, making temporal separation impossible. An arbitrary contamination is practically impossible to separate from the signal unless it can be accurately modeled. Fortunately, many contaminants in Oslo-type spectra are characterized by their simplicity — typically just a handful of well-identified transitions. This characteristic allows us to place strong constraints on both their peak locations and intensities during the unfolding process. By incorporating these constraints into the RMLE optimization, we can effectively separate the contaminant contributions from the prompt spectrum.

For M well-identified contaminant peaks $\{\boldsymbol{\xi}_i\}_{i=1}^M$, we can construct individual response functions $\{\mathbf{G}_{\gamma,i} \mathbf{D}_i \mathbf{G}_{\text{in},i}\}_{i=1}^M$ for each contaminant component $\boldsymbol{\xi}_i$. The observed spectrum $\mathbf{Y}$ can then be modeled as a sum of the main spectrum and these contaminant contributions (for notational simplicity we ignore the
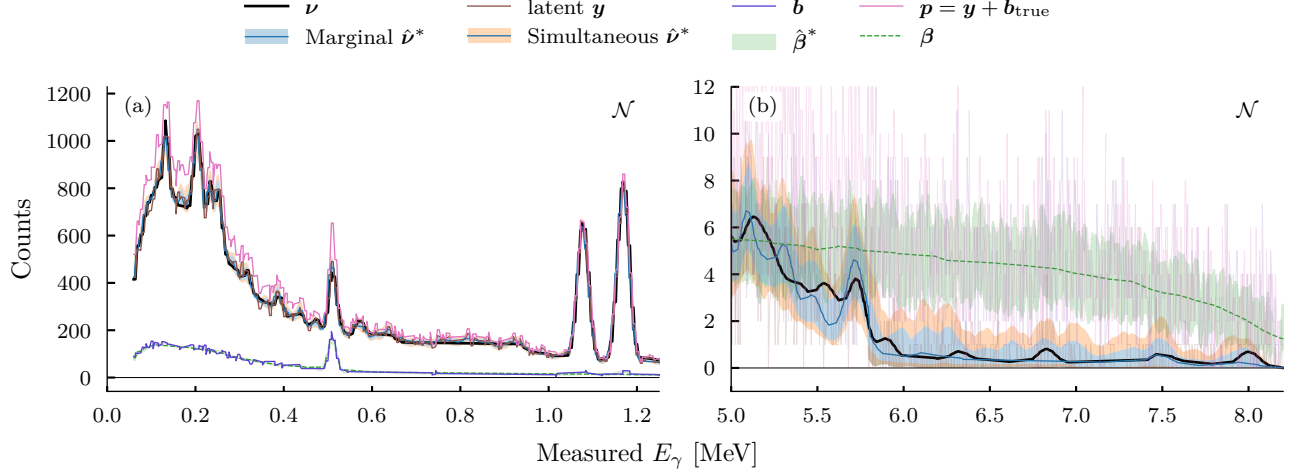
FIG. 18: Demonstration of background unfolding in the $\mathcal{N}$ space. The observed prompt spectrum $\boldsymbol{p}$ represents the sum of two unobserved components: the signal spectrum $\boldsymbol{y} \sim \mathrm{Poisson}\,(\boldsymbol{\nu})$ and the background spectrum $\boldsymbol{b} \sim \mathrm{Poisson}\,(\boldsymbol{\beta})$, with their relative contributions varying across the energy range. The left panel (a) shows the low-energy region where signal dominates, while the right panel (b) shows the high-energy region where background becomes dominant. The 95% confidence intervals around $\hat{\boldsymbol{\nu}}$ successfully contain the true $\boldsymbol{\nu}$ across the entire spectrum, demonstrating robust recovery even in regions of low signal-to-noise ratio.
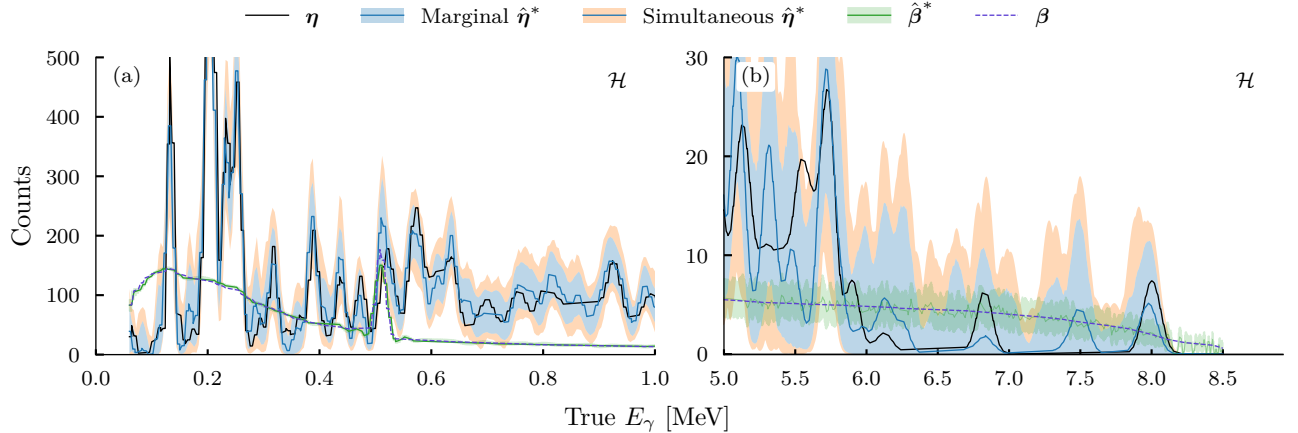

FIG. 19: Results of background unfolding shown in the $\mathcal{H}$ space in a low-energy region (a) and a high-energy region (b). The 95% confidence intervals around both the unfolded spectrum $\hat{\boldsymbol{\eta}}$ and the background spectrum $\hat{\boldsymbol{\beta}}$ largely capture their true values ($\boldsymbol{\eta}$ and $\boldsymbol{\beta}$, respectively). The contrasting smoothness between signal and background highlights the impact of regularization: $\hat{\boldsymbol{\eta}}$ exhibits smooth behavior due to implicit regularization, while the unregularized $\hat{\boldsymbol{\beta}}$ shows greater spectral variation, resulting in wider and less smooth confidence intervals.

background model of Sec. V C, but they are easily combined additively):

$$\mathbf{Y} \sim \mathrm{Poisson}\left(\mathbf{G}_\gamma \mathbf{D} \boldsymbol{\mu} \mathbf{G}_{\mathrm{in}} + \sum_{i=1}^{M} \mathbf{G}_{\gamma,i} \mathbf{D}_i \boldsymbol{\xi}_i \mathbf{G}_{\mathrm{in},i}\right). \quad (84)$$

The unfolding is performed by optimizing the log-likelihood with appropriate regularization terms:

$$L\left(\hat{\boldsymbol{\mu}}, \hat{\boldsymbol{\xi}}_i, \mathbf{Y}; \boldsymbol{\theta}, \boldsymbol{\theta}_{\xi,i}\right) = \ell\left(\hat{\boldsymbol{\mu}}, \left\{\hat{\boldsymbol{\xi}}_i\right\}_{i=1}^{M} \Big| \mathbf{Y}\right)$$
$$+ \Omega\left(\hat{\boldsymbol{\mu}}, \left\{\hat{\boldsymbol{\xi}}_i\right\}_{i=0}^{M}; \boldsymbol{\theta}, \boldsymbol{\theta}_{\xi,i}\right) \quad (85\mathrm{a})$$
$$= \hat{\boldsymbol{\nu}} + \hat{\boldsymbol{\xi}}_\nu - \mathbf{Y} \log\left(\hat{\boldsymbol{\nu}} + \hat{\boldsymbol{\xi}}_\nu\right)$$
$$+ \Omega_\mu(\hat{\boldsymbol{\mu}}; \boldsymbol{\theta}_\mu) + \sum_{i=1}^{M} \Omega_i(\hat{\boldsymbol{\xi}}_i; \boldsymbol{\theta}_{\xi,i}), \quad (85\mathrm{b})$$

with response terms

$$\hat{\boldsymbol{\nu}} = \mathbf{G}_\gamma \mathbf{D} \hat{\boldsymbol{\mu}} \mathbf{G}_{\text{in}} \tag{86}$$

$$\hat{\boldsymbol{\xi}}_\nu = \sum_{i=1}^{M} \mathbf{G}_{\gamma,i} \mathbf{D}_i \hat{\boldsymbol{\xi}}_i \mathbf{G}_{\text{in},i}. \tag{87}$$

The regularization terms $\left\{ \Omega_i(\hat{\boldsymbol{\xi}}_i; \boldsymbol{\theta}_{\xi,i}) \right\}_{i=0}^{M}$ enforce sparsity and other user-specified constraints on the contaminant components, constraining their contributions to the known peak regions.

To illustrate the method, a simulated ^{166}Ho-like spectrum at $E_{\text{in}} = 4\,\text{MeV}$ was contaminated with a single peak at $3\,\text{MeV}$ and unfolded (see Fig. 20. The uncertainty bands are explained later in Sec. VI). A prior Gaussian fit of the contaminant peak provided initial estimates and constraints for the central value, standard deviation and ν-amplitude. These constraints alone resulted in overfitting by the unfolding algorithm, producing a spurious peak in $\hat{\boldsymbol{\eta}}$. To address this, a weighted Tikhonov regularization was applied between $2.6\,\text{MeV}$ and $3.4\,\text{MeV}$ to penalize excessive counts in this region. The penalization weight was determined through trial and error, balancing the avoidance of dips in the unfolded spectrum ($\hat{\boldsymbol{\eta}}$) with the suppression of excessive counts.

This underscores a fundamental limitation: the necessity for strong, user-defined constraints on the contaminant model, which introduces the potential for bias through overly strict or lenient specifications. Lacking a model that sufficiently constrains the solution space, it is best to construct a model that allows for the most variance in order to reduce the bias.

The RMLE method provides a stable and physically constrained point estimate of the unfolded spectrum. However, to enable statistically sound interpretation of the results, uncertainty quantification is necessary. In the next section, we describe how to construct calibrated confidence intervals for each bin of the unfolded spectrum through Monte Carlo resampling.
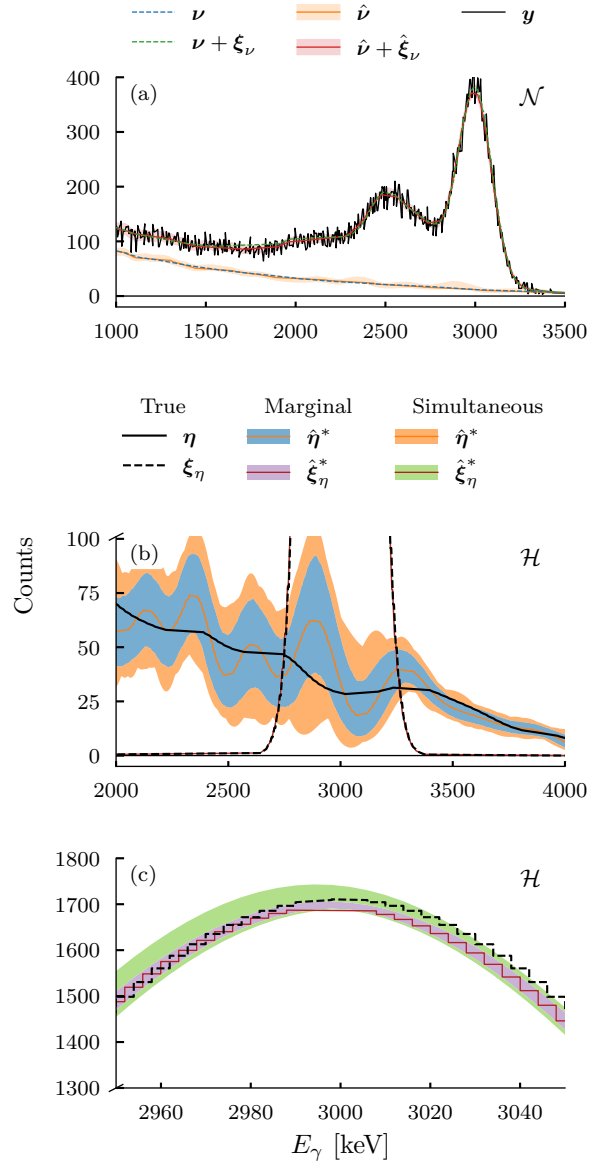

FIG. 20: Unfolding of a simulated ^{166}Ho-like spectrum with a dominant contaminant peak at $3\,\text{MeV}$. With sufficient model constraints on both the peak and the overlap region, the signal and contaminant can be effectively separated. (a) The raw spectrum $\mathbf{y}$, a Poisson sample of the combined signal $\boldsymbol{\nu}$ and contaminant $\boldsymbol{\xi}$. The refolded solutions accurately recover both $\boldsymbol{\nu}$ and $\boldsymbol{\nu} + \boldsymbol{\xi}$. The uncertainty bands are marginal. (b) Zoomed-in comparison of the true spectrum $\boldsymbol{\eta}$ and the unfolded Monte Carlo solution $\hat{\boldsymbol{\eta}}^*$. The confidence interval (CI) widens near the contaminant peak, fully encompassing $\boldsymbol{\eta}$. (c) Zoomed-in comparison of the true contaminant $\boldsymbol{\xi}$ and its unfolded estimate $\hat{\boldsymbol{\xi}}^*$. The CI here is much narrower than that of $\hat{\boldsymbol{\eta}}^*$ due to stronger constraints in the contaminant model.

VI. UNCERTAINTY QUANTIFICATION

A. Monte Carlo resampling

Algorithm 2 Constructing confidence intervals using Monte Carlo ensemble.

Require:
   Observed data $\mathbf{Y}$ or $\mathbf{P}$
   Observed background(s) $\mathbf{B}_i$
   Models for contaminants $\left\{\hat{\boldsymbol{\xi}}_{\mathrm{sol},i}\right\}_{i=1}^M$ ▷ If present
   Refolded solution $\hat{\boldsymbol{\nu}}_{\mathrm{sol}}$ ▷ Recommended
   Background parameter $\hat{\boldsymbol{\beta}}_{\mathrm{sol}}$
   Number of Monte Carlo samples N
Ensure:
   Confidence intervals for $\hat{\boldsymbol{\eta}}_{\mathrm{sol}}, \hat{\boldsymbol{\nu}}_{\mathrm{sol}}, \hat{\boldsymbol{\beta}}_{\mathrm{sol}}, \left\{\hat{\boldsymbol{\xi}}_{\mathrm{sol},i}\right\}_{i=1}^M$
1: `Generate Monte Carlo Ensemble`
2: **for** $k = 1$ to N **do**
3:    Sample new observation $Y_{ij}^{*(k)} \sim \mathrm{Poisson}(\lambda_{ij})$,
      where $\lambda_{ij} = (\hat{\nu}_{\mathrm{sol}})_{ij}$ or $\left(\hat{\nu}_{\mathrm{sol}} + \sum_{l=0}^M \hat{\xi}_{\mathrm{sol},l}\right)_{ij}$ or Y_{ij}
4:    Sample new observation $B_{ij}^{*(k)} \sim \mathrm{Poisson}(\kappa_{ij})$,
      where $\kappa_{ij} = \left(\hat{\beta}_{\mathrm{sol}}\right)_{ij}$ or B_{ij}
5:    Unfold $\mathbf{Y}^{*(k)}$ with $\mathbf{B}^{*(k)}$ to get $\hat{\boldsymbol{\eta}}^{*(k)}$, $\hat{\boldsymbol{\beta}}^{*(k)}$ and $\left\{\hat{\boldsymbol{\xi}}_i^{*(k)}\right\}_{i=0}^M$
6: **end for**
7: Collect the ensembles

$$\left\{\hat{\boldsymbol{\eta}}^{*(k)}\right\} = \left\{\hat{\boldsymbol{\eta}}^{*(1)}, \hat{\boldsymbol{\eta}}^{*(2)}, \ldots, \hat{\boldsymbol{\eta}}^{*(N)}\right\}$$

$$\left\{\hat{\boldsymbol{\beta}}^{*(k)}\right\} = \left\{\hat{\boldsymbol{\beta}}^{*(1)}, \hat{\boldsymbol{\beta}}^{*(2)}, \ldots, \hat{\boldsymbol{\beta}}^{*(N)}\right\}$$

   and

$$\left[\left\{\hat{\boldsymbol{\xi}}_i^{*(k)}\right\}\right]_{i=0}^M = \left[\hat{\boldsymbol{\xi}}_i^{*(1)}, \hat{\boldsymbol{\xi}}_i^{*(2)}, \ldots, \hat{\boldsymbol{\xi}}_i^{*(N)}\right]_{i=0}^M$$

8: `Construct Confidence Intervals`
9:    Use the desired method to compute confidence intervals on the ensemble of each parameter.
10: `Output`
   Confidence intervals for $\hat{\boldsymbol{\eta}}_{\mathrm{sol}}$, $\hat{\boldsymbol{\nu}}_{\mathrm{sol}}$, $\hat{\boldsymbol{\beta}}_{\mathrm{sol}}$ and $\left\{\hat{\boldsymbol{\xi}}_{\mathrm{sol},i}\right\}_{i=1}^M$ based on the constructed ensemble.

A Monte Carlo ensemble method is used to construct confidence intervals on the unfolded solution, similar to Midtbø *et al.* [7]. The algorithm is summarized in Algorithm 2.

We generate simulated observations by sampling from either the raw data $\mathbf{Y}$ or the refolded solution $\hat{\boldsymbol{\nu}}$. Under the assumption that these are representative of the true parameter $\boldsymbol{\nu}$ and that the data are Poisson-distributed, we can create an ensemble $\left\{\mathbf{Y}^{*(k)}\right\}$ by sampling:

$$Y_{ij}^{*(k)} \sim \mathrm{Poisson}\left(\lambda_{ij}\right) \quad \text{with } \lambda_{ij} = Y_{ij} \text{ or } \hat{\nu}_{ij}. \quad (88)$$

This ensemble is unfolded as before, resulting in an ensemble of solutions $\left\{\hat{\boldsymbol{\eta}}^{*(k)}\right\}$ from which we can construct

a distribution. The choice of λ_{ij} affects the variance of the ensemble, especially when the counts are low. Using $\hat{\nu}_{ij}$ as a mean is preferred because it incorporates information from the unfolding process, providing a more stable estimate than the raw counts Y_{ij}. There is a risk of introducing bias if $\hat{\boldsymbol{\nu}}$ is a poor solution, but in practice this is not a concern since the uncertainty intervals would be appropriately widened.

When background is present, we can either resample the prompt and background spectra separately:

$$B_{ij}^{*(k)} \sim \mathrm{Poisson}\left(B_{ij}\right), \quad (89)$$

$$P_{ij}^{*(k)} \sim \mathrm{Poisson}\left(P_{ij}\right), \quad (90)$$

or sample the estimated parameters and construct the prompt spectrum hierarchically:

$$B_{ij}^{*(k)} \sim \mathrm{Poisson}\left(\left(\hat{\beta}\right)_{ij}\right), \quad (91)$$

$$Y_{ij}^{*(k)} \sim \mathrm{Poisson}\left(\left(\hat{\nu}\right)_{ij}\right), \quad (92)$$

$$P_{ij}^{*(k)} = Y_{ij}^{*(k)} + B_{ij}^{*(k)}. \quad (93)$$

Again the latter approach is preferred as it provides more stable samples by incorporating more information. Contaminants $\left\{\hat{\boldsymbol{\xi}}_i\right\}_{i=1}^M$ are treated identically.

The ensemble distributions tend to be non-normal. Figure 21 illustrates this by showing the distribution of $\left\{\hat{\eta}_{ij}^{*(k)}\right\}$ for a bin where the true value is $\eta_{ij} = 0$, comparing unregularized and regularized MLE solutions. The distributions display pronounced left-skewness with extended right tails. In the regularized case, there is a sharp concentration at zero, consistent with the sparsity-promoting regularization that drives the bin to zero.

The distributions are clearly non-normal. Although gamma and lognormal distributions capture the general shape of the unregularized histogram, they fail Kolmogorov-Smirnov goodness-of-fit tests at conventional significance levels. As the number of counts η_{ij} increases, the distributions become more normal, but rarely reach significance in a Shapiro-Wilks test for normality.

The departure from normality can be quantified through higher-order moments. Both unregularized and regularized solutions exhibit substantial skewness (observed range $1 - 10$) and excess kurtosis (observed range $1 - 10$), with the regularized case showing markedly larger moments. This behavior aligns with expectations: the regularization enhances concentration around true values, while the non-negativity constraint introduces asymmetry near $\eta = 0$. The high excess kurtosis reflects the presence of significant outliers in the distribution tails.

The non-normality of the ensemble $\left\{\hat{\boldsymbol{\eta}}^{*(k)}\right\}$ is not an artifact of the Monte Carlo simulations but fundamental to how the unfolding process transforms the distribution of the observed data.

Using standard percentile intervals for confidence intervals is unsuitable in this context because they do not
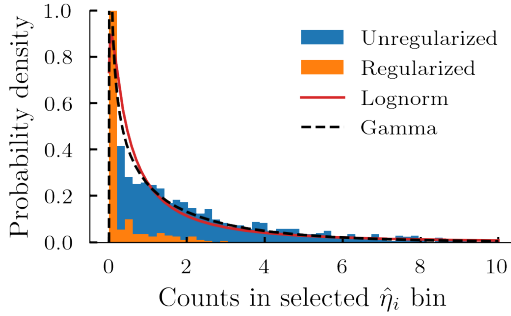
FIG. 21: Distribution of ensemble estimates $\left\{\hat{\eta}_{ij}^{*(k)}\right\}$ for a single bin ij with true value $\eta_{ij} = 0$, comparing unregularized MLE and regularized MLE with sparsity penalty. The regularized distribution shows stronger concentration at zero with reduced tail thickness. Fitted gamma and log-normal distributions (shown for unregularized case) capture the general shape but fail Kolmogorov-Smirnov goodness-of-fit tests. The y-axis is truncated at 1.0.

account for the non-normality of the bin distributions of $\hat{\boldsymbol{\eta}}^{*(k)}$. Instead, we draw on the bootstrap literature to construct bias-corrected and accelerated (BCa) confidence intervals [15], which adjust for bias, variance, and skewness in the sampling distribution. The acceleration parameter required for the BCa method is computed using Jackknife.

Because the data consist of spectra with highly correlated bins, the confidence intervals must account for these correlations to support valid spectra-wise inference. This is achieved using *simultaneous* confidence intervals, which are discussed further in Appendix D. All simultaneous intervals shown here use the Bonferroni correction. For reference, we also include the more familiar *marginal* confidence intervals in each plot.

Alternative approaches to quantify the uncertainty were explored but proved unsuccessful. Methods involving the inverse of the Fisher information matrix fail because they assume that higher-order moments beyond the second are negligible, which is not valid in our context. Additionally, inverting the Hessian matrix is ill-posed due to its near-singular nature, leading to unreliable variance estimates. Likelihood profiles are also unsuitable as they require asymptotic normality, which we do not have.

Methods relying on local curvature, such as those using the second derivative of the likelihood function, also fail for the same reasons. They assume that the log-likelihood surface can be well-approximated by a quadratic form near the maximum likelihood estimate, which is not valid in our case due to the ill-conditioned nature of the problem and the significance of higher-order terms.

Given these significant limitations, the Monte Carlo ensemble method emerges as the most viable approach

for accurately quantifying uncertainty in our unfolding process, as it handles non-normal distributions and avoids the computational and numerical challenges associated with alternative methods.

VII. SYSTEMATICS

Notation Summary:

$\mathbf{G}_\gamma$	Smearing matrix along the gamma energy axis.
$\sigma_\gamma(E_\gamma)$	The resolution along the gamma energy axis.
$\mathbf{D}$	Discrete response.
$\boldsymbol{\mu}$	The expectation value of the unfolded spectrum.
$\boldsymbol{\eta}$	The expectation value of the unfolded spectrum refolded by $\mathbf{G}_\gamma$.
$\boldsymbol{\nu}$	The expectation value of the folded spectrum.
$\mathbf{y}$	The observed data $\mathbf{y} \sim \text{Poisson}\left(\boldsymbol{\nu} = \mathbf{G}_\gamma \mathbf{D} \boldsymbol{\mu}\right)$.
$\mathcal{M}, \mathcal{H}, \mathcal{N}$	The spaces which $\boldsymbol{\mu}, \boldsymbol{\eta}$ and $\boldsymbol{\nu}$ belong, respectively.
$\hat{\boldsymbol{\eta}}$	RMLE estimate of $\boldsymbol{\eta}$.
$\hat{\boldsymbol{\eta}}^*$	Monte Carlo estimate or ensemble, depending on context.

The performance of RMLE is mostly determined by structural features of the input data and the unfolding setup. In this section, we analyze how of spectral complexity influence the reliability of the reconstructed spectrum and the coverage of the associated confidence intervals.

A. Low spectral complexity

Spectra exhibiting low spectral complexity are generally more amenable to unfolding. As outlined in Sec. IV D, spectral complexity relates to the presence of fluctuations and features in the underlying signal $\boldsymbol{\eta}$. When this signal has a relatively simple structure, the task of applying and tuning appropriate regularization methods becomes more straightforward, mitigating spurious peaks and oscillations in the unfolded result $\hat{\boldsymbol{\eta}}$. We can broadly categorize these simpler cases into discrete and smooth:

Discrete spectra: This category includes spectra composed of a small number of distinct, well-separated peaks. It is their separability that simplifies the problem. Regularization techniques that promote sparsity are particularly effective in such cases, as they align with the inherently sparse nature of the true signal $\boldsymbol{\eta}$, such as sparsity cost functions or minimum entropy criteria (see Sec. IV C). An instance of this category is the single-peak scenario, which will be discussed in Sec. VIII. Although the discrete peak region in Oslo Method data is not

typically used for direct extraction of the nuclear level density or gamma-strength function, its accurate unfolding is important for recovering the first-generation spectrum, see Appendix F.

Smooth spectra: The second category involves smooth spectra, often arising in scenarios with high nuclear level density, where individual energy levels are unresolved and merge into a (quasi-)continuum, *and* where the gamma cascades don't strongly feed through some low lying states. These spectra lack dominant, isolated structures. For such cases, regularization methods designed to enforce smoothness are preferred. Techniques like Tikhonov regularization, minimizing a Sobolev norm, or employing maximum entropy principles penalize high-frequency oscillations and favor the expected smooth behavior of $\boldsymbol{\eta}$.

The spectrum of a ^{166}Ho-like spectrum serves as a practical example of a smooth case, owing to its high level density. Figure 22 presents results from unfolding a simulated ^{166}Ho spectrum at $4\,\text{MeV}$. It compares an unregularized solution $\hat{\boldsymbol{\eta}}_0^*$ with a solution regularized using a Sobolev norm $\hat{\boldsymbol{\eta}}^*$. While the refolded versions of both solutions ($\hat{\boldsymbol{\nu}}_0^*$ and $\hat{\boldsymbol{\nu}}^*$) provide excellent fits to the ideal folded data $\boldsymbol{\nu}$ (with uncertainty bands significantly smaller than the Poisson noise), their unfolded counterparts $\hat{\boldsymbol{\eta}}$ differ markedly. The unregularized solution $\hat{\boldsymbol{\eta}}_0^*$ exhibits excessive higher-frequency oscillations. In contrast, the regularized solution $\hat{\boldsymbol{\eta}}^*$ is smooth, consistent with the expected nature of a continuum spectrum. Consequently, the uncertainty bands associated with the unregularized $\hat{\boldsymbol{\eta}}_0^*$ are wider and less smooth than that of the regularized $\hat{\boldsymbol{\eta}}^*$.

B. High spectral complexity

A significant challenge in analyzing Oslo spectra arises from their inherent high spectral complexity, which manifests as overlapping distinct peaks with varying amplitudes and widths, and a smoother underlying component. These structures are exemplified in the simulated ^{120}Sn-like spectrum shown in Fig. 23. The presence of such structures makes the application of regularization techniques challenging. No single regularization method has proven consistently effective for accurately unfolding these complex spectra. Consequently, unfolding high complexity spectra results in wide and fluctuating uncertainty bands. In this specific instance, the simultaneous confidence interval contains the true $\boldsymbol{\eta}$, whereas not all marginal CIs do. However, the simultaneous CIs are not guaranteed to always contain the true solution.

Further analysis of both regularization type and strength, as they relate to spectra of varying spectral complexity, is presented in Appendix G.
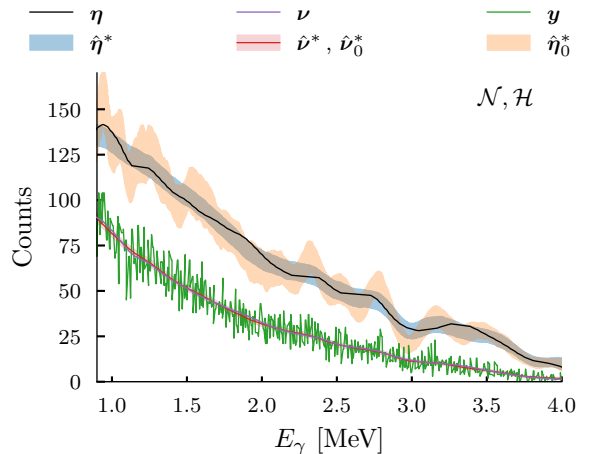

FIG. 22: Unfolding of a simulated ^{166}Ho-like spectrum at $E_{\text{in}} = 4\,\text{MeV}$. Shown are the unregularized solution $\hat{\boldsymbol{\eta}}_0^*$ and the regularized solution $\hat{\boldsymbol{\eta}}^*$ (using a Sobolev norm), both with marginal uncertainty bands. The true underlying spectrum $\boldsymbol{\eta}$ is shown as solid black line. Although the corresponding refolded spectra, $\hat{\boldsymbol{\nu}}_0^*$ and $\hat{\boldsymbol{\nu}}^*$, both closely match the measured spectrum $\boldsymbol{\nu}$—with narrow uncertainty bands not discernible in the plot and therefore plotted together—the unregularized $\hat{\boldsymbol{\eta}}_0^*$ exhibits substantial oscillations compared to the smoother $\hat{\boldsymbol{\eta}}^*$. Simultaneous CI are not shown.

C. Coverage probability

Having mapped how different regularization schemes influence point estimates we now turn to the associated uncertainty estimates. Specifically, we assess whether the confidence intervals produced by the RMLE procedure attain their nominal coverage probability. The definition and equations for coverage are given in Appendix E.

Ideally we would assess the coverage behavior of RMLE for every possible gamma-ray spectrum, but this is impractical. A given element η_i will correspond to different physical features in different spectra, and the confidence-region width varies with both spectral complexity and the chosen regularization. Coverage must therefore be evaluated within a defined class of spectra and regularization scheme. Taking a pragmatic approach, we here test RMLE on three representative cases spanning the complexity range studied earlier: a discrete single-peak spectrum, a smooth ^{166}Ho-like spectrum, and a high-complexity ^{120}Sn-like spectrum.

Spectrum coverage is used to denote the set of empirical coverage probabilities $\hat{p}(\boldsymbol{\eta})$ across all bins for a given spectrum:

$$\hat{p}(\boldsymbol{\eta}) \;=\; \big\{\hat{p}(\eta_i) : i = 1, \ldots, n\big\}. \tag{94}$$

This set is summarized by the mean and the median.

Figure 24 illustrates this notion for a sharply peaked spectrum, using three different regularization strengths
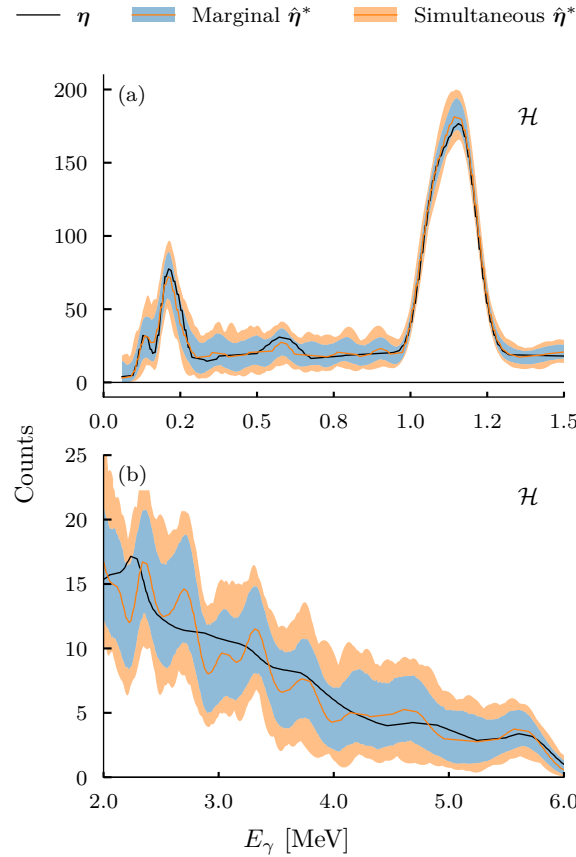
FIG. 23: Unfolding of a complex simulated ^{120}Sn-like spectrum ($E_{\text{in}} = 6\,\text{MeV}$). (a) Low energy region with a large peak in a otherwise smooth spectrum. (b) Higher energy region with a smoother spectrum. The spectrum's complex structure poses a challenge for regularization, resulting in an unfolded solution with wide, fluctuating uncertainty bands. Both marginal and simultaneous confidence intervals (CI) are displayed. The simultaneous CI always contains the true solution in this particular example, while the marginal CI does not (e.g., $E_\gamma = 2.2\,\text{MeV}$).

FIG. 24: Spectrum coverage for a peaked delta-spectrum under different regularization strengths α. The colored bands indicate the standard error of the Monte Carlo estimate (E3). Regularization strength $\alpha = 100$ minimizes the Wasserstein distance $W_1(\hat{\boldsymbol{\eta}}, \boldsymbol{\eta})$ (see Appendix G). The coverage of simultaneous intervals is not shown as they are indistinguishable from 0. The black diagonal represents perfect coverage.

α. When no regularization is used ($\alpha = 0$), the unfolding introduces spurious peaks that draw counts away from the true signal. This results in systematic undercoverage across all confidence levels. These intervals fail to capture the signal, despite the fact that the overall reconstruction $\hat{\boldsymbol{\eta}}$ may be close to $\boldsymbol{\eta}$ in terms of global metrics like D_{KL} and Wasserstein distance W_1. As α increases, these spurious features are suppressed, and spectrum coverage improves. The spectrum coverage becomes conservative at low confidence levels, but still undercover at high confidence levels.

Even with an appropriate regularization strength, the distribution of spectrum coverage is very wide. Bins far from the signal are often numerically zero, and their intervals trivially cover the true value, leading to overcover-
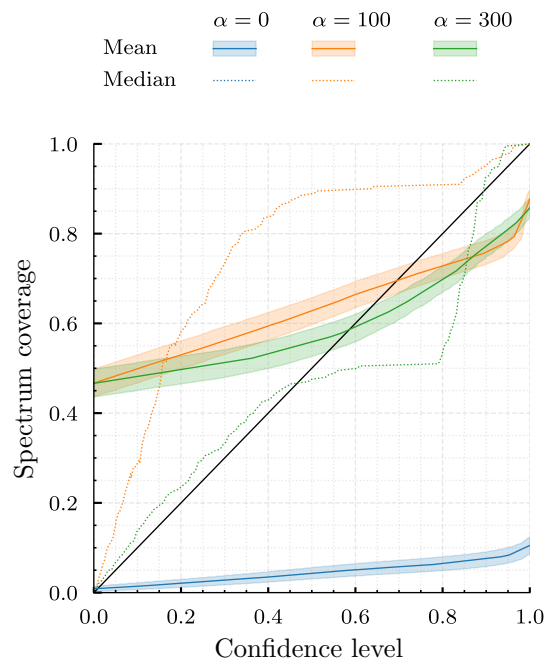
age. In contrast, bins on the lower tails of peaks may consistently miss the target due to narrow ensemble spread, resulting in near-zero coverage. These effects lead to the flat behavior of the spectrum coverage curves, e.g., the dotted green curve ($\alpha = 300$) in Fig. 24, which stays roughly constant from 0.5 to 0.8. By the same reason, simultaneous intervals achieve zero coverage, and the associated curves are therefore omitted from the figure.

In contrast, a ^{166}Ho-like spectrum does not have these problems, as shown in Fig. 25. The MC ensemble is much narrower for both the unregularized and regularized case, leading to the means and median coinciding. Without regularization the spectral complexity is too high, but on average the MC ensemble $\hat{\boldsymbol{\eta}}^{*(k)}$ will generally cover the true $\boldsymbol{\eta}$. The marginal spectrum coverage is nearly calibrated, but with minor undercoverage for all confidence levels. Sobolev regularization models the spectral complexity correctly, resulting in overcoverage for nearly all confidence levels. The simultaneous spectrum coverage has severe undercoverage without regularization, but has much better calibration with regularization, as desired.

Figure 26 shows the result for a ^{120}Sn-like spectrum. Despite the higher spectral complexity and lack of regularization, the spectrum coverage here behaves more pre-
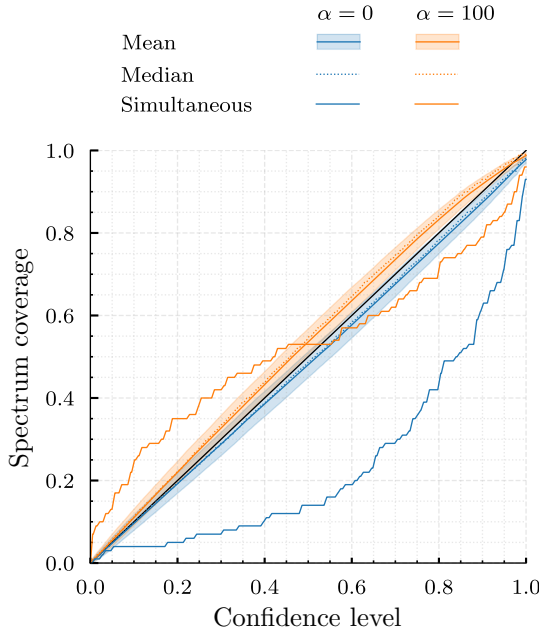
FIG. 25: Spectrum coverage for a ^{166}Ho-like spectrum.
Without regularization ($\alpha = 0$), the (marginal)
spectrum coverage is mostly calibrated, but with
systematic undercoverage. Sobolev regularization with
strength that minimizes the W_1 cost ($\alpha = 100$) gives
minor systematic overcoverage. The spectrum coverage
of studentized supremum simultaneous interval greatly
improves with regularization.

dictably. While some systematic undercoverage remains
due to the mismatched spectral complexity, it is less se-
vere and more evenly distributed than the peaked spec-
trum, but worse than ^{166}Ho. The spectral mismatches
are stochastic and do not lead to large systematic over-
or undercoverage, which makes the simultaneous cover-
age behavior nearly calibrated, but with some undercov-
erage.

In general, the RMLE confidence intervals exhibit rea-
sonably good calibration, particularly when an appropri-
ate regularization scheme is used. However, confidence
levels should never be interpreted naively; their valid-
ity depends on the spectral context and the underlying
assumptions of the unfolding process, which the practi-
tioner must always take into account.

VIII. COMPARISON TO FICS

FICS (Folding Iteration with Compton Subtraction)
is the standard unfolding algorithm used in the Oslo
Method and serves as a natural benchmark for com-
parison. Examples of its applications include [16–20]).
As a variant of Richardson's iterative method (see Ap-
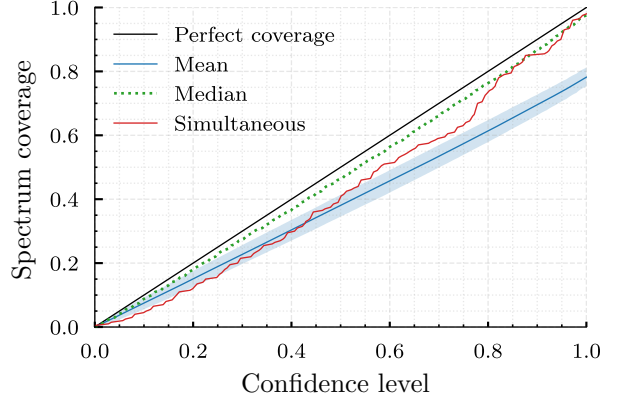pendix A 8), FICS inherits its core operational principle

FIG. 26: Spectrum coverage for a complex ^{120}Sn
spectrum. The Monte Carlo spread is much narrower
than in Fig. 24, and the mean and median nearly
coincide.

and limitations. Iterative methods like FICS function by
minimizing the residuals $|\mathbf{y} - \hat{\boldsymbol{\nu}}|$ between the refolded es-
timate $\hat{\boldsymbol{\nu}}$ and the measured data $\mathbf{y}$, effectively performing
a stepwise partial inversion of the detector response.

However, a fundamental issue arises because the mini-
mization target is the noisy experimental data $\mathbf{y}$, rather
than the underlying true folded distribution $\boldsymbol{\nu}$. Conse-
quently, the iterative process inevitably incorporates and
amplifies noise (see discussion in Sec. IV D) present in $\mathbf{y}$,
leading to overfitting. The severity of this overfitting is
influenced by the condition number of the response ma-
trix as shown in Sec. II D. The primary technique used to
mitigate this in FICS and similar methods is early stop-
ping, halting the iteration before convergence becomes
excessive. FICS employs a cost function that combines
a weighted chi-square term with a fluctuation penalty
based on the residuals between the unfolded estimate $\hat{\boldsymbol{\eta}}$
and its smoothed counterpart. For a detailed theoreti-
cal discussion, including methodological challenges in di-
rectly comparing FICS and RMLE, see Appendix H.

The inherent weaknesses of this iterative approach,
particularly its susceptibility to noise and absence of
physical constraints, are illustrated through the exam-
ple of unfolding a single peak. This scenario is especially
sensitive to noise and degeneracies in the response ma-
trix. Figure 27 shows the setup: the true underlying
distribution $\boldsymbol{\eta}$ peaking at $3.5\,\mathrm{MeV}$, the folded distribu-
tion $\boldsymbol{\nu}$, and the Poisson-sampled data $\mathbf{y}$ used as input.
To isolate the effect of the algorithm, no background or
contaminants are included.

Fig. 28 shows the evolution of the FICS solution $\hat{\boldsymbol{\eta}}$
over successive iterations. This demonstrates two critical
weaknesses (these are expected, see Appendix A 8):

Noise amplification and spurious features: The it-
erative process does not distinguish between signal
and noise in $\mathbf{y}$. As a result, noise is integrated into
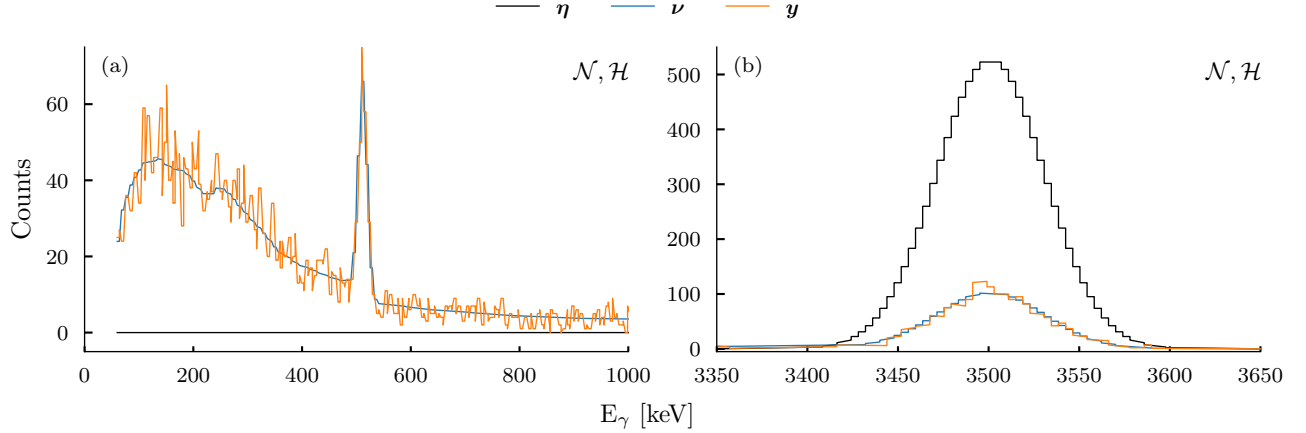the solution from the very first iteration. Spuri-

FIG. 27: A single peak at $3.5\,\mathrm{MeV}$, the folded spectrum $\boldsymbol{\nu}$ and a Poisson sample $\mathbf{y}$. The spectrum has been split in two to make the finer details visible, with a lower E_γ region (a) and a higher E_γ region (b). The region in between (not shown) is comprised of Compton, single-escape and double-escape events.
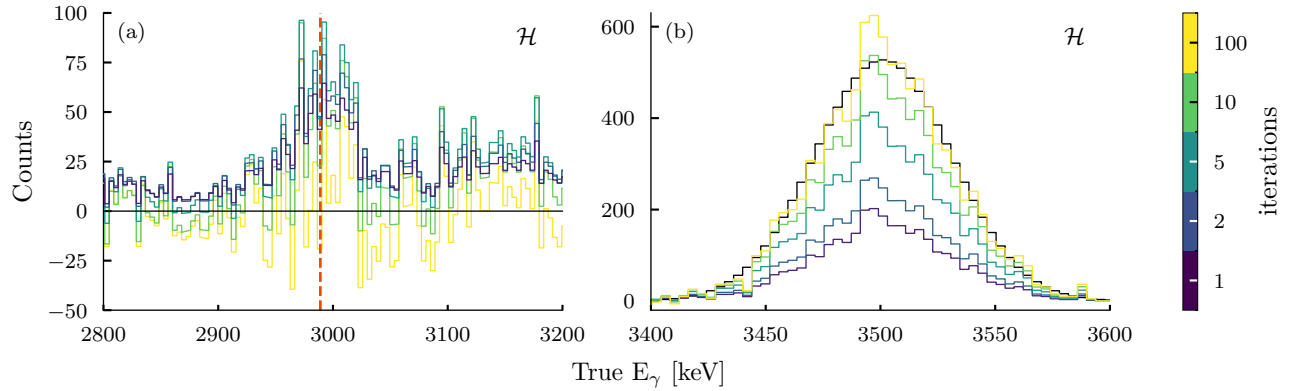

FIG. 28: The unfolded $\hat{\boldsymbol{\eta}}$ solution of FICS with increasing number of iterations (colored lines), compared to the true distribution $\boldsymbol{\eta}$ (black line), shown for the lower (a) and upper (b) regions. The energy of the single escape peak $(3.5\,\mathrm{MeV} - 511\,\mathrm{keV})$ is indicated by a dashed vertical red line. In the lower region (a), where the true $\boldsymbol{\eta} = 0$, FICS overfits to noise immediately, while bins in the upper region (b) where $\boldsymbol{\eta} > 0$ require more iterations to converge toward the peak, albeit with added noise. The spurious peak in the lower region is due to the single escape peak being misinterpreted as signal. For illustration, the step size was set to 0.3 times the optimal step size [see Eq. (A31)], allowing the small updates of FICS to be visible. For comparison, using the reduced step size means that iteration 100 here corresponds roughly to iteration 15 with the standard step size of 1.

ous features, such as oscillations around zero and false peaks (particularly prominent in the lower energy region, left panel), converge rapidly—often faster than the actual signal peak (right panel). Early stopping in such a case yields an unsatisfactory compromise: the true peak is underestimated, while significant spurious noise structures remain. A notable example is the spurious peak near $2.99\,\mathrm{MeV}$ ($3.5\,\mathrm{MeV}$ - $511\,\mathrm{keV}$), corresponding to the single escape peak (marked by the red dashed line). We found that insufficient regularization frequently causes unfolding methods to misinterpret noise associated with strong response features (like

escape peaks) as genuine peaks in $\boldsymbol{\eta}$.

Unphysical negative values: FICS does not inherently restrict the solution space to non-negative values. While negative values can arise in purely mathematical solutions, they are unphysical. Their presence indicates the method's failure to confine the solution to a physically meaningful space. Simply rectifying (removing or redistributing negative values through some procedure) post-unfolding does not address this underlying deficiency. Negative counts in the input data $\mathbf{y}$ typically signal issues like improper background subtraction as dis-

cussed in Sec. V C. Negative counts in the unfolded solution can also stem from an inaccurate response matrix.

Comparing the final unfolded solutions $\hat{\boldsymbol{\eta}}$ from FICS and RMLE, shown in Fig. 29, the FICS result is characterized by significant bin-to-bin fluctuations, whereas the RMLE solution is smooth and more closely approximates the true $\boldsymbol{\eta}$. This reflects their differing approaches: FICS fits the noisy data deterministically, while RMLE treats the data stochastically. As described in Secs. IV C and IV D, not properly accounting for the different sources of variation will lead to fluctuations in the solution. This difference is further emphasized by the refolded solutions $\hat{\boldsymbol{\nu}}$ in Fig. 30. FICS's $\hat{\boldsymbol{\nu}}$ almost perfectly reproduces the noise profile of the input $\mathbf{y}$, confirming overfitting. In contrast, RMLE's $\hat{\boldsymbol{\nu}}$ converges towards the smooth, true folded distribution $\boldsymbol{\nu}$.

The uncertainty bands for FICS $\hat{\boldsymbol{\eta}}$ (calculated via Monte Carlo using the method of Midtbø et $al.$ [7]) are wide and fluctuating, reflecting the high variance introduced by fitting to the noise in $\mathbf{y}$. In contrast, RMLE estimates the regularized expectation value of $\hat{\boldsymbol{\eta}}$, making it less sensitive to input noise and resulting in substantially narrower uncertainty bands (calculated as described in Sec. VI).[28] This also illustrates a point made in Sec. VI A: using $\hat{\boldsymbol{\nu}}$ as a basis for resampling is preferable once $\hat{\boldsymbol{\nu}}$ has converged sufficiently close to $\boldsymbol{\nu}$. If, instead, $\mathbf{y}$ is used as the resampling basis—as in the approach of Midtbø—the noise in $\mathbf{y}$ introduces both greater bias and higher variance in the resulting ensemble.

This juxtaposition of $\hat{\boldsymbol{\eta}}$ and $\hat{\boldsymbol{\nu}}$ underscores why relying solely on the residuals $|\mathbf{y} - \hat{\boldsymbol{\nu}}|$ to assess unfolding quality is deceptive. FICS demonstrates that achieving a low residual (a good fit to $\mathbf{y}$) does not guarantee an accurate estimation of the true underlying distribution $\boldsymbol{\eta}$. Indeed, convergence to the noise in $\mathbf{y}$ prevents convergence to the true $\boldsymbol{\eta}$. Moreover, even perfect convergence to the true $\boldsymbol{\nu}$ would not yield a unique $\hat{\boldsymbol{\eta}}$ due to the inherent degeneracy (ill-posedness) of the unfolding problem (Sec. IV C). While the spuriousness of the FICS $\hat{\boldsymbol{\eta}}$ is relatively obvious in this simple single-peak test case, identifying such artifacts in complex experimental spectra by visual inspection alone is practically impossible.

---

[28] Note that the confidence intervals of $\hat{\boldsymbol{\nu}}$ in the lower region, Fig. 30(a), fail to cover the true $\boldsymbol{\nu}$ due to the ensemble spread discussed in Sec. VII C.
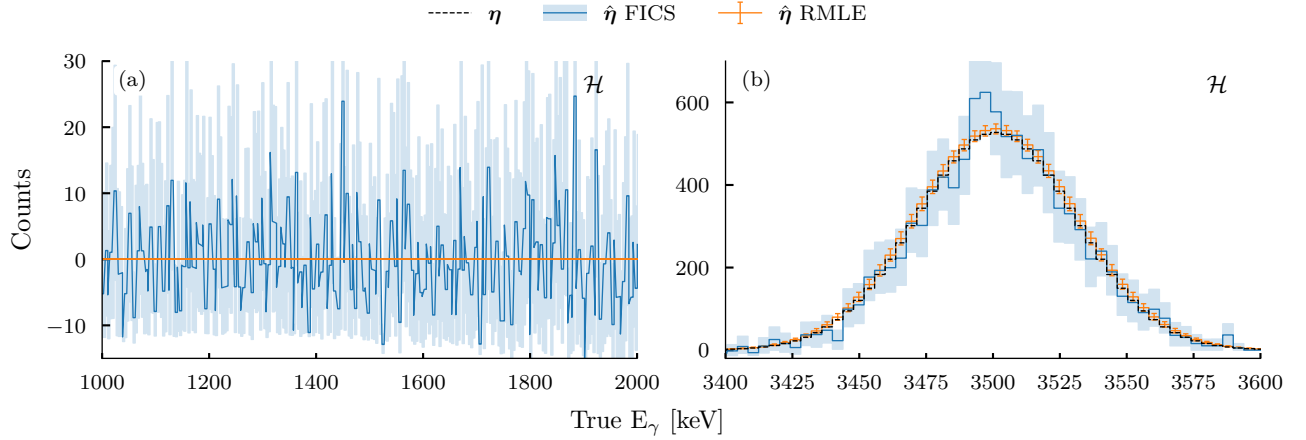
FIG. 29: Comparison of the unfolded estimate $\hat{\boldsymbol{\eta}}$ to the true distribution $\boldsymbol{\eta}$ (dashed black line), along with associated 2σ uncertainty bands in the lower (a) and upper (b) regions. The RMLE solution is completely smooth and closely tracks the true $\boldsymbol{\eta}$, with their curves nearly overlapping; the corresponding uncertainty band is so narrow in the lower region (a) that it is not visible. In contrast, the FICS solution exhibits substantial noise and wider, more irregular uncertainty bands, reflecting overfitting to noise in the ensemble members. The CIs are marginal.
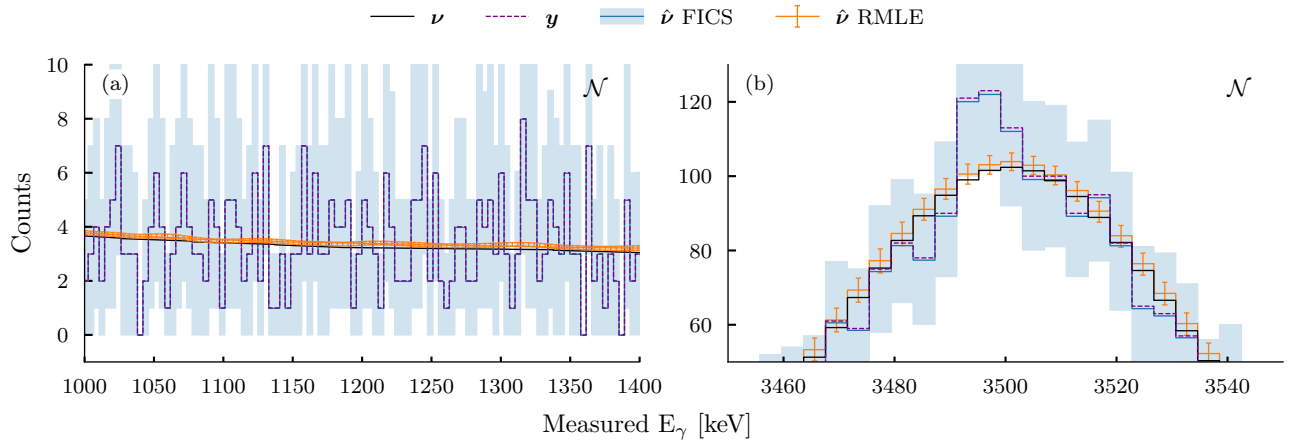

FIG. 30: Comparison of the refolded solutions $\hat{\boldsymbol{\nu}}$ to the true $\boldsymbol{\nu}$ (black line) and to the observed data $\mathbf{y}$ (dashed purple line), shown for the lower (a) and upper (b) regions. The refolded FICS solution perfectly fits the observed data $\mathbf{y}$, while the refolded RMLE solution almost perfectly fits the true $\boldsymbol{\nu}$. The wider and fluctuating uncertainty bands of FICS reflect the incorporation of noise. The CIs are marginal.

IX.   SUMMARY AND OUTLOOK

In this work, we introduced a novel method for unfolding gamma-ray spectra, specifically tailored for the Oslo Method. This approach addresses key limitations of traditional unfolding techniques, such as their tendency to overfit noise and inability to provide reliable uncertainty estimates. By combining regularized maximum log-likelihood optimization with Monte Carlo simulations, the method offers more robust and transparent confidence intervals, particularly for spectra characterized by low complexity.

We developed a theoretical framework to better understand the challenges of unfolding, which helped guide the design of the method to reduce overfitting. For simpler low complexity spectra, the regularization scheme proved highly effective, producing narrow confidence intervals that accurately cover the true solutions. This success arises from the ability to incorporate prior knowledge into the regularization cost function.

For high-complexity spectra, the regularization schemes were less effective. Non-statistical noise and the diversity of spectral structures lead to difficulties in constraining the solutions. As a result, handling the variability across different types of spectra remains a challenge in unfolding gamma-ray spectra for Oslo Method applications.

Moving forward, the unfolding methodology can be improved by addressing the challenges encountered in this work:

1. *New regularization schemes based on physical principles:* A significant obstacle for improved unfolding is the lack of general regularization schemes. Developing regularization schemes grounded in physical principles, rather than relying solely on statistical methods, will better capture the underlying nature of the spectra.

2. *Develop adaptive regularization:* Barring physics-based regularization, combine standard regularization schemes to handle high-complexity spectra. The main problem here is finding schemes that combine, and that have parameters that are feasible to tune.

3. *Parameter tuning:* Implementing techniques to predict optimal regularization parameters based on the structure of the input spectra and nuclear systematics.

4. *Response function discrepancy correction:* Investigating how to systematically correct for discrepancies between modeled and true detector response functions.

We believe answering these problems would improve the method's applicability to more complex and varied gamma-ray spectra.

ACKNOWLEDGMENTS

Appendix A: Mathematical background and proofs

This section collects some linear–algebra material used in the paper. We recall only what we need—namely the four fundamental subspaces of a matrix $\mathbf{R} \in \mathbb{R}^{m \times n}$: $\mathrm{Ran}(\mathbf{R})$, $\mathrm{Ker}(\mathbf{R})$, $\mathrm{Ran}(\mathbf{R}^{\top})$, and $\mathrm{Ker}(\mathbf{R}^{\top})$—and fix notation for the rank–nullity identity and the standard orthogonality relations between these spaces. We also provide the Moore-Penrose pseudoinverse and the associated Penrose equations. Further, we present short proofs of the statements invoked in the main text, so the arguments there can be read without interruption. The presentation is deliberately minimal: it is not a self-contained primer, and for results or background not proved here we refer to standard references in linear-algebra, convex analysis and statistical analysis.

1. Four Fundamental Subspaces

1. The range of $\mathbf{R}$, denoted $\mathrm{Ran}(\mathbf{R})$, is the set of all possible values that $\mathbf{R}\boldsymbol{\mu}$ can take for any vector $\boldsymbol{\mu} \in \mathbb{R}^n$. Formally, for a linear map $\mathbf{R} : \mathbb{R}^n \to \mathbb{R}^m$, it is defined as:

$$\mathrm{Ran}(\mathbf{R}) = \{\mathbf{R}\boldsymbol{\mu} \,|\, \boldsymbol{\mu} \in \mathbb{R}^n\}, \qquad (A1)$$

which in our case represents the set of all smeared means. This is also sometimes called the column space of $\mathbf{R}$.

2. The null space of $\mathbf{R}$, denoted $\mathrm{Ker}(\mathbf{R})$, consists of all vectors $\boldsymbol{\lambda} \in \mathbb{R}^n$ that $\mathbf{R}$ maps to zero:

$$\mathrm{Ker}(\mathbf{R}) = \{\boldsymbol{\lambda} \in \mathbb{R}^n \,|\, \mathbf{R}\boldsymbol{\lambda} = 0\}. \qquad (A2)$$

This space contains all directions in which $\mathbf{R}$ has no effect. When $\mathbf{R}$ is ill-conditioned, $\mathrm{Ker}(\mathbf{R})$ is non-trivial, meaning there are vectors other than zero that lie in this space.

3. Let $\mathbf{R}^{\mathrm{T}}$ denote the transpose of $\mathbf{R}$. Then, $\mathrm{Ran}(\mathbf{R}^{\mathrm{T}})$ is the set of all linear combinations of the rows of $\mathbf{R}$:

$$\mathrm{Ran}(\mathbf{R}^{\mathrm{T}}) = \{\mathbf{R}^{\mathrm{T}}\mathbf{v} \,|\, \mathbf{v} \in \mathbb{R}^m\}, \qquad (A3)$$

and is called the row space of $\mathbf{R}$.

4. The left null space of $\mathbf{R}$, denoted $\mathrm{Ker}(\mathbf{R}^{\mathrm{T}})$, consists of all vectors $\mathbf{v} \in \mathbb{R}^m$ such that $\mathbf{R}^{\mathrm{T}}\mathbf{v} = 0$. Formally, it is defined as:

$$\mathrm{Ker}(\mathbf{R}^{\mathrm{T}}) = \{\mathbf{v} \in \mathbb{R}^m \,|\, \mathbf{R}^{\mathrm{T}}\mathbf{v} = 0\}. \qquad (A4)$$

This space contains all vectors that lie in the kernel of the transpose of $\mathbf{R}$, representing directions that are annihilated by $\mathbf{R}^{\mathrm{T}}$.

Then, the *Four Fundamental Subspaces Theorem* establishes the following orthogonality relations:

$$\mathrm{Ker}(\mathbf{R}) = \mathrm{Ran}(\mathbf{R}^T)^{\perp}, \qquad (A5)$$

$$\mathrm{Ker}(\mathbf{R}^{\mathrm{T}}) = \mathrm{Ran}(\mathbf{R})^{\perp}. \qquad (A6)$$

These relations describe the fact that:

- The null space of $\mathbf{R}$ is the orthogonal complement of the range (row space) of $\mathbf{R}^{\mathrm{T}}$. That is, every vector in $\mathrm{Ker}(\mathbf{R})$ is orthogonal to all vectors in $\mathrm{Ran}(\mathbf{R}^{\mathrm{T}})$.

- The null space of $\mathbf{R}^T$ is the orthogonal complement of the range (column space) of $\mathbf{R}$. This means that every vector in $\mathrm{Ker}(\mathbf{R}^{\mathrm{T}})$ is orthogonal to all vectors in $\mathrm{Ran}(\mathbf{R})$.

2. Moore–Penrose Pseudoinverse

For a matrix $\mathbf{R} \in \mathbb{R}^{m \times n}$, the *Moore–Penrose pseudoinverse* $\mathbf{R}^{\dagger} \in \mathbb{R}^{n \times m}$ is the unique matrix satisfying the *Penrose equations*:

$$\mathbf{R}\mathbf{R}^{\dagger}\mathbf{R} = \mathbf{R}, \qquad \mathbf{R}^{\dagger}\mathbf{R}\mathbf{R}^{\dagger} = \mathbf{R}^{\dagger}, \qquad (A7)$$

$$(\mathbf{R}\mathbf{R}^{\dagger})^{\mathrm{T}} = \mathbf{R}\mathbf{R}^{\dagger}, \qquad (\mathbf{R}^{\dagger}\mathbf{R})^{\mathrm{T}} = \mathbf{R}^{\dagger}\mathbf{R}. \qquad (A8)$$

These imply that $\mathbf{R}\mathbf{R}^{\dagger}$ and $\mathbf{R}^{\dagger}\mathbf{R}$ are the orthogonal projectors onto $\mathrm{Range}(\mathbf{R})$ and $\mathrm{Range}(\mathbf{R}^{\mathrm{T}})$, respectively. If $\mathbf{R}$ has rank r and singular value decomposition (SVD) $\mathbf{R} = \mathbf{U}\boldsymbol{\Sigma}\mathbf{V}^{\mathrm{T}}$, with

$$\boldsymbol{\Sigma} = \begin{bmatrix} \mathrm{diag}(\sigma_1, \ldots, \sigma_r) & 0 \\ 0 & 0 \end{bmatrix}, \quad \sigma_i > 0,$$

then

$$\mathbf{R}^{\dagger} = \mathbf{V}\boldsymbol{\Sigma}^{\dagger}\mathbf{U}^{\mathrm{T}}, \qquad \boldsymbol{\Sigma}^{\dagger} = \begin{bmatrix} \mathrm{diag}(\sigma_1^{-1}, \ldots, \sigma_r^{-1}) & 0 \\ 0 & 0 \end{bmatrix}.$$

This definition extends inversion to rank-deficient matrices: if $\mathbf{R}$ is invertible, $\mathbf{R}^{\dagger} = \mathbf{R}^{-1}$.

3. Proof of theorem II.1

Proof: Let $\mathbf{P}_{\mathcal{R}} := \mathbf{R}\mathbf{R}^{\dagger}$ and $\mathbf{P}_{\mathcal{K}} := \mathbf{I} - \mathbf{R}^{\dagger}\mathbf{R}$, the orthogonal projectors onto $\mathrm{Range}(\mathbf{R})$ and $\mathrm{Ker}(\mathbf{R})$, respectively, by the Penrose equations.

The least-squares problem

$$\min_{\boldsymbol{\mu}} \|\mathbf{R}\boldsymbol{\mu} - \mathbf{y}\|_2$$

is solved by projecting $\mathbf{y}$ onto $\mathrm{Range}(\mathbf{R})$, giving the minimal residual $\mathbf{p} = \mathbf{P}_{\mathcal{R}}\mathbf{y}$. One minimizer is

$$\boldsymbol{\mu}_0 = \mathbf{R}^{\dagger}\mathbf{y},$$

since $\mathbf{R}\boldsymbol{\mu}_0 = \mathbf{R}\mathbf{R}^\dagger\mathbf{y} = \mathbf{p}$. If $\boldsymbol{\mu}$ is any other minimizer, then

$$\mathbf{R}(\boldsymbol{\mu} - \boldsymbol{\mu}_0) = \mathbf{R}\boldsymbol{\mu} - \mathbf{R}\boldsymbol{\mu}_0 = 0,$$

so $\boldsymbol{\mu} - \boldsymbol{\mu}_0 \in \mathrm{Ker}(\mathbf{R})$. Thus every solution has the form

$$\boldsymbol{\mu} = \boldsymbol{\mu}_0 + \boldsymbol{\lambda}, \quad \boldsymbol{\lambda} \in \mathrm{Ker}(\mathbf{R}).$$

Finally, any $\boldsymbol{\lambda} \in \mathrm{Ker}(\mathbf{R})$ can be written as $\boldsymbol{\lambda} = \mathbf{P}_\mathcal{K}\boldsymbol{v} = (\mathbf{I} - \mathbf{R}^\dagger\mathbf{R})\boldsymbol{v}$ for some $\boldsymbol{v} \in \mathbb{R}^n$, proving the claim:

$$\boldsymbol{\mu}_{\mathrm{LS}} = \mathbf{R}^\dagger\mathbf{y} + (\mathbf{I} - \mathbf{R}^\dagger\mathbf{R})\boldsymbol{v}, \quad \boldsymbol{v} \in \mathbb{R}^n.$$

$\square$

4. Proof of corollary II.2

Proof From Theorem II.1, the least-squares solutions are

$$\hat{\boldsymbol{\mu}}_{\mathrm{LS}} = \mathbf{R}^\dagger\mathbf{y} + \boldsymbol{\lambda}, \quad \boldsymbol{\lambda} \in \mathrm{Ker}(\mathbf{R}).$$

The solution is unique if and only if the only possible $\boldsymbol{\lambda}$ is $\mathbf{0}$, i.e., when $\mathrm{Ker}(\mathbf{R}) = \{\mathbf{0}\}$. Equivalently, $\mathbf{R}$ has full column rank (and for square $\mathbf{R}$, is invertible), in which case $\mathbf{R}^\dagger = \mathbf{R}^{-1}$ and

$$\hat{\boldsymbol{\mu}}_{\mathrm{LS}} = \mathbf{R}^{-1}\mathbf{y}.$$

$\square$

5. Proof of proposition II.3

Proof: We will prove this by contradiction, considering two cases where $\boldsymbol{\lambda}$ is either entirely non-positive or entirely non-negative. The key to the proof is to use the orthogonality relation between $\mathrm{Ker}(\mathbf{R})$ and $\mathrm{Ran}(\mathbf{R}^{\mathrm{T}})$.

The orthogonality relation implies that for all $\boldsymbol{\lambda} \in \mathrm{Ker}(\mathbf{R})$ and for all $\mathbf{v} \in \mathrm{Ran}(\mathbf{R}^{\mathrm{T}})$, the inner product takes the form

$$\langle \boldsymbol{\lambda}, \mathbf{v} \rangle = \boldsymbol{\lambda}^{\mathrm{T}}\mathbf{v} = 0. \tag{A9}$$

Suppose, for contradiction, that $\boldsymbol{\lambda}$ is either entirely non-positive or non-negative.

Without loss of generality, we first assume $\boldsymbol{\lambda} \geq 0$ component wise and $\boldsymbol{\lambda} \neq 0$. Since $\mathbf{R}^{\mathrm{T}}$ has non-negative entries (because $\mathbf{R}$ does), any vector $\mathbf{v} \in \mathrm{Ran}(\mathbf{R}^{\mathrm{T}})$ obtained from a non-negative $\mathbf{w} \in \mathbb{R}^m$ will also have non-negative components. Choose $\mathbf{w}$ with non-negative components and at least one positive component, and define $\mathbf{v} = \mathbf{R}^{\mathrm{T}}\mathbf{w}$. Then $\mathbf{v} \geq 0$ component wise and $\mathbf{v} \neq 0$, because $\mathbf{w}$ is not the zero vector and $\mathbf{R}^{\mathrm{T}}$ has no zero columns (since $\mathbf{R}$ has no zero rows).

Now, compute the inner product

$$\langle \boldsymbol{\lambda}, \mathbf{v} \rangle = \boldsymbol{\lambda}^{\mathrm{T}}\mathbf{v} = \boldsymbol{\lambda}^{\mathrm{T}}(\mathbf{R}^{\mathrm{T}}\mathbf{w}) = (\mathbf{R}\boldsymbol{\lambda})^{\mathrm{T}}\mathbf{w} = 0. \tag{A10}$$

The inner product is a sum of non-negative terms

$$\langle \boldsymbol{\lambda}, \mathbf{v} \rangle = \sum_{k=1}^{n} \lambda_k v_k. \tag{A11}$$

Since $\lambda_k \geq 0$ and $v_k \geq 0$, each term $\lambda_k v_k \geq 0$. A sum of non-negative terms resulting in zero is only possible if $\lambda_k v_k = 0$ for all $k = 1, 2 \ldots n$. This implies that for each k, either $\lambda_k = 0$ or $v_k = 0$. However, since $\boldsymbol{\lambda} \neq 0$, there exists at least one index $\lambda_k > 0$. For such k, it must be that $v_k = 0$.

Next, examine the case $v_k = 0$. By definition

$$v_k = (\mathbf{R}^{\mathrm{T}}\mathbf{w})_k = \sum_{i=1}^{m} R_{ik} w_i. \tag{A12}$$

Since by assumption $R_{ik} \geq 0$ and $w_i \geq 0$, the only way $v_k = 0$ is if $R_{ik} w_i = 0$ for all i. But $w_i \geq 0$ with at least one $w_i > 0$, so $R_{ik} = 0$ for all i where $w_i > 0$.

This would imply that the k-th column of $\mathbf{R}$ is zero, but this leads to a contradiction as $\mathbf{R}$ is assumed to have non-trivial columns. Hence, the assumption that $\boldsymbol{\lambda} \geq 0$ must be false. The case $\boldsymbol{\lambda} \leq 0$ is completely symmetrical, and also leads to a contradiction. Thus, $\boldsymbol{\lambda}$ must have both positive and negative components to yield $\langle \boldsymbol{\lambda}, \mathbf{v} \rangle = 0$.

$\square$

6. Proof of Theorem II.4

Proof: Define

$$f_\alpha(\boldsymbol{\mu}) = \|\mathbf{y} - \mathbf{R}\boldsymbol{\mu}\|^2 + \alpha\|\boldsymbol{\mu}\|^2. \tag{A13}$$

1. Existence and uniqueness: We have

$$\nabla f_\alpha(\boldsymbol{\mu}) = -2\mathbf{R}^{\mathrm{T}}(\mathbf{y} - \mathbf{R}\boldsymbol{\mu}) + 2\alpha\boldsymbol{\mu}, \tag{A14}$$

$$\nabla^2 f_\alpha(\boldsymbol{\mu}) = 2(\mathbf{R}^{\mathrm{T}}\mathbf{R} + \alpha\mathbf{I}). \tag{A15}$$

For any nonzero $\mathbf{z}$,

$$\mathbf{z}^{\mathrm{T}}(\mathbf{R}^{\mathrm{T}}\mathbf{R} + \alpha\mathbf{I})\mathbf{z} = \|\mathbf{R}\mathbf{z}\|^2 + \alpha\|\mathbf{z}\|^2 > 0, \tag{A16}$$

so $\mathbf{R}^{\mathrm{T}}\mathbf{R} + \alpha\mathbf{I}$ is symmetric positive definite and invertible. The unique minimizer therefore satisfies

$$(\mathbf{R}^{\mathrm{T}}\mathbf{R} + \alpha\mathbf{I})\hat{\boldsymbol{\mu}}_\alpha = \mathbf{R}^{\mathrm{T}}\mathbf{y}, \tag{A17}$$

$$\hat{\boldsymbol{\mu}}_\alpha = (\mathbf{R}^{\mathrm{T}}\mathbf{R} + \alpha\mathbf{I})^{-1}\mathbf{R}^{\mathrm{T}}\mathbf{y}. \tag{A18}$$

2. Limiting case $\alpha \to 0^+$: Let $\mathbf{R} = \mathbf{U}\boldsymbol{\Sigma}\mathbf{V}^{\mathrm{T}}$ be a singular value decomposition with rank r and singular values $\sigma_1, \ldots, \sigma_r > 0$, and let $(\mathbf{u}_i)$, $(\mathbf{v}_i)$ denote the corresponding singular vectors. Then

$$\hat{\boldsymbol{\mu}}_\alpha = \mathbf{V}(\boldsymbol{\Sigma}^2 + \alpha\mathbf{I})^{-1}\boldsymbol{\Sigma}\,\mathbf{U}^{\mathrm{T}}\mathbf{y} = \sum_{i=1}^{r} \frac{\sigma_i}{\sigma_i^2 + \alpha}(\mathbf{u}_i^{\mathrm{T}}\mathbf{y})\,\mathbf{v}_i. \tag{A19}$$

Taking limits termwise, $\frac{\sigma_i}{\sigma_i^2+\alpha} \to 1/\sigma_i$ as $\alpha \to 0^+$, hence

$$\hat{\boldsymbol{\mu}}_\alpha \xrightarrow[\alpha\to 0^+]{} \sum_{i=1}^{r} \frac{1}{\sigma_i} (\mathbf{u}_i^{\mathrm{T}} \mathbf{y})\, \mathbf{v}_i = \mathbf{R}^\dagger \mathbf{y} =: \hat{\boldsymbol{\mu}}_{\mathrm{MNLS}}. \quad \text{(A20)}$$

Moreover,

$$\hat{\boldsymbol{\mu}}_\alpha - \hat{\boldsymbol{\mu}}_{\mathrm{MNLS}} = \sum_{i=1}^{r} \Big(\frac{\sigma_i}{\sigma_i^2+\alpha} - \frac{1}{\sigma_i} \Big) (\mathbf{u}_i^{\mathrm{T}} \mathbf{y})\, \mathbf{v}_i \quad \text{(A21)}$$

$$= -\sum_{i=1}^{r} \frac{\alpha}{\sigma_i(\sigma_i^2+\alpha)} (\mathbf{u}_i^{\mathrm{T}} \mathbf{y})\, \mathbf{v}_i, \quad \text{(A22)}$$

so, using $\frac{1}{\sigma_i^2+\alpha} \le \frac{1}{\sigma_i^2}$,

$$\left\| \hat{\boldsymbol{\mu}}_\alpha - \hat{\boldsymbol{\mu}}_{\mathrm{MNLS}} \right\| \le \alpha \Big(\sum_{i=1}^{r} \frac{(\mathbf{u}_i^{\mathrm{T}} \mathbf{y})^2}{\sigma_i^6} \Big)^{1/2} \xrightarrow[\alpha\to 0^+]{} 0. \quad \text{(A23)}$$

(3) Noise dampening under the additive model: Insert $\mathbf{y} = \mathbf{R}\boldsymbol{\mu} + \boldsymbol{\epsilon}$ into the solution map to obtain

$$\hat{\boldsymbol{\mu}}_\alpha(\mathbf{y}) = \hat{\boldsymbol{\mu}}_\alpha(\mathbf{R}\boldsymbol{\mu}) + (\mathbf{R}^{\mathrm{T}}\mathbf{R} + \alpha\mathbf{I})^{-1} \mathbf{R}^{\mathrm{T}} \boldsymbol{\epsilon}. \quad \text{(A24)}$$

With the SVD,

$$\hat{\boldsymbol{\mu}}_\alpha(\mathbf{R}\boldsymbol{\mu}) = \mathbf{V}(\boldsymbol{\Sigma}^2 + \alpha\mathbf{I})^{-1}\boldsymbol{\Sigma}^2 \mathbf{V}^{\mathrm{T}} \boldsymbol{\mu}$$

$$= \sum_{i=1}^{r} \frac{\sigma_i^2}{\sigma_i^2+\alpha} (\mathbf{v}_i^{\mathrm{T}} \boldsymbol{\mu})\, \mathbf{v}_i, \quad \text{(A25)}$$

such that

$$\hat{\boldsymbol{\mu}}_\alpha(\mathbf{y}) - \hat{\boldsymbol{\mu}}_\alpha(\mathbf{R}\boldsymbol{\mu}) = \sum_{i=1}^{r} \frac{\sigma_i}{\sigma_i^2+\alpha} (\mathbf{u}_i^{\mathrm{T}} \boldsymbol{\epsilon})\, \mathbf{v}_i. \quad \text{(A26)}$$

In particular, using the spectral norm and the elementary inequality

$$\frac{t}{t^2+\alpha} \le \frac{1}{2\sqrt{\alpha}} \qquad (\forall\, t \ge 0,\ \alpha > 0), \quad \text{(A27)}$$

we obtain the bound

$$\left\| \hat{\boldsymbol{\mu}}_\alpha(\mathbf{y}) - \hat{\boldsymbol{\mu}}_\alpha(\mathbf{R}\boldsymbol{\mu}) \right\| \le \frac{1}{2\sqrt{\alpha}} \|\boldsymbol{\epsilon}\|. \quad \text{(A28)}$$

In contrast, the unregularized least-squares map employs gains $1/\sigma_i$, which may be arbitrarily large when σ_i are small, hence regularization provides a smooth spectral cut-off and damps noise amplification.

$\square$
$\square$

7. Effects on non-negativity constraint on the feasible set

Proposition A.1 *Let $\mathbf{R} \in \mathbb{R}^{n\times n}$ satisfy $R_{ij} \ge 0$ for all i,j and have no zero columns, and suppose* $\mathrm{rank}(\mathbf{R}) =$

$r < n$ with $d = n - r > 0$. Let $\{\mathbf{k}_1, \ldots, \mathbf{k}_d\}$ be an orthonormal basis of $\ker(\mathbf{R})$ and set $K = [\mathbf{k}_1 \cdots \mathbf{k}_d] \in \mathbb{R}^{n\times d}$. Fix a particular vector $\boldsymbol{\mu}_0 \in \mathbb{R}^n$ with $\mathbf{R}\boldsymbol{\mu}_0 = \boldsymbol{\nu}$, and parametrize

$$\boldsymbol{\mu} = \boldsymbol{\mu}_0 + \boldsymbol{\lambda}, \qquad \boldsymbol{\lambda} = K\boldsymbol{\beta} = \sum_{i=1}^{d} \beta_i \mathbf{k}_i, \quad \boldsymbol{\beta} \in \mathbb{R}^d.$$

Impose the componentwise nonnegativity constraint $\boldsymbol{\mu} \ge 0$, i.e.

$$(\mu_0)_j + \sum_{i=1}^{d} \beta_i\, k_{i,j} \ge 0, \qquad j = 1, \ldots, n.$$

Let the feasible set be

$$\mathcal{B} = \{\, \boldsymbol{\beta} \in \mathbb{R}^d : \ \boldsymbol{\mu}_0 + K\boldsymbol{\beta} \ge 0 \,\}.$$

If $\mathcal{B} \ne \varnothing$, then:

1. *$\mathcal{B}$ is a convex polytope (a bounded convex polyhedron) in $\mathbb{R}^d$.*

2. *The set of feasible perturbations $\{\, \boldsymbol{\lambda} = K\boldsymbol{\beta} : \ \boldsymbol{\beta} \in \mathcal{B} \,\}$ is bounded. In particular, since the $\mathbf{k}_i$ are orthonormal, there exists $M < \infty$ such that*

$$\|\boldsymbol{\lambda}\| = \|\boldsymbol{\beta}\| \le M \qquad \text{for all } \boldsymbol{\beta} \in \mathcal{B}.$$

Consequently, the nonnegativity constraint reduces the affine family $\boldsymbol{\mu}_0 + \ker(\mathbf{R})$ to a bounded convex polytope of (physically meaningful) nonnegative solutions. Moreover, the boundedness in (1)–(2) follows from

$$\ker(\mathbf{R}) \cap \mathbb{R}_+^n = \{0\},$$

which holds under $R_{ij} \ge 0$ and the no–zero–columns assumption.

Proof: Convexity: $\mathcal{B}$ is an intersection of halfspaces, hence convex and polyhedral.

Recession cone: the recession directions of $\mathcal{B}$ are $\{\mathbf{d} \in \mathbb{R}^d : K\mathbf{d} \ge 0\}$. If there were a nonzero $\mathbf{d}$ with $K\mathbf{d} \ge 0$, then $\mathbf{v} := K\mathbf{d} \in \ker(\mathbf{R}) \cap \mathbb{R}_+^n$ would be nonzero. Under $R_{ij} \ge 0$ and no zero columns, any $\mathbf{v} \ge 0$ with $\mathbf{R}\mathbf{v} = 0$ must satisfy $\mathbf{v} = 0$ (each row has a nonnegative dot with $\mathbf{v}$ that can vanish only if $\mathbf{v}$ is supported on columns that are zero in that row; intersecting over all rows forces $\mathbf{v}$ to be supported on a column that is zero in every row, i.e. a zero column, which is excluded). Hence the recession cone is $\{0\}$ and $\mathcal{B}$ is bounded.

Bound on $\boldsymbol{\lambda}$: since $\boldsymbol{\lambda} = K\boldsymbol{\beta}$ with orthonormal columns of K, we have $\|\boldsymbol{\lambda}\| = \|\boldsymbol{\beta}\|$. Boundedness of $\mathcal{B}$ gives $\sup_{\boldsymbol{\beta}\in\mathcal{B}} \|\boldsymbol{\beta}\| < \infty$, yielding the stated M.

$\square$

8. Richardson's method

Previous work on unfolding the gamma-ray spectra in this work has primarily focused on using an iterative approach with a stopping criterion and a subtraction scheme to obtain estimates for the underlying spectrum, see Appendix H. As FICS in effect is a variant Richardson's iterative method [5], it warrants a deeper analysis of its robustness.

While the Richardson method is transparent, convergent, and fast for well-defined systems, the presence of noise and inclusion of background is problematic. As usual in iteration methods, a stopping criterion is used to regularize, and one is not forced to alter the problem via normal equations. However, as we will show, a stopping criterion is usually not enough for the Richardson method. For rank deficient and ill-conditioned systems, the situation only gets worse.

The Richardson iteration method for solving $\mathbf{y} = \mathbf{R}\boldsymbol{\mu}$ is defined by:

$$\boldsymbol{\mu}^{(k+1)} = \boldsymbol{\mu}^{(k)} + \omega(\mathbf{y} - \mathbf{R}\boldsymbol{\mu}^{(k)}), \qquad \text{(A29)}$$

where:

- $\boldsymbol{\mu}^{(k)}$ is the approximation of the solution at iteration k

- ω is the relaxation parameter (step-size)

We note that this formulation assumes *Gaussian* errors. However, our data model is Poisson-distributed, in which case the corresponding update step takes the form of a ratio rather than a difference For the Richardson method to have any possibility of converging, the choice of ω is crucial:

Theorem A.2 *For a square matrix* $\mathbf{R} \in \mathbb{R}^{n \times n}$ *of full rank with singular values* $\sigma_i > 0$, *the Richardson iteration converges to a unique solution for any initial guess* $\boldsymbol{\mu}^{(0)}$ *if and only if the relaxation parameter* ω *satisfies*

$$0 < \omega < \frac{2}{\sigma_{\max}}, \qquad \text{(A30)}$$

where $\sigma_{\max}$ *is the largest singular value of* $\mathbf{R}$.

To achieve the fastest convergence of the Richardson iteration, it is essential to select the optimal relaxation parameter ω within the convergence interval. The convergence rate is directly influenced by the spectral radius ρ of the iteration matrix $\mathbf{I} - \omega\mathbf{R}$,[29] and minimizing this leads to faster convergence. For a full-rank matrix, the optimal relaxation parameter is given by:

$$\omega_{\text{opt}} = \frac{2}{\sigma_{\min} + \sigma_{\max}}, \qquad \text{(A31)}$$

---

[29] This form is easily found by recasting Eq. (A29).

with corresponding spectral radius

$$\rho_{\text{opt}} = 1 - \omega_{\text{opt}}\sigma_{\min} = 1 - \frac{2}{1 + \text{Cond}(\mathbf{R})}. \qquad \text{(A32)}$$

As demonstrated above, even in well-defined systems where the matrix is of full column rank, noise amplification is inevitable for ill-conditioned matrices. The hope to prevent this is to use early stopping by monitoring the residual $\|\mathbf{y} - \mathbf{R}\boldsymbol{\mu}^{(k)}\|$ and stop iterations when it stops decreasing or starts increasing, indicating that further iterations may be fitting to noise. Unfortunately, in the Richardson method, early stopping is simply not enough

In the presence of noise, the Richardson iteration method amplifies noise if the system is ill-conditioned. Specifically:

1. If $\mathbf{R}$ is of full column rank, all singular values are $\sigma_i > 0$, but depending on the condition number, noise may be significantly amplified despite the residual norm decreasing.

2. If $\mathbf{R}$ is rank-deficient, it has zero singular values, leading to non-unique solutions. In this case, the Richardson iteration cannot converge to a unique solution, and noise is amplified in the directions corresponding to zero singular values. The method will produce non-unique solutions dominated by noise, and early stopping fails to prevent this issue.

While early stopping based on the residual norm is often used to regularize iterative methods, for Richardson iteration this is generally insufficient. In full-rank but ill-conditioned systems, the condition number is large, $\rho_{\text{opt}} \to 1$, which results in slow convergence and amplification of noise along directions associated with small singular values, even while the residual norm decreases. In rank-deficient systems, zero singular values cause non-uniqueness. The method cannot converge to a unique solution, and noise is projected into the null space of $\mathbf{R}$, producing solutions dominated by noise and often containing negative components.

These effects arise directly from the structure of the method. Since Richardson iteration has no built-in mechanism to constrain non-negativity or to regulate the influence of small or vanishing singular values, additional regularization would require modifications beyond early stopping. As a result, applying the method in practice requires considerable care.

Appendix B: Spectral complexity profile measure

To quantify local variations in the target spectrum $\boldsymbol{\eta}$ relative to the energy-dependent detector resolution $\sigma_\gamma(E_\gamma)$, we introduce the scale-invariant smoothness measure

$$s(E_\gamma) = \sqrt{\left[\frac{1}{\sigma_\gamma(E_\gamma)}\frac{d\boldsymbol{\eta}}{dE_\gamma}\right]^2 + \left[\frac{1}{\sigma_\gamma^2(E_\gamma)}\frac{d^2\boldsymbol{\eta}}{dE_\gamma^2}\right]^2}.$$

Large values of $s(E_\gamma)$ mark sharp structure or rapid changes that exceed the local Gaussian resolution. To probe piecewise smoothness we smooth $s(E_\gamma)$ with a Gaussian kernel of bandwidth $w\,\sigma_\gamma(E_\gamma)$,

$$s_w(E_\gamma) \;=\; \frac{\sum_{E_k} \mathbf{G}_\gamma^w(E_\gamma, E_k)\, s(E_k)}{\sum_{E_k} \mathbf{G}_\gamma^w(E_\gamma, E_k)},$$

where $\mathbf{G}_\gamma^w(E_\gamma, E_k)$ is the smearing kernel of Eq. (59) with $\sigma_\gamma \mapsto w\sigma_\gamma$. A larger w reduces noise at the cost of resolving fine structure. Evaluating $s_w(E_\gamma)$ on a mesh $\{E_k\}_{k=0}^M$ gives the set $S = \{s_w(E_k)\}_{k=0}^M$. Overall complexity is summarized by

$$s_{\mathrm{max/med}} \;=\; \frac{\max_k S_k}{\mathrm{median}_k\, S_k}, \qquad s_{\mathrm{CV}} \;=\; \frac{\sqrt{\mathrm{Var}[S]}}{\mathrm{mean}\, S}\,.$$

The ratio $s_{\mathrm{max/med}}$ highlights the single sharpest feature relative to the typical one. The coefficient of variation s_{CV} measures how evenly smoothness is distributed. Combining these metrics suggests three heuristic classes, shown in Fig. 14. :

- **Smooth**: low $s_{\mathrm{max/med}}$, low s_{CV}. Uniformly smooth.

- **Pseudo-smooth**: high $s_{\mathrm{max/med}}$, low s_{CV}. Mostly smooth with isolated sharp features.

- **Non-smooth**: high $s_{\mathrm{max/med}}$, high s_{CV}. Complex structure with variable smoothness.

The fourth logical quadrant, low $s_{\mathrm{max/med}}$ and high s_{CV}, is theoretically possible but has not been observed. Such spectra would also be labeled *non-smooth*.

No fixed numerical cutoffs are supplied. The scheme is intended as a qualitative aid when tuning global or locally adaptive regularization methods.

Appendix C: Convergence conditions

The qualitative result of the unfolding was found to be independent of the specific gradient descent optimizer used. However, the rate of convergence can be highly dependent on the particular spectrum; an optimizer with well-tuned hyperparameters may converge rapidly on one spectrum but be orders of magnitude slower on another, even within the same dataset.[30] In practice, the

_____

[30] The reason for this behavior is related to the spectral radius. Optimizers with modifications that, in practice, result in an effective step size larger than the spectral radius tend to experience unstable convergence, or even divergence. On the other hand, if the effective step size is too small compared to the spectral radius, convergence becomes slow. Optimizers that only have minor modifications compared to standard gradient descent typically do not encounter this issue.

NAdam [21] optimizer, a variant of Adam [22] that incorporates Nesterov Momentum, was found to perform efficiently across all tested spectra when using a step size $d\tau$, set within the convergence interval:

$$0 < d\tau < 1/L \tag{C1}$$

where L is the Lipschitz constant of the gradient of the loss function. However, calculating L directly is challenging as it amounts to calculating the Hessian, which in our case is infeasible. If we instead make the approximation to a quadratic loss, the Lipschitz constant is given by the maximum singular value of the relevant response, $L = 2\sigma_{\mathrm{max}}^2$. A complication occurs when we introduce a regularization term as this changes the loss landscape. Adding a regularization can lead to a larger Lipschitz constant, as the regularization term can completely dominate the behavior of the loss function. Effectively, this leads to a shrinking of the convergence interval as the upper bound is shifted and Eq. (C1) with $L = 2\sigma_{\mathrm{max}}^2$ can no longer guarantee convergence.

When adding a regularization term to the loss function the Lipschitz constant takes the form

$$L = L_\ell + \alpha L_\Omega\,. \tag{C2}$$

While these are possible to calculate in theory, they are not available in practice. For the special case of Tikhonov regularization with a quadratic loss function, the Lipschitz constant takes the form $L = 2\sigma_{\mathrm{max}}^2 + \alpha$, serving as a new upper bound to achieve convergence. For the regularization schemes we use, no simple analytical expression is available. In practice, a sufficiently good step length can be found by manually tuning the parameter until the loss curve is sufficiently steep without signs of divergence.

Appendix D: Marginal and simultaneous confidence intervals

The Monte Carlo resampling method (Sec. VI) generates an ensemble of unfolded solutions $\boldsymbol{\eta}$, which characterizes the variability inherent in the RMLE method. Because this distribution typically exhibits non-negligible higher-order moments, summarizing the ensemble inevitably discards important information. Consequently, for subsequent steps in the Oslo Method, it is strongly recommended to propagate the full ensemble rather than any summary statistic.

However, summaries—particularly confidence intervals (CIs)—can offer intuitive measures of uncertainty. One must then distinguish between *marginal* and *simultaneous* confidence intervals.

A **marginal confidence interval** is constructed independently for each bin from the ensemble. Common approaches include the percentile method or bias-corrected and accelerated (BCa) intervals. While simple to compute, marginal intervals consider each bin in isolation

and thus ignore correlations between bins. As a result, marginal intervals are inadequate for global inference tasks, such as testing whether a peak significantly differs from zero or comparing entire unfolded solutions $\hat{\boldsymbol{\eta}}^*$ to $\hat{\boldsymbol{\eta}}'^*$.

In contrast, a **simultaneous confidence interval** accounts for bin-to-bin correlations and provides global coverage. Specifically, a simultaneous CI describes an interval or region that contains the entire true function $\boldsymbol{\eta}$ with a given confidence level. Formally, a simultaneous interval ensures that, asymptotically, at least a fraction[31] $1 - \alpha$ of the repeated samples will contain the complete function.

The simultaneous CI is inherently high-dimensional, corresponding geometrically to an N-dimensional confidence ellipsoid enclosing a proportion $1 - \alpha$ of the probability mass. Compared to marginal intervals, simultaneous CI are always wider. Practical methods to derive simultaneous CIs typically reduce this region into interpretable intervals, using methods such as:

Supremum norm intervals: Computed by evaluating the maximum absolute deviation across bins and determining a uniform margin that simultaneously covers all bins. This approach yields conservative intervals.

Studentized supremum norm intervals: Similar to the supremum norm method, but deviations are standardized by local variance estimates. This results in tighter intervals that better reflect spatially varying uncertainty.

Bonferroni intervals: Constructed by adjusting the confidence level of each marginal interval to $1 - \frac{\alpha}{N}$, ensuring that the global coverage probability is at least $1 - \alpha$ via the Bonferroni correction.

In practice, we find that the studentized supremum norm and the Bonferroni-based simultaneous confidence intervals yielded nearly identical results. Unless otherwise stated, all confidence intervals presented in this work are marginal. Although these are easier to compute and interpret, it is important to exercise caution when drawing global inferences from marginal intervals, as they do not account for bin-to-bin correlations. Researchers should be mindful of these limitations when interpreting the results.

Appendix E: Coverage

For each physical bin i, we denote by η_i the (unknown) true intensity. If a confidence interval CI_i is constructed

_____

[31] Here, α denotes the significance level, not to be confused with a regularization parameter.

for that bin, the *coverage probability*

$$p_i = \Pr(\eta_i \in \mathrm{CI}_i) \qquad \text{(E1)}$$

quantifies how often, in repeated experiments, the interval contains the true value. The *confidence level* is the prescribed coverage probability that we want our constructed confidence interval to have.

The *empirical* or *actual* coverage probability of the CI can be estimated using Monte Carlo simulations. Given a fixed underlying spectrum $\boldsymbol{\eta}$, we simulate M independent reconstructions, each producing a confidence interval $\mathrm{CI}_i^{(m)}$ for bin i. For each simulation, we define a Bernoulli random variable

$$I_i^{(m)} = \mathbb{1}\{\eta_i \in \mathrm{CI}_i^{(m)}\}, \qquad \text{(E2)}$$

which equals one if the interval contains the true value and zero otherwise. The estimate for the actual coverage probability is then given by

$$\hat{p}_i = \frac{1}{M} \sum_{m=1}^{M} I_i^{(m)}, \qquad \mathbb{E}[\hat{p}_i] = p_i. \qquad \text{(E3)}$$

Since $I_i^{(m)}$ is Bernoulli distributed, the standard error of $\hat{p}_i$ is

$$\mathrm{SE}(\hat{p}_i) = \sqrt{\frac{\hat{p}_i(1 - \hat{p}_i)}{M}}. \qquad \text{(E4)}$$

Appendix F: Experimental data used for the Oslo Method

The aim of the Oslo Method is to obtain nuclear level densities and gamma-ray transmission coefficients. The method consists of five main steps:

1. Use experimental data to construct the $\mathbf{P}\,(E_{\mathrm{in}}, E_\gamma)$ matrix of γ-ray spectra for each initial excitation-energy bin E_{in}.

2. Unfold the $(E_{\mathrm{in}}, E_\gamma)$ matrix using response functions of the γ-detector array to obtain a spectrum of full-energy peaks, the *all-generation* matrix. This unfolding has usually been done with the method described in Ref. [1].

3. Extract the distribution of the *first-generation* gamma rays for each initial excitation-energy bin through an iterative subtraction technique, thus obtaining the first-generation matrix $P(E_{\mathrm{in}}, E_\gamma)$ [2].

4. Decompose the first-generation matrix into two vectors, namely, the nuclear level density $\rho(E_{\mathrm{in}} - E_\gamma)$ and the gamma-ray transmission coefficient $\mathcal{T}(E_\gamma)$, under the ansatz that the first-generation matrix can be written as $P(E_{\mathrm{in}}, E_\gamma) \propto \rho(E_{\mathrm{in}} - E_\gamma) \times \mathcal{T}(E_\gamma)$ [3].
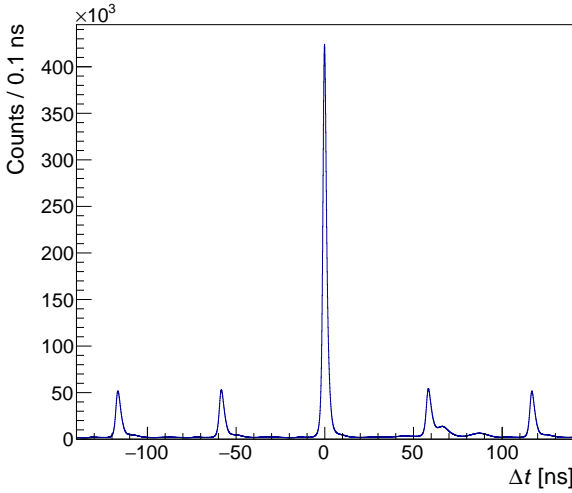
FIG. 31: The time spectrum for all 30 OSCAR detectors from the $^{28}\text{Si}(p, p'\gamma)$ reaction. The large peak at 0 ns is gated for the total counts, and the lower peaks for the background.

5. Normalize $\rho(E_{\text{in}} - E_\gamma)$ and $\mathcal{T}(E_\gamma)$ to auxiliary data [3, 23].

This work focuses on step 2, i.e., the unfolding of complex gamma-ray spectra. But here we first briefly describe the way the experimental data are obtained (step 1).

A large variety of nuclear reactions can be used for the Oslo Method. To reach high excitation energies in the nuclei of interest, the following reactions have been used:

- Charged-particle reactions such as $(^3\text{He},\alpha)$, (d,p) and (p,p') in normal kinematics; see, e.g., Refs. [18, 24, 25].

- The (d,p) reaction in inverse-kinematics, e.g., Ref. [26].

- β^- decay, for *the beta-Oslo Method*, e.g., Refs. [27– 29].

We remark that for the beta-Oslo Method, the initial excitation energy is inferred from total absorption spectrometry, which poses additional challenges for the unfolding. For the purpose of discrete spectroscopy using a total absorption spectrometer like the SuN detector [30], machine learning has very recently been applied to such data sets [31]. Moreover, a wide range of gamma-ray detectors have been utilized for applications of the Oslo Method, such as NaI:Tl scintillators (CACTUS [6], SuN [30]), LaBr$_3$:Ce scintillators (HECTOR$^+$ [32], OS-CAR [13]), and high-purity Ge detectors with anti-Compton shields such as STARLiTeR [33]. As a consequence, there is large diversity of gamma-ray spectra from different experiments and nuclei.

In this work we focus on experimental data for which the initial excitation energy is determined from information independent from the gamma rays, i.e., from the

charged-particle ejectiles. Here we use a calibration run on natural Si as an example, using a proton beam of 16 MeV. As natural Si mainly consists of ^{28}Si (92%), the data set is dominated by the $^{28}\text{Si}(p, p'\gamma)^{28}\text{Si}$ reaction. This data set was taken with OSCAR [13] for gamma-ray detection and the Silicon Ring (SiRi) [11] for proton detection, with SiRi in backward angles (126–140° with respect to the beam direction), and using digital electronics for the data acquisition where all events are time stamped (XiA Pixie-16 digitizers, 14-bit and 500 MHz sample rate for OSCAR and 16-bit and 250 MHz sample rate for SiRi). SiRi consists of eight ΔE–E telescope modules, with a thin front detector of ≈ 130 μ that is segmented into eight strips, which cover $\approx 2°$ each. The front detector is accompanied by a thick E detector of thickness ≈ 1550 μm, where the protons are stopped. OSCAR is built of 30 large-volume LaBr$_3$:Ce detectors distributed on a spherical frame.

In Fig. 31, the time spectrum of the ^{28}Si data set is shown. The reference time (the "start") is the proton detection in SiRi, while the "stop" is the signal in one of the OSCAR detectors. The figure shows the summed time spectrum, i.e., the time spectrum for all the 30 OS-CAR detectors. The prompt peak has a time difference between the start and stop signals of zero nanoseconds and has a resolution of ≈ 2.4 ns FWHM. Due to the pulsed beam from the cyclotron, other peaks show up in the time spectrum, for which the gamma was detected before the proton, such as the peak at ≈ -59 ns, or after the proton, such as the peak at ≈ 59 ns. These peaks are used to estimate the background contribution (random background plus beam-induced background) in the prompt peak, so that the spectra are incremented when the time difference between the ΔE and OSCAR detector is within $\Delta t = [-5.0, 5.0]$ ns and decremented if $\Delta t = [-62, -52]$ ns. The resulting initial excitation energy versus gamma-ray energy matrix of ^{28}Si with the gate on the prompt time peak is shown in Fig. 32a. Here, the detected proton energy has been converted to initial excitation energy in ^{28}Si using the reaction kinematics. Correspondingly, the matrix generated with the gate on the random time peak is shown in Fig. 32b.

To better visualize the background contribution, we have made projections of both the prompt and background gamma-ray spectra for two different initial-excitation-energy regions as marked by the black lines in Fig. 32a and b, and shown in Fig. 32c and d, respectively. The gamma-ray spectrum for the initial-excitation-energy gate corresponding to the first 2^+ level in ^{28}Si (Fig. 32c) clearly shows the 1779-keV line, which is the full-energy peak corresponding to the decay to the ground state. We observe that the background spectrum contains many of the same features as the prompt one, however in the gamma-energy region of interest, i.e., the region up to about the maximum initial excitation energy in the gate, the background has significantly less counts than the prompt gamma-ray spectrum, about a factor of 10 or so. This is what is expected from the time spec-
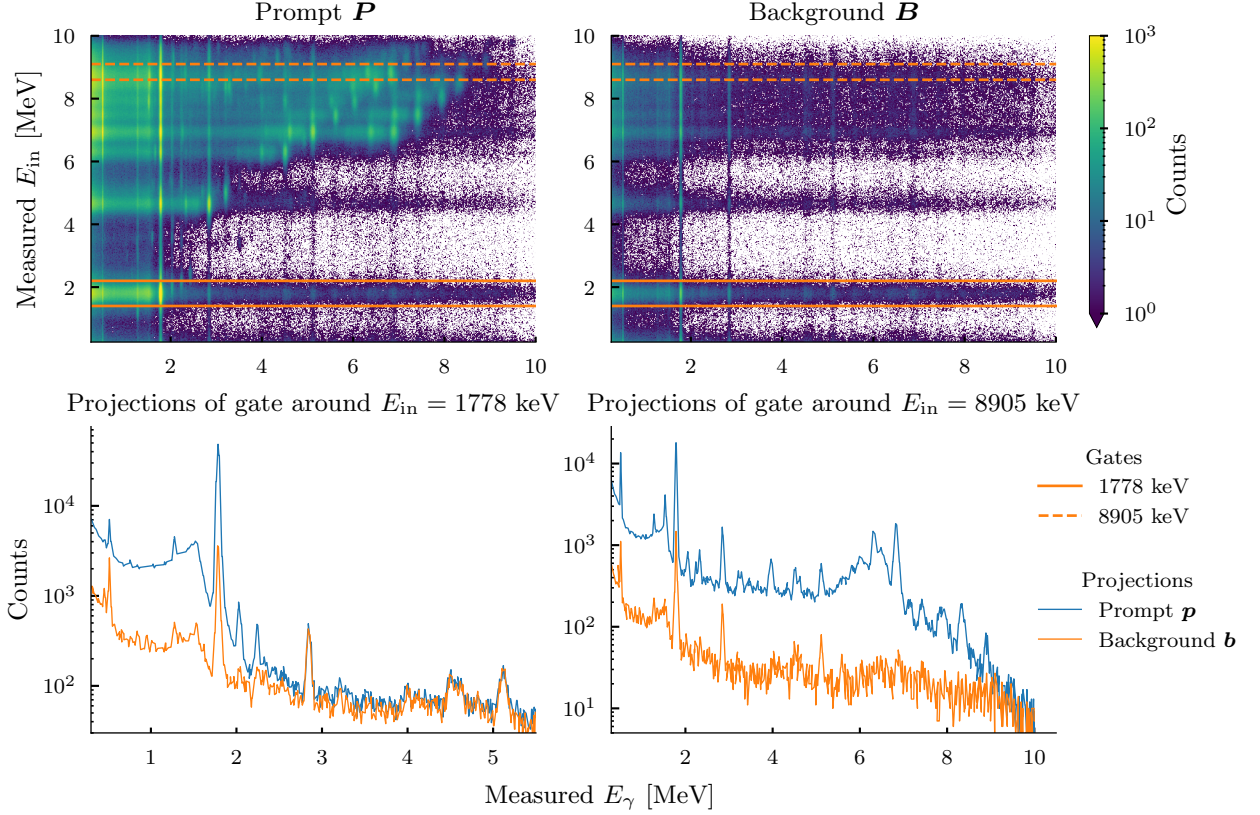
FIG. 32: Data from a calibration run using the ^{28}Si$(p, p'\gamma)$ reaction, where gamma rays were measured with OSCAR. (Top left) Gates on prompt events; (top right) Gates on background events; (bottom left) gamma spectra for gates on prompt and background events for $E_{in} \approx 1778$ keV; (bottom right) gamma spectra for gates on prompt and background events for $E_{in} \approx 8900$ keV.

trum in Fig. 31. For the spectra obtained by gating on $E_{in} \approx 8905$ keV, the same behavior is seen.

Before 2019 and the commissioning of OSCAR, the CACTUS array was the workhorse in the nuclear physics experiments at the Oslo Cyclotron Laboratory (OCL). Also, the data acquisition system was analogue, with a "master gate" to control the event building. This master gate was a logic signal generated either from one of the 64 ΔE detectors giving a signal (an OR signal of all the 64 strips), or taking the overlap of the ΔE and E detectors requiring both a ΔE strip and an E detector giving signals, or just using an OR of the eight E detectors. This same master gate was used as the "start" in the time-to-digital converters for the NaI:Tl detectors of CACTUS.

An example of a CACTUS experiment with poor statistics is the ^{186}W$(\alpha, \alpha'\gamma)$ data shown in Fig. 33 and published in Ref. [34]. In this experiment, the start was generated from the E detectors only, and as they are quite thick detectors, the timing properties are not as good as for the thin ΔE detectors. In addition, CACTUS had a significantly worse time resolution than OSCAR, as signals from the NaI:Tl crystals have a slower rise time than the LaBr$_3$:Ce crystals. Due to the worse time res-

olution, the time window set on the prompt events was quite broad, $\Delta t = [-21.6, 21.6]$ ns, and so the gate on the randoms was broad as well, $[110.4, 153.6]$ ns.

The prompt (E_{in}, E_γ) events for the ^{186}W$(\alpha, \alpha'\gamma)$ reaction are shown in Fig. 33a, and the background matrix is shown in Fig. 33b. We observe that the background component is quite reasonable also in this case for the lower initial excitation energies, as seen from the projection around the second 2^+ level at 737.97 keV in Fig. 33c. However, as shown in Fig. 33d for the gate at higher initial excitation energies around 7 MeV, the background component becomes comparable to the prompt spectrum for $E_\gamma \approx 5.5$ MeV and above. For such cases, the unfolding might become even more challenging, especially for methods where the background is not input to the unfolding but where the unfolding is performed directly on the background-subtracted spectra. Inevitably, the low signal-to-noise ratio will lead to large uncertainties in the resulting unfolded spectrum. The noise in the data is one of the major complicating factors for the unfolding problem, as discussed in this work.
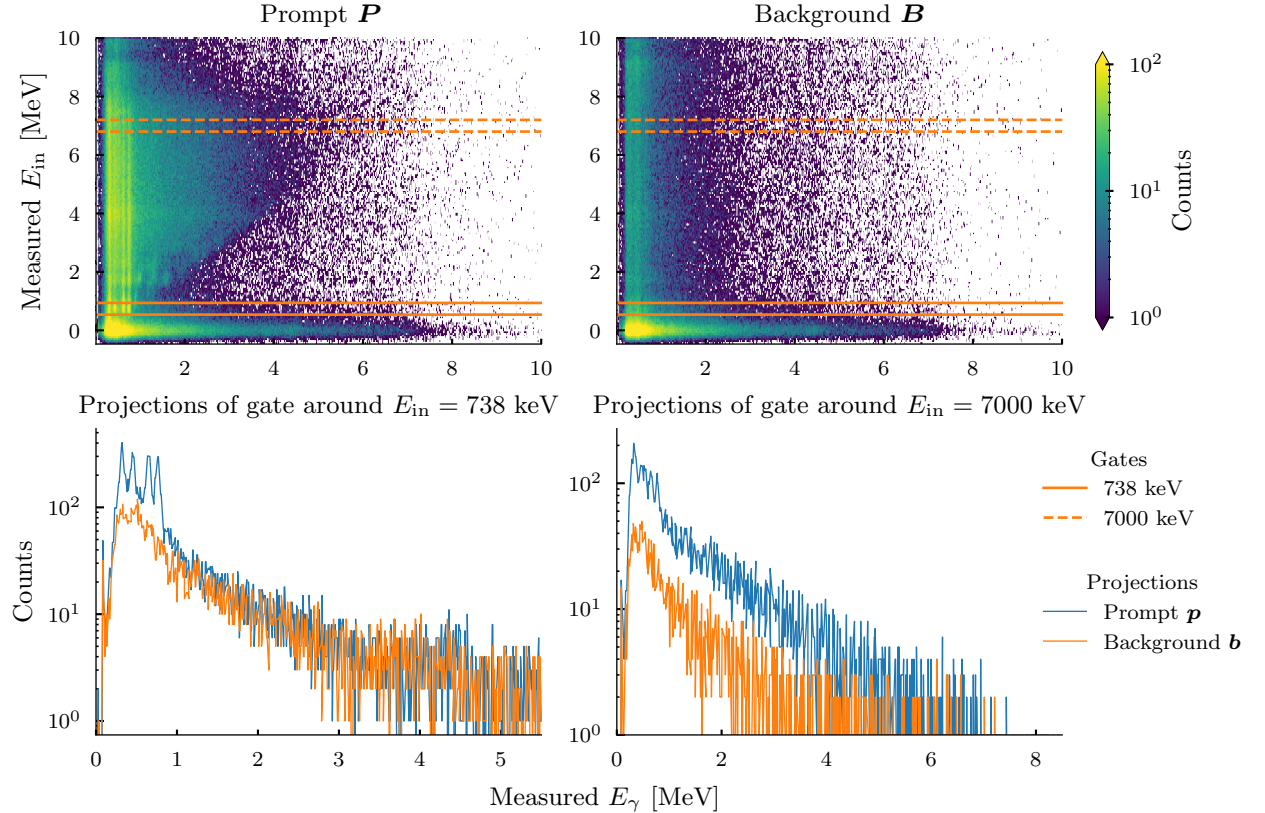
FIG. 33: Data from the ^{186}W$(\alpha, \alpha'\gamma)$ reaction published in Ref. [34], where gamma rays were measured with CACTUS. (Top left) Gates on prompt events; (top right) Gates on background events; (bottom left) gamma spectra for gates on prompt and background events for $E_{\mathrm{in}} \approx 738$ keV; (bottom right) gamma spectra for gates on prompt and background events for $E_{\mathrm{in}} \approx 7000$ keV.

Appendix G: Regularization systematics

We benchmark the RMLE method on both low- and high-complexity spectra, varying total number of counts, and applying a range of regularization types and strengths. While synthetic discrete spectra are trivial to construct, realistic quasi-continuous or high-complexity spectra require gamma-cascade simulations using codes such as RAINIER[35] or DICEBOX[36]. A ^{120}Sn-like spectrum is used as an example of a high-complexity spectrum, while a ^{166}Ho-like spectrum represents a quasi-continuous spectrum. Although the simulations are not optimized for realism, they adequately support the analysis presented here. For clarity of presentation we unfold only one-dimensional spectra.

The Kullback–Leibler (KL) divergence $D_{\mathrm{KL}}(\hat{\boldsymbol{\eta}}||\boldsymbol{\eta})$ is a natural choice for evaluating the discrepancy between the fitted distribution $\hat{\boldsymbol{\eta}}$ and the actual distribution $\boldsymbol{\eta}$, but it becomes numerically unstable when either distribution contain vanishingly small elements. As a robust alternative we employ the first-order Wasserstein (earth-mover) distance[37, 38], denoted $W_1(\hat{\boldsymbol{\eta}}, \boldsymbol{\eta})$, which measures the minimum "work" required to transform one distribution into the other. When comparing distributions with different total counts, normalization is applied to ensure an unbiased comparison.

A practical strategy for selecting the regularization strength α is the *L-curve* diagnostic. An L-curve plots the residual (fidelity) cost — here $D_{\mathrm{KL}}(\hat{\boldsymbol{\nu}}||\mathbf{y})$ — on the abscissa and the regularization cost on the ordinate for a sweep of α. Ideally, the resulting curve forms an L-shape, where the point of maximum curvature — the corner of the L — balances data fidelity and solution regularization.

Because our data is simulated, $\boldsymbol{\eta}$ is known *a priori*. This allows us to validate the L-curve diagnostic by computing independent "cost curves" using $W_1(\hat{\boldsymbol{\eta}}, \boldsymbol{\eta})$ for the residual. In an ideal scenario the minimum residual cost coincides with the L-curve corner.

Figure 34(a, b) thus confirm that, for a low-complexity peak with sparsity regularization, the L-curve correctly pinpoints the optimal sparsity regularization strength ($\alpha \approx 10^2$ in this example).

For the continuous ^{166}Ho-like spectrum with smoothness regularization, the curvature criterion again selects the optimal α as the cost minimum, shown in Fig. 34(c, d). The L-curve lacks an obvious elbow, but the point
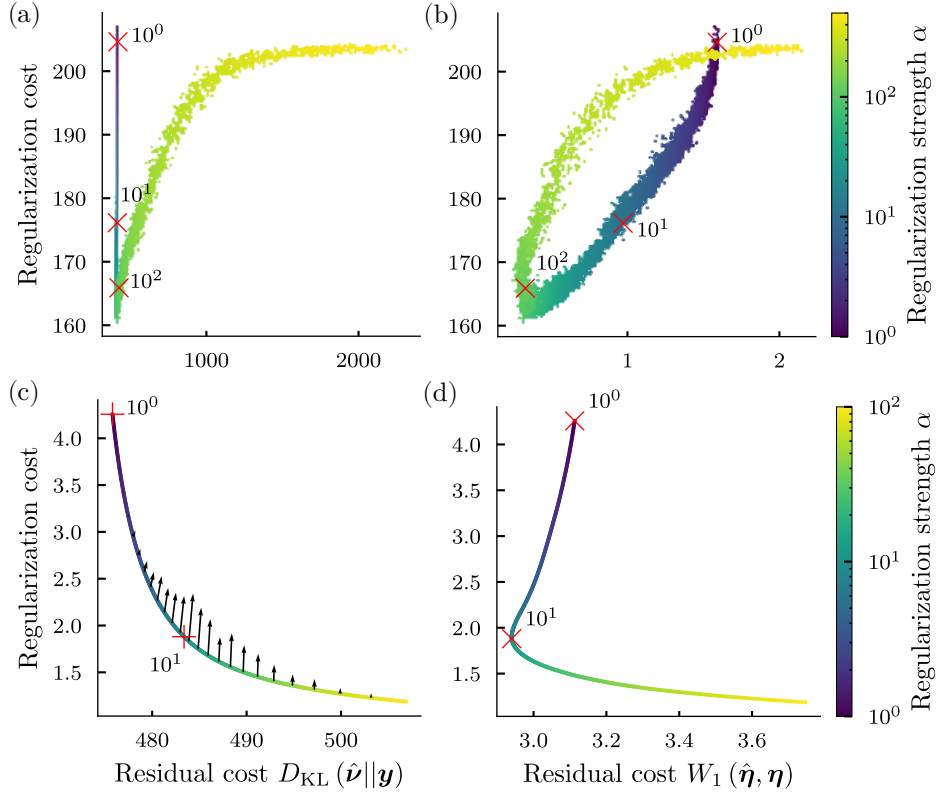
FIG. 34: (a) L-curve for a single-peak spectrum with sparsity penalty. A pronounced minimum occurs near $\alpha \approx 10^2$, and the scattered shape reflects a non-convex loss landscape. (b) Corresponding Wasserstein cost curve for a peaked spectrum; the optimal value $\alpha \approx 10^2$ aligns with the L-curve elbow in panel (a). (c) L-curve for a ^{166}Ho-like spectrum with smoothness penalty, whose curvature peaks near $\alpha \approx 10$ without a sharp corner. (d) Wasserstein cost curve for the ^{166}Ho case; its minimum near $\alpha \approx 10$ coincides with the curvature peak in panel (c).

of largest curvature still signals the best regularization strength.

High-complexity spectra—such as the ^{120}Sn benchmark—behave differently. As shown in Fig. 35(a,c), their L-curves may contain inflection-like features that could be mistaken for corners. However, the cost curves in Figure 35(b,d) demonstrate that these features do not correspond to true minima. In other words, the L-curve criterion fails, and regularization offers no clear benefit.

Finally, Figure 36 explores how counting statistics modulates the sensitivity to regularization. With fewer counts the residual cost exhibits a narrow trough, making the solution acutely dependent on α. As statistics improve, the trough widens and shallows, implying that the data themselves begin to dominate the optimization and tolerate stronger penalties without a loss of fidelity. The situation is analogous for ^{166}Ho with smoothness regularization.

For spectra of low spectral complexity, the L-curve—interpreted via its point of maximum curvature—is a reliable, data-driven tool for selecting the regularization strength, and its recommendation is corroborated by the Wasserstein cost curves. In contrast, high complexity spectra lack a single optimal penalty parameter; any

fixed-value regularization either over- or under-constrains the solution. Moreover, increased counting statistics systematically reduce the sensitivity of the reconstruction to regularization choices, highlighting the practical value of high-statistical-quality data when unfolding complex gamma-spectra.
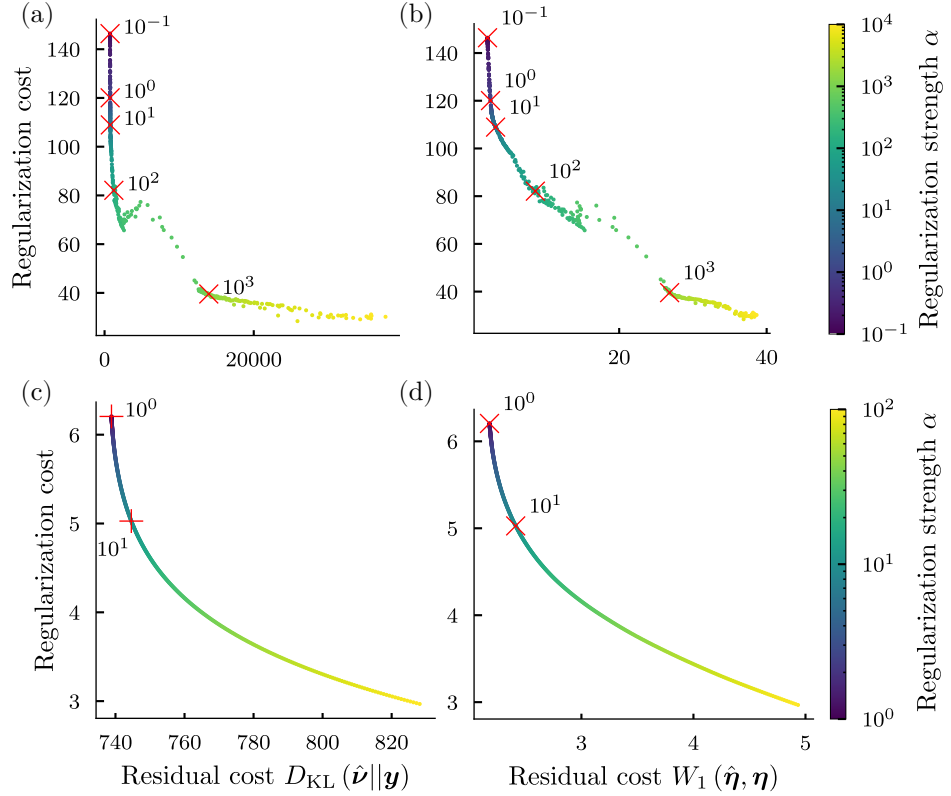
FIG. 35: (a) L-curve with sparsity penalty. A superficial bend appears near $\alpha \approx 3 \times 10^{2}$, but this is a false optimum, see panel (b). (b) Cost curve for sparsity penalty. Residual increases monotonically with α, confirming the absence of a valid optimum. (c) L-curve with smoothness penalty. The curvature is nearly monotonic; no clear corner is present. (d) Cost curve for smoothness penalty. Residual worsens steadily; no suitable regularization strength is found. Panels (a)–(d) thus show L-curves (left) and corresponding cost curves (right) for a high-complexity ^{120}Sn spectrum under sparsity (top row) and smoothness (bottom row) regularization. While the L-curves suggest possible optima, the cost curves reveal that neither sparsity nor smoothness regularization yields a meaningful trade-off between residual and penalty.
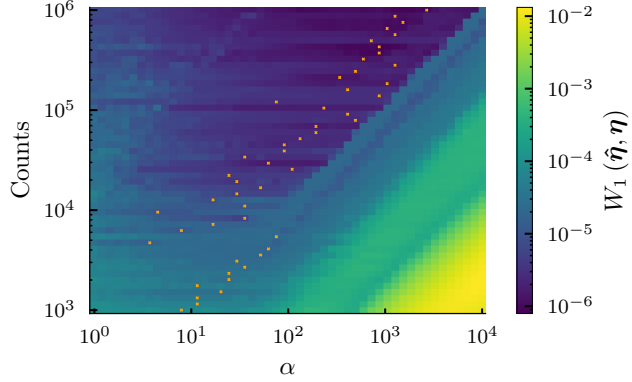
FIG. 36: Residual cost $W_1(\hat{\boldsymbol{\eta}}, \boldsymbol{\eta})$ for a single-peak spectrum as a joint function of the total number of detected counts (vertical axis) and the sparsity strength α (horizontal axis). At low statistics the landscape is steep: the optima (orange dots) are narrowly confined and highly sensitive to α. As the number of counts increases the surface flattens, indicating that data statistics progressively outweigh the influence of the penalty term.

Appendix H: FICS

The *Folding Iteration with Compton Subtraction* method (FICS), first described in [1], consists of an iterative component that solves the inverse problem, followed by a correction to the unfolded solution called *Compton subtraction*. The complete method is summarized in Algorithm 3. The iterative component implements Richardson's method for Gaussian error, with constant step size $\omega = 1$, and early stopping. For a response matrix $\mathbf{R}$, the update to the current solution $\hat{\boldsymbol{u}}^{(k)}$ is given by

$$\hat{\boldsymbol{u}}^{(k+1)} = \hat{\boldsymbol{u}}^{(k)} + \boldsymbol{y} - \mathbf{R}\hat{\boldsymbol{u}}^{(k)}, \tag{H1}$$

which is identical to Eq. (A29). Guttormsen et al. [1] observed that the solution diverged, necessitating early stopping. Furthermore, they noted that the solution contained spurious fluctuations, requiring the iterations to be stopped before these fluctuations dominated the spectrum. The stopping criteria (not detailed in [1]) combine two terms: the residuals between the folded solution $\hat{\boldsymbol{f}}^{(k)} = \mathbf{R}\hat{\boldsymbol{u}}^{(k)}$ and the data $\boldsymbol{y}$, and a cost term based on the fluctuations in $\hat{\boldsymbol{u}}^{(k)}$. The residual cost is expressed as a χ^2:

$$c_{\text{res}}^{(k)} = \sum_i \frac{\left(y_i - f_i^{(k)}\right)^2}{|y_i|}. \tag{H2}$$

The fluctuations cost uses the ℓ_1 norm of the difference between the solution $\hat{\boldsymbol{u}}^{(k)}$ and its smoothed version under a smoothing operator S:

$$c_{\text{fluct}}^{(k)} = \sum_i \left| \hat{u}_i^{(k)} - S\left(\hat{u}^{(k)}\right)_i \right|. \tag{H3}$$

The total cost combines these terms with a weighting factor:

$$c_{\text{tot}}^{(k)} = \alpha c_{\text{res}}^{(k)} + (1-\alpha)c_{\text{fluct}}^{(k)} \tag{H4}$$

where $0 \leq \alpha \leq 1$. The iteration terminates when $c_{\text{tot}}^{(k+1)} > c_{\text{tot}}^k$.

Guttormsen et. al. [1] recognized that this scheme remained insufficient, as the solution continued to exhibit spurious fluctuations. Specifically, they observed that the fluctuations in $\hat{\boldsymbol{u}}^{(k)}$ did not correspond to those in the data $\boldsymbol{y}$. The Compton subtraction method was developed to address this discrepancy. The method relies on physical assumptions about the Compton component, particularly its smoothness: we expect this component to be free of fluctuations. To derive the method, recall from Eq. (58) that the discrete matrix $\mathbf{D}$ comprises the following discrete components:

$$\mathbf{D} = \mathbf{P}_{\text{f}} + \mathbf{P}_{\text{s}} + \mathbf{P}_{\text{d}} + \mathbf{P}_{\text{a}} + \mathbf{P}_{\text{c}}. \tag{H5}$$

Let $\mathbf{P}_{\text{p}} = \mathbf{P}_{\text{s}} + \mathbf{P}_{\text{d}} + \mathbf{P}_{\text{a}}$ denote the discrete peaks excluding the full energy peak (corresponding to $w(i)$

in [1]). The data $\boldsymbol{y}$ can then be expressed in terms of $\boldsymbol{x}$ as

$$\boldsymbol{y} = \mathbf{G}_\lambda \mathbf{D}\boldsymbol{x} = \mathbf{G}_\lambda\left(\mathbf{P}_{\text{f}} + \mathbf{P}\text{p} + \mathbf{P}_{\text{c}}\right)\boldsymbol{x} = \boldsymbol{f}_{\text{f}} + \boldsymbol{f}_{\text{p}} + \boldsymbol{f}_{\text{c}}, \tag{H6}$$

for some smearing operator $\mathbf{G}_\lambda$. From $\hat{\boldsymbol{u}}^{(k)}$, we derive an estimate $\hat{\boldsymbol{f}}_{\text{c}}$ of the Compton component by rearranging Eq. (H6) (corresponding to Eq. (17) in [1]):

$$\hat{\boldsymbol{f}}_{\text{c}} = \boldsymbol{y} - \underbrace{\mathbf{G}_\lambda\mathbf{P}_{\text{f}}\hat{\boldsymbol{u}}^{(k)}}_{\text{Smeared full energy peaks}} - \underbrace{\mathbf{G}_\lambda\mathbf{P}_{\text{p}}\hat{\boldsymbol{u}}^{(k)}}_{\text{Smeared discrete peaks}}. \tag{H7}$$

We then modify $\hat{\boldsymbol{f}}_{\text{c}}$ based on its expected physical properties by applying a smoothing operator S, attempting to better approximate the true $\boldsymbol{f}_{\text{c}}$. The final solution is obtained by subtracting both the smoothed Compton estimate and the discrete peak estimate from the data:

$$\mathbf{G}_\lambda\mathbf{P}_{\text{f}}\hat{\boldsymbol{u}}_{\text{sol}} := \boldsymbol{y} - \underbrace{S\left(\hat{\boldsymbol{f}}_{\text{c}}\right)}_{\text{Smoothed Compton}} - \underbrace{\mathbf{G}_\lambda\mathbf{P}_{\text{p}}\hat{\boldsymbol{u}}^{(k)}}_{\text{Smeared discrete peaks}}. \tag{H8}$$

This formulation differs from Eq. (18) in [1] due to two fundamental issues. The first stems from an error propagated from [14]. Sükösd et al. correctly identified that the response matrix is ill-conditioned, primarily due to Gaussian smoothing, necessitating regularization. They attempted to unfold to an η-space with higher resolution than the experimental spectrum. However, as demonstrated in Sec. IV, this is impossible without strong and robust regularization.

While Süksöd et al. observed oscillations when unfolding at full resolution σ_γ, they found that unfolding with $\sigma = 0.5\sigma_\gamma$ produced optimal results, based on analysis of a synthetic spectrum with discrete peaks. However, unfolding discrete peaks implicitly incorporates prior information about the solution's discrete nature. This additional prior information serves as a regularizer, enabling unfolding of discrete peaks to resolutions beyond the experimental resolution. In effect, it is the *human analyst*, not the method, that is performing the regularized optimization.

For continuous spectra, comprising numerous overlapping Gaussians, this approach fails. The solution space becomes too degenerate to identify the true solution uniquely, and unfolding with $\sigma < \sigma_\gamma$ is impossible without substantial additional regularization. Any choice of $\sigma < \sigma_\gamma$ leaves residual degeneracy. Therefore, the only viable choice for the response is $\mathbf{R} = \mathbf{G}_\gamma\mathbf{D}$, contrary to standard FICS.

The second issue, related to the first, concerns an ambiguity in the interpretation of $\hat{\boldsymbol{u}}_{\text{sol}}$: whether it represents sharp peaks ("delta peaks") or a spectrum with Gaussian correlation. For the former interpretation, Eq. (H8) is formally correct but practically unsolvable due to the non-invertibility of $\mathbf{G}_\lambda$. For the latter, the appropriate equation becomes

$$\mathbf{P}_{\text{f}}\hat{\boldsymbol{u}}_{\text{sol}} := \boldsymbol{y} - S\left(\hat{\boldsymbol{f}}_{\text{c}}\right) - \mathbf{G}_\lambda\mathbf{P}_{\text{p}}\hat{\boldsymbol{u}}^{(k)}. \tag{H9}$$

In this case, $\hat{\boldsymbol{u}}^{(k)}$ and $\hat{\boldsymbol{u}}_{\text{sol}}$ exist in distinct spaces: the former comprising sharp peaks, the latter exhibiting Gaussian correlation.

FICS can accommodate any smoothing operator S, but Gaussian smoothing is the most natural choice. Without any significant loss of generality, we define the smearing operation as a Gaussian smoothing $S\left(\hat{\boldsymbol{f}}_{\text{c}}\right) = \mathbf{G}_{\kappa}\hat{\boldsymbol{f}}_{\text{c}}$, where κ determines the resolution. Combining Eq. (H7) and Eq. (H9) yields

$$\mathbf{P}_{\text{f}}\hat{\boldsymbol{u}}_{\text{sol}} = \boldsymbol{y} - \mathbf{G}_{\kappa}\hat{\boldsymbol{f}}_{\text{c}} - \boldsymbol{y} + \mathbf{G}_{\lambda}\mathbf{P}_{\text{f}}\hat{\boldsymbol{u}}^{(k)} + \hat{\boldsymbol{f}}_{\text{c}}. \qquad (\text{H10})$$

Since $\mathbf{P}_{\text{f}}$ is diagonal, we can rearrange terms to obtain

$$\hat{\boldsymbol{u}}_{\text{sol}} = \mathbf{P}_{\text{f}}^{-1}\mathbf{G}_{\lambda}\mathbf{P}_{\text{f}}\hat{\boldsymbol{u}}^{(k)} + \mathbf{P}_{\text{f}}^{-1}(\mathbf{I} - \mathbf{G}_{\kappa})\hat{\boldsymbol{f}}_{\text{c}}. \qquad (\text{H11})$$

Had we instead employed definition Eq. (H8), and assuming $\mathbf{G}_{\lambda}$ were invertible, we would obtain

$$\begin{aligned}
\hat{\boldsymbol{u}}_{\text{sol}} &\overset{!}{=} \mathbf{P}_{\text{f}}^{-1}\mathbf{G}_{\lambda}^{-1}\mathbf{G}_{\lambda}\mathbf{P}_{\text{f}}\hat{\boldsymbol{u}}^{(k)} + \mathbf{P}_{\text{f}}^{-1}\mathbf{G}_{\lambda}^{-1}(\mathbf{I} - \mathbf{G}_{\kappa})\hat{\boldsymbol{f}}_{\text{c}} \\
&\overset{!}{=} \hat{\boldsymbol{u}}^{(k)} + \mathbf{P}_{\text{f}}^{-1}\mathbf{G}_{\lambda}^{-1}(\mathbf{I} - \mathbf{G}_{\kappa})\hat{\boldsymbol{f}}_{\text{c}}. \qquad (\text{H12})
\end{aligned}$$

In both cases, $\mathbf{I} - \mathbf{G}_{\kappa}$ extracts the residual between the original and smoothed spectrum. Thus, Compton subtraction can be interpreted as augmenting the original solution $\hat{\boldsymbol{u}}^{(k)}$ with modulated residual fluctuations, where the modulation factor is the full energy peak probability. For Eq. (H11), $\hat{\boldsymbol{u}}^{(k)}$ undergoes smearing from a sharp peak to experimental resolution via $\mathbf{G}_{\lambda}$, consistent with the definition of $\hat{\boldsymbol{u}}_{\text{sol}}$.

Assuming sufficient convergence of the iteration procedure, we have $\boldsymbol{y} = \mathbf{R}\hat{\boldsymbol{u}}^{(k)} + \boldsymbol{\delta}$ for some residual $\boldsymbol{\delta}$. Furthermore, under an additive noise model as in Sec. II D, we have $\boldsymbol{y} = \mathbf{R}\boldsymbol{\mu} + \boldsymbol{\epsilon}$, yielding

$$\boldsymbol{\delta} = \mathbf{R}\left(\boldsymbol{\mu} - \hat{\boldsymbol{u}}^{(k)}\right) + \boldsymbol{\epsilon}, \qquad (\text{H13})$$

meaning the residual is the sum of the noise $\boldsymbol{\epsilon}$ and of the difference between the true solution $\boldsymbol{\mu}$ and the unfolded solution $\hat{\boldsymbol{u}}^{(k)}$. Under the convergence condition, Eq. (H7) becomes

$$\begin{aligned}
\hat{\boldsymbol{f}}_{\text{c}} &= \left(\mathbf{G}_{\lambda}\mathbf{D} - \mathbf{G}_{\lambda}\mathbf{P}_{\text{f}} - \mathbf{G}_{\lambda}\mathbf{P}_{\text{p}}\right)\hat{\boldsymbol{u}}^{(k)} + \boldsymbol{\delta} \\
&= \underbrace{\mathbf{G}_{\lambda}\mathbf{P}_{\text{c}}\hat{\boldsymbol{u}}^{(k)}}_{\text{Smeared Compton}} + \boldsymbol{\delta}, \qquad (\text{H14})
\end{aligned}$$

by the definition of $\mathbf{D}$. Combining with Eq. (H11)

and Eq. (H13) we obtain[32]

$$\begin{aligned}
\hat{\boldsymbol{u}}_{\text{sol}} = &\left[\overbrace{\mathbf{P}_{\text{f}}^{-1}\mathbf{G}_{\lambda}\mathbf{P}_{\text{f}}}^{\text{Full energy component}} + \overbrace{\mathbf{P}_{\text{f}}^{-1}(\mathbf{I} - \mathbf{G}_{\kappa})\mathbf{G}_{\lambda}\mathbf{P}_{\text{c}}}^{\text{Compton residual}}\right]\hat{\boldsymbol{u}}^{(k)} \\
&+ \mathbf{P}_{\text{f}}^{-1}(\mathbf{I} - \mathbf{G}_{\kappa})\underbrace{\left[\mathbf{R}\left(\boldsymbol{\mu} - \hat{\boldsymbol{u}}^{(k)}\right) + \boldsymbol{\epsilon}\right]}_{\text{Difference residual and noise}}. \qquad (\text{H15})
\end{aligned}$$

The Compton subtraction method thus represents an affine transformation of $\hat{\boldsymbol{u}}^{(k)}$. It combines a smoothed version of the full energy peak with the residual of the smoothed Compton component, but critically, it also reintroduces both the noise component and the deviation from the true underlying signal.

A fundamental limitation of FICS arises from its convergence behavior. Instead of converging towards the ideal expectation value $\boldsymbol{\mu}$, the iteration converges to a solution $\boldsymbol{x}$ that satisfies the observation equation $\boldsymbol{y} = \mathbf{R}\boldsymbol{x}$. Because the observed data $\boldsymbol{y}$ inevitably contain noise, seeking a solution that perfectly fits $\boldsymbol{y}$ leads to overfitting, where the result conforms to the noise rather than the signal. This susceptibility to noise overfitting is a well-known characteristic of unregularized iterative methods like Richardson iteration (Sec. II D), and it persists in FICS despite the mitigation strategies of early stopping and Compton subtraction. Indeed, the Compton subtraction step exacerbates this issue by reintroducing noise via the second and third terms of Eq. (H15).

This noise-preserving behavior appears consistent with a stated objective of the original method [1]:

> "Our new Compton subtraction method (u) gives a much smoother spectrum with the same fluctuations as the observed spectrum (r)."

Given that earlier methods like the stripping method[39–42] often yield large fluctuations, this goal of FICS is laudable. However, preserving the observed spectrum's fluctuations is both ambiguous and fundamentally problematic from an unfolding perspective. As detailed in Sec. IV D, this terminology conflates two distinct concepts: *stochastic variation* (undesirable noise) and *spectral complexity* (desirable signal features). The primary aim of unfolding is precisely to reconstruct the spectral complexity while rigorously minimizing the influence of stochastic variation. Consequently, the unfolded spectrum *should not* replicate the high-frequency, bin-to-bin variations present in the observed spectrum. Doing so

---

[32] A third possibility involves unfolding with $\mathbf{R} = \mathbf{D}$, which would apparently yield

$$\hat{\boldsymbol{u}}_{\text{sol}} \overset{!}{=} \left[\mathbf{I} + \mathbf{P}_{\text{f}}^{-1}(\mathbf{I} - \mathbf{G}_{\kappa})\mathbf{P}_{\text{c}}\right]\hat{\boldsymbol{u}}^{(k)} + \mathbf{P}_{\text{f}}^{-1}(\mathbf{I} - \mathbf{G}_{\kappa})\boldsymbol{\delta}.$$

However, unfolding with $\mathbf{D}$ alone introduces a commutation error that invalidates both the folding and this expression; see Sec. IV.

merely ensures that the final result inherits stochastic noise, a direct consequence of the noise reintroduction mechanism demonstrated in (H15).

This critique may appear to contradict numerous studies (e.g., [1, 16, 43–45]) that demonstrate FICS's effectiveness. However, these studies share a common methodological limitation: they evaluate $\hat{\boldsymbol{u}}_{\mathrm{sol}}$ not by statistical comparison to the true solution $\boldsymbol{\mu}$ or $\boldsymbol{\eta}$, but by comparing the folded spectrum $\mathbf{R}\hat{\boldsymbol{u}}_{\mathrm{sol}}$ to the raw spectrum $\boldsymbol{y}$. As detailed in Secs. II D and IV C, this approach is inadequate because infinitely many solutions satisfy $\boldsymbol{y} = \mathbf{R}\boldsymbol{x}$, all yielding identical results under folding.

Nevertheless, within the broader context of the Oslo Method, the unfolding appears robust: forward modeling using input nuclear level density and gamma strength function successfully recovers both quantities [43]. However, this primarily validates the Oslo Method's reliability rather than FICS specifically. The Oslo Method's robustness likely stems from the strong physical constraints inherent in the first generation method, combined with the dimension reduction achieved through decomposition into unnormalized level density and transmission coefficient. To that end, the FICS solution appears sufficient as a point estimate.

Algorithm 3 Folding Iteration with Compton Subtraction (FICS). The algorithm follows [1] more closely rather than the main text, as that is what's generally used.

Require:
    Observed spectrum $\mathbf{y}$
    Discrete detector response $\mathbf{D}$
    Discrete smoothing operator $\mathrm{S_D}$
    Fluctuation smoothing operator $\mathrm{S_{fluct}}$
    Compton smoothing operator $\mathrm{S_{compton}}$
    Discrete detector response components
       $\mathbf{P}_{\mathrm{f}}, \mathbf{P}_{\mathrm{s}}, \mathbf{P}_{\mathrm{d}}, \mathbf{P}_{\mathrm{a}}, \mathbf{P}_{\mathrm{c}}$
    Fluctuation weight $0 \leq \alpha \leq 1$
    Maximum iterations limit $k_{\max}$

Ensure:
    Unfolded gamma-ray spectrum $\hat{\boldsymbol{u}}_{\mathrm{FICS}}$

1: `Initialize`
    Smooth the discrete response $\mathbf{D}_{\mathrm{smooth}} \leftarrow \mathrm{S_D}\,(\mathbf{D})$
    Set initial guess $\hat{\boldsymbol{u}} \leftarrow \mathbf{y}$
    Set iteration counter $k \leftarrow 0$
    Set previous cost $c_{\mathrm{tot}} \leftarrow \infty$

2: **while** not converged **do**

3:    `Fold the spectrum`
       Compute the folded trial spectrum:
       $\hat{\boldsymbol{f}}^{(k)} \leftarrow \mathbf{D}_{\mathrm{smooth}}\hat{\boldsymbol{u}}^{(k)}$

4:    `Update the unfolded spectrum`
       Update the trial function using the difference between observed and folded spectra:
       $\hat{\boldsymbol{u}}^{(k+1)} \leftarrow \hat{\boldsymbol{u}}^{(k)} + (\mathbf{y} - \hat{\boldsymbol{f}}^{(k)})$

5:    `Compute fluctuation cost`
       $\hat{\boldsymbol{u}}_{\mathrm{smooth}} \leftarrow \mathrm{S_{fluct}}\left(\hat{\boldsymbol{u}}^{(k+1)}\right)$

       $c_{\mathrm{fluct}} \leftarrow \sum_i |\hat{u}_i^{(k+1)} - (\hat{u}_{\mathrm{smooth}})_i|$

6:    `Compute residual cost` $\left(\chi^2\right)$

7:       $c_{\mathrm{res}}^{(k+1)} \leftarrow \sum_i \frac{\left(y_i - \hat{f}_i^{(k+1)}\right)^2}{y_i}$

8:    `Compute total cost as a weighted sum`

9:       $c_{\mathrm{tot}}^{(k+1)} \leftarrow \alpha c_{\mathrm{res}}^{(k+1)} + (1-\alpha)c_{\mathrm{fluct}}^{(k+1)}$

10:   `Check for convergence`
       If $c_{\mathrm{tot}}^{(k+1)} > c_{\mathrm{tot}}^{(k+1)}$: **Break**
       If $k + 1 > k_{\max}$: **Break**

11:   `Update states`
       $k \leftarrow k + 1$

12: **end while**

13: `Compton Subtraction`

14:   Estimate the Compton background by removing the other components from $\mathbf{y}$
       $\boldsymbol{f}_{\mathrm{discrete}} \leftarrow (\mathbf{P}_{\mathrm{f}} + \mathbf{P}_{\mathrm{s}} + \mathbf{P}_{\mathrm{d}} + \mathbf{P}_{\mathrm{a}})\,\hat{\boldsymbol{u}}^{(k)}$
       $\boldsymbol{f}_{\mathrm{compton}} \leftarrow \mathbf{y} - \boldsymbol{f}_{\mathrm{discrete}}$

15:   Smooth the estimated Compton
       $\tilde{\boldsymbol{f}}_{\mathrm{compton}} \leftarrow \mathrm{S_{compton}}\left(\boldsymbol{f}_{\mathrm{compton}}\right)$

16:   Estimate the full-energy component by removing the other discrete components and our estimate for Compton from $\mathbf{y}$
       $\boldsymbol{u}_{\mathrm{fe}} \leftarrow \mathbf{y} - \tilde{\boldsymbol{f}}_{\mathrm{compton}} - (\mathbf{P}_{\mathrm{s}} + \mathbf{P}_{\mathrm{d}} + \mathbf{P}_{\mathrm{a}})\,\hat{\boldsymbol{u}}^{(k)}$

17:   Correct for probability for full energy
       $\boldsymbol{u}_{\mathrm{fe}} \leftarrow \boldsymbol{u}_{\mathrm{fe}}/\boldsymbol{p}_{\mathrm{f}}$

18:   Correct for detector efficiency
       $\boldsymbol{u}_{\mathrm{fe}} \leftarrow \boldsymbol{u}_{\mathrm{fe}}/\boldsymbol{\varepsilon}$
       $\hat{\boldsymbol{u}}_{\mathrm{FICS}} \leftarrow \hat{\boldsymbol{u}}_{\mathrm{fe}}$

19: **Return**
    Unfolded gamma-ray spectrum $\hat{\boldsymbol{u}}_{\mathrm{FICS}}$

Appendix I: Notes on implementation

The RMLE method is implemented using the `Jax`[46] Python package, which provides just-in-time compilation and GPU support, making the optimization process feasible. We experimented with other methods, such as expectation maximization, and software packages designed for inverse problems, but they did not scale well to the millions of variables our problem requires. In contrast, using `Jax` allows the optimization to complete in just a few seconds on a desktop GPU. `Jax` also targets the CPU.

Relatively small unfoldings can be accomplished on the CPU, but a GPU is strongly recommended for large matrices, especially for uncertainty propagation.

The complete implementation of the RMLE algorithm is available as open-source software in the `OMpy` package[7, 47], permanently archived at Zenodo (doi:10.5281/zenodo.17594267). Although the `OMpy` package is relatively extensive, the MC RMLE algorithm itself, as described in this paper, can be implemented in roughly one hundred lines of `Jax`-based Python code.

[1] M. Guttormsen, T. Tveter, L. Bergholt, F. Ingebretsen, and J. Rekstad, The unfolding of continuum gamma-ray spectra, Nuclear Instruments and Methods in Physics Research Section A: Accelerators, Spectrometers, Detectors and Associated Equipment **374**, 371 (1996).

[2] M. Guttormsen, T. Ramsøy, and J. Rekstad, The first generation of gamma-rays from hot nuclei, Nuclear Instruments and Methods in Physics Research Section A: Accelerators, Spectrometers, Detectors and Associated Equipment **255**, 518 (1987).

[3] A. Schiller, L. Bergholt, M. Guttormsen, E. Melby, J. Rekstad, and S. Siem, Extraction of level density and gamma strength function from primary gamma spectra, Nuclear Instruments and Methods in Physics Research Section A: Accelerators, Spectrometers, Detectors and Associated Equipment **447**, 498 (2000).

[4] J. Rekstad, A. Henriquez, F. Ingebretsen, G. Midttun, B. Skaali, R. Øyan, J. Wikne, T. Engeland, T. F. Thorsteinsen, E. Hammaren, and E. Liukkonen, A study of the nuclear structure at high energy and low spin, Physica Scripta **1983**, 45 (1983).

[5] L. F. Richardson, Ix. the approximate arithmetical solution by finite differences of physical problems involving differential equations, with an application to the stresses in a masonry dam, Philosophical Transactions of the Royal Society of London. Series A, Containing Papers of a Mathematical or Physical Character **210**, 307 (1911).

[6] M. Guttormsen, A. Atac, G. Løvhøiden, S. Messelt, T. Ramsøy, J. Rekstad, T. F. Thorsteinsen, T. S. Tveter, and Z. Zelazny, Statistical gamma-decay at low angular momentum, Physica Scripta **1990**, 54 (1990).

[7] J. E. Midtbø, F. Zeiser, E. Lima, A.-C. Larsen, G. M. Tveten, M. Guttormsen, F. L. Bello Garrote, A. Kvellestad, and T. Renstrøm, A new software implementation of the oslo method with rigorous statistical uncertainty propagation, Computer Physics Communications **262**, 107795 (2021).

[8] L. Cavalier, Nonparametric statistical inverse problems, Inverse Problems **24**, 034004 (2008).

[9] A. Antoniadis and J. Bigot, Poisson inverse problems, The Annals of Statistics **34**, 10.1214/009053606000000687 (2006).

[10] A. H. Mjos, A.-C. Larsen, A. Kvellestad, and E. Lima (2025), work in preparation.

[11] M. Guttormsen, A. Bürger, T. Hansen, and N. Lietaer, The siri particle-telescope system, Nuclear Instruments and Methods in Physics Research Section A: Accelerators, Spectrometers, Detectors and Associated Equipment **648**, 168 (2011).

[12] S. Agostinelli, J. Allison, K. Amako, J. Apostolakis, H. Araujo, P. Arce, M. Asai, D. Axen, S. Banerjee, G. Barrand, F. Behner, L. Bellagamba, J. Boudreau, L. Broglia, A. Brunengo, H. Burkhardt, S. Chauvie, J. Chuma, R. Chytracek, G. Cooperman, G. Cosmo, P. Degtyarenko, A. Dell'Acqua, G. Depaola, D. Dietrich, R. Enami, A. Feliciello, C. Ferguson, H. Fesefeldt, G. Folger, F. Foppiano, A. Forti, S. Garelli, S. Giani, R. Giannitrapani, D. Gibin, J. Gómez Cadenas, I. González, G. Gracia Abril, G. Greeniaus, W. Greiner, V. Grichine, A. Grossheim, S. Guatelli, P. Gumplinger, R. Hamatsu, K. Hashimoto, H. Hasui, A. Heikkinen, A. Howard, V. Ivanchenko, A. Johnson, F. Jones, J. Kallenbach, N. Kanaya, M. Kawabata, Y. Kawabata, M. Kawaguti, S. Kelner, P. Kent, A. Kimura, T. Kodama, R. Kokoulin, M. Kossov, H. Kurashige, E. Lamanna, T. Lampén, V. Lara, V. Lefebure, F. Lei, M. Liendl, W. Lockman, F. Longo, S. Magni, M. Maire, E. Medernach, K. Minamimoto, P. Mora de Freitas, Y. Morita, K. Murakami, M. Nagamatu, R. Nartallo, P. Nieminen, T. Nishimura, K. Ohtsubo, M. Okamura, S. O'Neale, Y. Oohata, K. Paech, J. Perl, A. Pfeiffer, M. Pia, F. Ranjard, A. Rybin, S. Sadilov, E. Di Salvo, G. Santin, T. Sasaki, N. Savvas, Y. Sawada, S. Scherer, S. Sei, V. Sirotenko, D. Smith, N. Starkov, H. Stoecker, J. Sulkimo, M. Takahata, S. Tanaka, E. Tcherniaev, E. Safai Tehrani, M. Tropeano, P. Truscott, H. Uno, L. Urban, P. Urban, M. Verderi, A. Walkden, W. Wander, H. Weber, J. Wellisch, T. Wenaus, D. Williams, D. Wright, T. Yamada, H. Yoshida, and D. Zschiesche, Geant4—a simulation toolkit, Nuclear Instruments and Methods in Physics Research Section A: Accelerators, Spectrometers, Detectors and Associated Equipment **506**, 250 (2003).

[13] F. Zeiser, G. Tveten, F. Bello Garrote, M. Guttormsen, A. Larsen, V. Ingeberg, A. Görgen, and S. Siem, The γ-ray energy response of the oslo scintillator array oscar, Nuclear Instruments and Methods in Physics Research Section A: Accelerators, Spectrometers, Detectors and Associated Equipment **985**, 164678 (2021).

[14] C. Sükösd, W. Galster, I. Licot, and M. P. Simonart, Spectrum unfolding in high energy gamma-ray detection with scintillation detectors, Nuclear Instruments and Methods in Physics Research Section A: Accelerators, Spectrometers, Detectors and Associated Equip-

[15] B. Efron, Better bootstrap confidence intervals, Journal of the American Statistical Association **82**, 171 (1987).

[16] A. C. Larsen, R. Chankova, M. Guttormsen, F. Ingebretsen, S. Messelt, J. Rekstad, S. Siem, N. U. H. Syed, S. W. Ødegård, T. Lönnroth, A. Schiller, and A. Voinov, Microcanonical entropies and radiative strength functions of ^{50,51}V, Phys. Rev. C **73**, 064301 (2006).

[17] T. K. Eriksen, H. T. Nyhus, M. Guttormsen, A. Görgen, A. C. Larsen, T. Renstrøm, I. E. Ruud, S. Siem, H. K. Toft, G. M. Tveten, and J. N. Wilson, Pygmy resonance and low-energy enhancement in the γ-ray strength functions of pd isotopes, Phys. Rev. C **90**, 044311 (2014).

[18] M. Guttormsen, Y. Alhassid, W. Ryssens, K. Ay, M. Ozgur, E. Algin, A. Larsen, F. Bello Garrote, L. Crespo Campo, T. Dahl-Jacobsen, A. Görgen, T. Hagen, V. Ingeberg, B. Kheswa, M. Klintefjord, J. Midtbø, V. Modamio, T. Renstrøm, E. Sahin, S. Siem, G. Tveten, and F. Zeiser, Strong enhancement of level densities in the crossover from spherical to deformed neodymium isotopes, Physics Letters B **816**, 136206 (2021).

[19] M. Markova, A. C. Larsen, P. von Neumann-Cosel, S. Bassauer, A. Görgen, M. Guttormsen, F. L. B. Garrote, H. C. Berg, M. M. Bjørøen, T. K. Eriksen, D. Gjestvang, J. Isaak, M. Mbabane, W. Paulsen, L. G. Pedersen, N. I. J. Pettersen, A. Richter, E. Sahin, P. Scholz, S. Siem, G. M. Tveten, V. M. Valsdottir, and M. Wiedeking, Nuclear level densities and γ-ray strength functions in ^{120,124}Sn isotopes: Impact of porter-thomas fluctuations, Phys. Rev. C **106**, 034322 (2022).

[20] V. W. Ingeberg, S. Siem, M. Wiedeking, A. Choplin, S. Goriely, L. Siess, K. J. Abrahams, K. Arnswald, F. Bello Garrote, D. L. Bleuel, J. Cederkäll, T. L. Christoffersen, D. M. Cox, H. De Witte, L. P. Gaffney, A. Görgen, C. Henrich, A. Illana, P. Jones, B. V. Kheswa, T. Kröll, S. N. T. Majola, K. L. Malatji, J. Ojala, J. Pakarinen, G. Rainovski, P. Reiter, M. von Schmid, M. Seidlitz, G. M. Tveten, N. Warr, and F. Zeiser (The ISOLDE Collaboration), Nuclear level density and γ-ray strength function of ^{67}Ni and the impact on the i process, Phys. Rev. C **111**, 015803 (2025).

[21] T. Dozat, *Incorporating Nesterov Momentum into Adam*, Tech. Rep. (Stanford University, 2015).

[22] D. P. Kingma and J. Ba, Adam: A method for stochastic optimization (2017), arXiv:1412.6980 [cs.LG].

[23] A. C. Larsen, M. Guttormsen, M. Krtička, E. Běták, A. Bürger, A. Görgen, H. T. Nyhus, J. Rekstad, A. Schiller, S. Siem, H. K. Toft, G. M. Tveten, A. V. Voinov, and K. Wikan, Analysis of possible systematic errors in the oslo method, Phys. Rev. C **83**, 034315 (2011).

[24] H. T. Nyhus, S. Siem, M. Guttormsen, A. C. Larsen, A. Bürger, N. U. H. Syed, G. M. Tveten, and A. Voinov, Radiative strength functions in ^{163,164}Dy, Phys. Rev. C **81**, 024325 (2010).

[25] A. C. Larsen, N. Blasi, A. Bracco, F. Camera, T. K. Eriksen, A. Görgen, M. Guttormsen, T. W. Hagen, S. Leoni, B. Million, H. T. Nyhus, T. Renstrøm, S. J. Rose, I. E. Ruud, S. Siem, T. Tornyi, G. M. Tveten, A. V. Voinov, and M. Wiedeking, Evidence for the dipole nature of the low-energy γ enhancement in ^{56}Fe, Phys. Rev. Lett. **111**, 242504 (2013).

[26] V. W. Ingeberg, S. Siem, M. Wiedeking, K. Sieja, D. L. Bleuel, C. P. Brits, T. D. Bucher, T. S. Dinoko, J. L. Easton, A. Görgen, M. Guttormsen, P. Jones, B. V. Kheswa, N. A. Khumalo, A. C. Larsen, E. A. Lawrie, J. J. Lawrie, S. N. Majola, K. L. Malatji, L. Makhathini, B. Maqabuka, D. Negi, S. P. Noncolela, P. Papka, E. Sahin, R. Schwengner, G. M. Tveten, F. Zeiser, and B. R. Zikhali, First application of the Oslo method in inverse kinematics, European Physical Journal A **56**, 68 (2020).

[27] A. Spyrou, S. N. Liddick, A. C. Larsen, M. Guttormsen, K. Cooper, A. C. Dombos, D. J. Morrissey, F. Naqvi, G. Perdikakis, S. J. Quinn, T. Renstrøm, J. A. Rodriguez, A. Simon, C. S. Sumithrarachchi, and R. G. T. Zegers, Novel technique for constraining r-process (n, γ) reaction rates, Phys. Rev. Lett. **113**, 232502 (2014).

[28] S. N. Liddick, A. Spyrou, B. P. Crider, F. Naqvi, A. C. Larsen, M. Guttormsen, M. Mumpower, R. Surman, G. Perdikakis, D. L. Bleuel, A. Couture, L. Crespo Campo, A. C. Dombos, R. Lewis, S. Mosby, S. Nikas, C. J. Prokop, T. Renstrom, B. Rubio, S. Siem, and S. J. Quinn, Experimental neutron capture rate constraint far from stability, Phys. Rev. Lett. **116**, 242502 (2016).

[29] A. C. Larsen, J. E. Midtbø, M. Guttormsen, T. Renstrøm, S. N. Liddick, A. Spyrou, S. Karampagia, B. A. Brown, O. Achakovskiy, S. Kamerdzhiev, D. L. Bleuel, A. Couture, L. C. Campo, B. P. Crider, A. C. Dombos, R. Lewis, S. Mosby, F. Naqvi, G. Perdikakis, C. J. Prokop, S. J. Quinn, and S. Siem, Enhanced low-energy γ-decay strength of ^{70}Ni and its robustness within the shell model, Phys. Rev. C **97**, 054329 (2018).

[30] A. Simon, S. Quinn, A. Spyrou, A. Battaglia, I. Beskin, A. Best, B. Bucher, M. Couder, P. DeYoung, X. Fang, J. Görres, A. Kontos, Q. Li, S. Liddick, A. Long, S. Lyons, K. Padmanabhan, J. Peace, A. Roberts, D. Robertson, K. Smith, M. Smith, E. Stech, B. Stefanek, W. Tan, X. Tang, and M. Wiescher, Sun: Summing nai(tl) gamma-ray detector for capture reaction measurements, Nuclear Instruments and Methods in Physics Research Section A: Accelerators, Spectrometers, Detectors and Associated Equipment **703**, 16 (2013).

[31] C. Dembski, M. Kuchera, S. Liddick, R. Ramanujan, and A. Spyrou, Two-dimensional total absorption spectroscopy with conditional generative adversarial networks, Nuclear Instruments and Methods in Physics Research Section A: Accelerators, Spectrometers, Detectors and Associated Equipment **1060**, 169026 (2024).

[32] A. Giaz, L. Pellegri, S. Riboldi, F. Camera, N. Blasi, C. Boiano, A. Bracco, S. Brambilla, S. Ceruti, S. Coelli, F. Crespi, M. Csatlòs, S. Frega, J. Gulyàs, A. Krasznahorkay, S. Lodetti, B. Million, A. Owens, F. Quarati, L. Stuhl, and O. Wieland, Nuclear Instruments and Methods in Physics Research Section A: Accelerators, Spectrometers, Detectors and Associated Equipment **729**, 910 (2013).

[33] A. Simon, M. Guttormsen, A. C. Larsen, C. W. Beausang, P. Humby, J. T. Harke, R. J. Casperson, R. O. Hughes, T. J. Ross, J. M. Allmond, R. Chyzh, M. Dag, J. Koglin, E. McCleskey, M. McCleskey, S. Ota, and A. Saastamoinen, First observation of low-energy γ-ray enhancement in the rare-earth region, Phys. Rev. C **93**, 034303 (2016).

[34] A. C. Larsen, G. M. Tveten, T. Renstrøm, H. Utsunomiya, E. Algin, T. Ari-izumi, K. O. Ay, F. L. Bello Garrote, L. Crespo Campo, F. Furmyr, S. Goriely, A. Görgen, M. Guttormsen, V. W. Ingeberg, B. V. Kheswa, I. K. B. Kullmann, T. Laplace, E. Lima,

M. Markova, J. E. Midtbø, S. Miyamoto, A. H. Mjøs, V. Modamio, M. Ozgur, F. Pogliano, S. Riemer-Sørensen, E. Sahin, S. Shen, S. Siem, A. Spyrou, and M. Wiedeking, New experimental constraint on the ^{185}W$(n, \gamma)^{186}$W cross section, Phys. Rev. C **108**, 025804 (2023).

[35] L. Kirsch and L. Bernstein, Rainier: A simulation tool for distributions of excited nuclear states and cascade fluctuations, Nuclear Instruments and Methods in Physics Research Section A: Accelerators, Spectrometers, Detectors and Associated Equipment **892**, 30 (2018).

[36] F. Bečvář, Simulation of γ cascades in complex nuclei with emphasis on assessment of uncertainties of cascade-related quantities, Nuclear Instruments and Methods in Physics Research Section A: Accelerators, Spectrometers, Detectors and Associated Equipment **417**, 434 (1998).

[37] L. Kantorovich, On the translocation of mass, Doklady Akademii Nauk SSSR **37**, 227 (1942).

[38] L. V. Kantorovich, Mathematical methods of organizing and planning production, Management Science **6**, 366 (1960).

[39] W. Trautmann, J. F. Sharpey-Schafer, H. R. Andrews, B. Haas, O. Hausser, P. Taras, and D. Ward, Measurement of the linear polarization of continuum gamma rays from (32s,xn) reactions to prolate and oblate rare-earth nuclei, Nuclear Physics A **378**, 141 (1982).

[40] D. C. Radford, I. Ahmad, R. Holzmann, R. V. F. Janssens, and T. L. Khoo, A prescription for the removal of compton-scattered gamma rays from gamma-ray spectra, Nuclear Instruments and Methods in Physics Research Section A **258**, 111 (1987).

[41] D. J. G. Love and A. H. Nelson, Unfolding the response function of high-quality germanium detectors, Nuclear Instruments and Methods in Physics Research Section A **274**, 541 (1989).

[42] J. C. Waddington, An iterative method for estimating background in gamma-ray spectra, Nuclear Instruments and Methods in Physics Research Section A **274**, 608 (1989).

[43] A. C. Larsen, M. Guttormsen, M. Krtička, E. Běták, A. Bürger, A. Görgen, H. T. Nyhus, J. Rekstad, A. Schiller, S. Siem, H. K. Toft, G. M. Tveten, A. V. Voinov, and K. Wikan, Analysis of possible systematic errors in the oslo method, Phys. Rev. C **83**, 034315 (2011).

[44] A. C. Larsen, M. Guttormsen, R. Chankova, F. Ingebretsen, T. Lönnroth, S. Messelt, J. Rekstad, A. Schiller, S. Siem, N. U. H. Syed, and A. Voinov, Nuclear level densities and γ-ray strength functions in ^{44,45}Sc, Phys. Rev. C **76**, 044303 (2007).

[45] N. U. H. Syed, M. Guttormsen, F. Ingebretsen, A. C. Larsen, T. Lönnroth, J. Rekstad, A. Schiller, S. Siem, and A. Voinov, Level density and γ-decay properties of closed shell pb nuclei, Phys. Rev. C **79**, 024316 (2009).

[46] J. Bradbury, R. Frostig, P. Hawkins, M. J. Johnson, C. Leary, D. Maclaurin, G. Necula, A. Paszke, J. VanderPlas, S. Wanderman-Milne, and Q. Zhang, JAX: composable transformations of Python+NumPy programs (2018).

[47] E. Lima, Ompy: Rmle algorithm (v1.0.0) (2025).